

Liquid crystal switchable optical devices



Ethan Isaak Luke Jull

University of Leeds

School of Physics and Astronomy

Submitted in accordance with the requirements for the degree of

Doctor of Philosophy

December 2019



The candidate confirms that the work submitted is his own, except where work which has formed part of jointly authored publications has been included. The contribution of the candidate and the other authors to this work has been explicitly indicated below. The candidate confirms that appropriate credit has been given within the thesis where reference has been made to the work of others.

This copy has been supplied on the understanding that it is copyright material and that no quotation from the thesis may be published without proper acknowledgement.

The right of Ethan Isaak Luke Jull to be identified as Author of this work has been asserted by Ethan Isaak Luke Jull in accordance with the Copyright, Designs and Patents Act 1988.

For my family and friends

Acknowledgements

During this PhD I have had the pleasure of researching a truly beautiful area of Physics and a fundamentally interesting phenomenon. I have met and collaborated with incredible people from around the globe, and quite literally travelled around the world in 62 days, though that doesn't quite have as nice a ring to it. There are numerous people that I must thank for providing opportunities, support, and encouragement over these fantastic years.

Firstly I would like to thank my supervisor Professor Helen Gleeson who has continually provided me with advice and opportunity over the past 4 years. The opportunities and support you have provided me has truly allowed me to make the most of this PhD. I have attended multiple international conferences, conducted an industrial project, and collaborated with researchers in Japan all thanks to your continual encouragement, pushing me forward to apply for additional funding and applying for all these incredible opportunities. Your advice surrounding my research, giving me excellent guidance whilst still allowing me to pursue lines of interest, is truly appreciated and has allowed me to develop as a researcher.

I would also like to thank Professor Kiyooki Usami with whom I had two years of excellent collaboration with. I want to thank you firstly for hosting me in Osaka, an exceptional highlight of my time as a PhD student, as well as continually providing support, patience, and expertise during our research collaboration. Special thanks also goes to Dr. Serak, Dr. Grozhik, Dr. Cowling, Dr. Mandle, and Dr. Ellis for

chemical synthesis of many of the materials utilised throughout my PhD. Chemistry is most definitely not my strong suit and the ability to utilise these incredibly materials, without having to synthesise them myself, in my studies is greatly appreciated.

Special thanks must also go to Dr. John Lydon, for providing intriguing discussions over coffee, helping me explore the beautiful world of liquid crystal topological defects (helping me get my first ever authorship in a journal), and of course for the brilliant annual Christmas party.

The soft matter group at Leeds is filled with incredible people who have been a continual support during my PhD either through experimental training, theoretical sanity checks, or simply providing non-work related merriment. I would like to give exceptional thanks to all of my PhD co-conspirators, past and present, you all made my time in Leeds a wonderful experience and made my PhD enjoyable even when research was frustratingly non-cooperative. Special thanks must also go to Gelnys Bowles and Paula Talbot without whom I would never have managed to navigate the extreme terrain of University admin.

Lastly, but by no means least, I would like to thank my family and friends for their unconditional support, even if never fully understanding what it is I do or why I'm doing it. Thank you Mum, Dad, and Jacob for everything over the last 25 years, supporting all of my endeavours including this ridiculous PhD, I bet you're glad I didn't ask you to proof read this one! I truly wouldn't be where I am today without you and I cannot express enough thanks.

Abstract

This thesis will investigate liquid crystal materials for application in switchable optical devices, with a focus on dichroic dyes and the photoisomerisation of azobenzene-based materials.

An electrically switchable and tuneable liquid crystal Lyot filter is presented which demonstrates excellent switching from transmission to blocking modes with a response time between 40 and 110ms depending on the wavelength rejection required.

The effect of doping nematic liquid crystal 5CB with a new high-solubility anthraquinone dye is investigated. The solubility limit is found to be 7%($\frac{w}{w}$), greater than any previously reported anthraquinone dye, allowing for better colour saturation in guest-host devices. The inclusion of this dye is found to improve the nematic temperature range of the system, with 5%($\frac{w}{w}$) dye generating an increase in the nematic temperature range by 8.3°C. The optical, elastic, and dielectric properties dependence on dye concentration are fully investigated and the observed dependencies discussed in terms of device implications.

An anthraquinone dichroic dye doped liquid crystal elastomer is developed and the strain dependence of order parameter is measured via the polarisation angle dependent absorption of the anthraquinone dye. A temperature independent linear relationship between order parameter and strain is demonstrated, with excellent agreement with separate Raman spectroscopy data. A maximum order parameter of $S = (0.28 \pm 0.01)$ is measured in the initially isotropic system. The

transmission dependence on strain means that this material could be implemented as a simple optical strain sensor, with a continuous variation on transmission observed with applied strain.

An azobenzene material BAAB2 is utilised in the investigation of the impact of photoisomerisation on nematic host 5CB. The nematic temperature range of BAAB2 un-irradiated is between 48 and 83°C and the absorption peaks corresponding to the *trans* and *cis* excitations are found at 350nm and 435nm respectively.

Doping of 5CB with BAAB2 at varying concentration between 0 and 10% ($\frac{w}{w}$) is undertaken and the change in nematic to isotropic phase transition temperature is investigated for various illumination conditions. In the un-irradiated state the nematic to isotropic phase transition temperature is found to increase from 36.3 to 41.4°C, a direct result of BAAB2's higher nematic temperature range when compared with 5CB. In the yellow-filtered state a reduction in transition temperature is observed with increasing *cis* concentration, with the relative change in intermolecular interaction energy measured as $(-3.5 \pm 0.3) \cdot 10^{-3}$. Under continuous **unpolarised** UV irradiation the relative change in intermolecular interaction energy is 2.5 times larger, at $(-8.7 \pm 0.2) \cdot 10^{-3}$. This is associated with the light-induced torque generated out of the plane by the selective excitation of the BAAB2 material, confirmed via dielectrics measurements of the system under yellow-filtered and continuous UV irradiation conditions.

It is demonstrated that the BAAB2 doped 5CB system can be utilised as an all-optical automatic switchable laser protection device which switches from transmission to protection mode when the laser "threat" irradiates the system. The response time dependence on temperature and laser power is fully characterised and the ability for this all-optical device to provide protection for CCD cameras is evaluated.

Abbreviations

LC	Liquid crystal
LIMR	Light-induced molecular reorientation
LIOM	Light-induced order modification
TDM	Transitional dipole moment
LIM	Light-induced impurity
DSC	Differential scanning calorimetry
POM	Polarised optical microscopy
ITO	Indium tin oxide
5CB	<i>4-pentyl-4'-cyanobiphenyl</i>
MBBA	<i>N-(4-Methoxybenzylidene)-4-butaniline</i>
BAAB2	<i>4-2-butyl-4'-2-alkoxyazobenzene</i>
15NB3OH	<i>1,5-Dihydroxy-4,8-bis-(4-propylphenylamino)anthraquinone</i>
15NB3	<i>1,5-bis(4-propylphenyl)aminoanthraquinone.</i>

Table 1: General abbreviations

\underline{n}	Director
\underline{k}	Layer normal
S	Order parameter
$f(\theta, \phi)$	Distribution function
\parallel	Parallel to the director
\perp	Perpendicular to the director
d	Cell gap
c	Concentration
\mathbf{a}	Rod unit vector
θ	Deviation angle of rod vector from director
ϕ	Deviation angle of rod vector in x-y plane
θ_{tilt}	Surface pre-tilt
β	Angle between dye TDM and rod unit vector
Υ	Torque
N	Volume concentration

Table 2: General LC symbols

n	Refractive index
χ	Susceptibility
n_e	Extraordinary refractive index
n_o	Ordinary refractive index
Δn	Birefringence
Γ	Optical retardance
λ	Wavelength
A	Absorption
α	Absorption coefficient
ψ	Angle between polarisation vector and director
D	Dichroic ration

Table 3: General LC optics symbols

G	Gibbs free energy
g	Free energy density
F_{diel}	Electric free energy
F_{el}	Elastic free energy
ν	Volume
k_i	Elastic moduli
a_i	Curvature component
ϵ_0	Permittivity of free space
ϵ	Dielectric permittivity
$\Delta\epsilon$	Dielectric anisotropy
V	Voltage
V_{th}	Threshold voltage
Ψ	Z-dependant director angle
C	Capacitance

Table 4: General LC elastic and electric symbols

k_B	Boltzmann's constant
T	Temperature
T_{NI}	Nematic to isotropic phase transition temperature
τ	Reduced temperature
Λ	Intermolecular interaction energy
v	Intermolecular interaction potential

Table 5: General LC temperature symbols

Contents

1	Motivation and direction	1
2	Fundamentals of liquid crystals	5
2.1	Introduction	5
2.2	Liquid crystal phases	6
2.3	Order parameter	8
2.4	Refractive indices and birefringence	10
2.5	Elastic properties	12
2.6	Director deformation under electric fields	14
2.7	Summary	17
3	Dyes and photoisomerisation	21
3.1	Dichroic dyes	21
3.1.1	Dye types and properties	23
3.1.2	Dichroism and the order parameter	24
3.2	Photoisomerisation	27
3.2.1	Optical nonlinearities in liquid crystals	28
3.2.2	Light-induced molecular reorientation	29
3.2.3	Light-induced order modification	30
3.3	Summary	34
4	Experimental methods and materials	39
4.1	Materials	39
4.2	Polarised optical microscopy	41
4.3	Differential scanning calorimetry	46

CONTENTS

4.4	Dielectrics	48
4.5	LC devices	51
4.5.1	Device types	51
4.5.2	Device fabrication	54
4.5.3	Summary	55
5	Liquid crystal Lyot filter	59
5.1	Introduction	59
5.2	Liquid crystal Lyot filter	60
5.3	Results and discussion	62
5.3.1	Device spectra	62
5.3.2	Rejection wavelength tuning	63
5.3.3	Response speed	65
5.4	Summary	67
6	Dichroic dye doped systems	71
6.1	High-solubility anthraquinone dye	71
6.1.1	Materials and methods	72
6.1.2	Phase effects	73
6.1.3	Optical properties	76
6.1.4	Elastic and dielectric properties	78
6.1.5	High-solubility summary	80
6.2	Guest-host LC elastomer	81
6.2.1	Materials and methods	81
6.2.2	Results and discussion	82
6.2.3	Dye-doped LCE summary	84
6.3	Summary	85
7	Photoisomerisation of BAAB2	89
7.1	BAAB2	91
7.1.1	BAAB2 phases	91
7.1.2	BAAB2 absorption	94
7.1.3	Summary of BAAB2	96
7.2	BAAB2 doped 5CB	98

7.2.1	Un-irradiated phase sequence	98
7.2.2	Laser-irradiated phase sequence	100
7.2.3	Summary of BAAB2 doped 5CB	103
7.3	Photoisomerisation and order	105
7.3.1	Method and materials	105
7.3.2	Order parameter of 5CB	108
7.3.3	Absorption coefficient of <i>cis</i> BAAB2	109
7.3.4	Yellow-filtered order modification	112
7.3.5	BAAB2 <i>cis</i> orientation	118
7.3.6	UV-irradiated order modification	122
7.4	Summary	126
8	Photoisomerisation and physical properties	129
8.1	Dielectrics	129
8.1.1	15NB3OH doped 5CB	131
8.1.2	Yellow-filtered physical properties	133
8.1.3	UV-Irradiated physical properties	140
8.2	Summary	145
9	Time-dependence of photoisomerisation	147
9.1	Time-dependent optical properties	147
9.2	Time-dependence of capacitance	151
9.3	Summary	154
9.4	Summary of photoisomerisation investigation	156
10	All-optical automatic switchable laser protection	159
10.1	Introduction	159
10.2	Materials and methods	160
10.3	Results and discussion	161
10.3.1	Phase transition temperature	161
10.3.2	Device spectra	164
10.3.3	Response time	165
10.4	Summary	167

CONTENTS

11 Conclusion	173
A Materials Glossary	179

List of Figures

2.1	The isotropic liquid, LC, and solid crystal phases of matter are depicted. The isotropic liquid exhibits short-range positional order and fluidity. LC phases exhibit long range order (orientational) and fluidity. Solid crystal phases exhibit long range positional order, but are unable to flow.	6
2.2	The (a) nematic, (b) smectic-A, and (c) smectic-C phases are shown. The director and layer normal are denoted n and k	7
2.3	(a) Chirality is shown to be when the mirror image cannot be superimposed upon the original object. (b) The chiral nematic (cholesteric) phase is shown in which the director rotates through the sample forming a helicoidal structure.	8
2.4	The model of simple rods used to generate a numerical order parameter, θ is the angle between the director (z-axis) and the rods vector (\mathbf{a}), whilst ϕ is the angle in the x-y plane.	9
2.5	The Fresnel or refractive index ellipsoid is shown. This demonstrates the dielectric susceptibility of the material in all directions and shows how the refractive index will be different depending on the propagation direction.	10
2.6	The wavelength dispersion of n_e and n_o for nematic LC <i>4-pentyl-4'-cyanobiphenyl</i> (5CB). Data acquired from extended Cauchy model fit parameters [10].	12
2.7	The possible torsional deformations available in the LC director. The director n is parallel with the z-axis of the Cartesian frame. .	13

LIST OF FIGURES

- 2.8 A planar aligned nematic is depicted. (a) In the low voltage state, $V < V_{th}$ the director field remains uniform. (b) At just above the threshold voltage the director field in the centre of the device begins to reorient and the splay elastic force dominates. (c) At voltages much greater than the threshold voltage the director reorients to be approximately homeotropic, although anchoring prevents this at the surfaces. 15
- 3.1 Anthraquinone dichroic dye (15NB3OH) is shown with the relationship between molecular long-axis and TDM (absorption axis) demonstrated. The angle $\beta = 15.9^\circ$ is calculated from time-dependent density functional theory [1]. 22
- 3.2 The basic chemical foundation of (a) azo-dyes and (b) anthraquinone-dyes. Chemical substitutions can modify the physical properties of these dichroic dyes. 23
- 3.3 (a) The model of a guest-host system is shown. The director is in the z-direction. The LC host can vary by an angle θ_{host} away from the director and the dichroic dye can vary away from the director by an angle θ_{dye} . The dichroic dye TDM varies by an angle β away from the dye's long axis. (b) A depiction of the standard dichroic dye guest-host system. The dichroic dye molecules align with the LC host. The sizes of the molecules are representative of the chemical structure, with the dye 15NB3OH being slightly larger than host 5CB. 25
- 3.4 (a) The *trans* and *cis* conformers of azobenzene are shown. (b) An example of the energy landscape for the photoisomerisation process is demonstrated. 28
- 3.5 Transmission of methyl-orange ($\lambda = 488nm$) as a function of irradiation time parallel (T_{\parallel}) and perpendicular (T_{\perp}) to the pump polarisation is shown, redrawn from [23]. 29
- 3.6 The photoisomerisation of an azo-based mesogen from *trans* to *cis*. The molecules goes from a well packed nematic rod-shape, to a bent molecule that disrupts the ordering of the nematic host. . . 31

LIST OF FIGURES

3.7	The conformational <i>trans</i> and <i>cis</i> states of LC MBBA used in experiments on optically induced nonlinearities [18, 30].	32
4.1	The chemical structure of 5CB is shown. The crystal to nematic phase transition temperature is $25.0^{\circ}C$ and the nematic to isotropic phase transition temperature is $36.3^{\circ}C$	40
4.2	The chemical structure of BAAB2 is shown. The crystal to nematic phase transition temperature is $48.5^{\circ}C$ and the nematic to isotropic phase transition temperature is $83.5^{\circ}C$	40
4.3	The chemical structure of 15NB3OH is shown. The absorption peaks at $\lambda = 694nm$ and the angle the TDM makes with the molecular long axis is $\beta = 15.9^{\circ}$ [8].	41
4.4	(a) Unpolarised light is polarised by a polariser, upon passing through a birefringent medium a retardance is applied. Although this will typically generate elliptically polarised light here it is simply depicted as a rotation in the polarisation. Partial transmission of light is then achieved through the analyser due to the modification to the polarised light. (b) The Leica DM2700 polarising microscope used in the majority of experiments is shown. The entire system is depicted in terms of optical path and microscope parts.	42
4.5	The DSC heat flow trace for typical LC material 5CB, with a heating rate of $10^{\circ}Cmin^{-1}$. On heating the enthalpy change associated with the crystal (K) to nematic (N) phase and the nematic to isotropic (I) phase transition is observed. On cooling the enthalpy change associated with the isotropic to nematic phase transition is observed, however the nematic to crystal phase transition isn't observed in the demonstrated temperature range as a result of the sample super cooling.	47

LIST OF FIGURES

4.6	(a) The voltage dependence of capacitance is shown for 5CB sample at $20^{\circ}C$. The dielectrics fitting with pre-tilt gave parameters of $k_{11} = 6.8pN$, $k_{33} = 10.5pN$, $\epsilon_{\parallel} = 20.0$, $\epsilon_{\perp} = 6.2$, and $\theta_{tilt} = 1.5^{\circ}$. The dielectrics fitting without pre-tilt gave parameters of $k_{11} = 6.1pN$, $k_{33} = 10.9pN$, $\epsilon_{\parallel} = 20.0$, and $\epsilon_{\perp} = 6.3$. (b) A clear demonstration of the difference in fitting when pre-tilt is included into the fitting procedure.	50
4.7	The comparison of dielectric fitting results for 5CB (a) dielectric permittivity and (b) elastic constants with accepted literature values [16].	50
4.8	(a) The standard planar aligned LC device is depicted. The substrates are rubbed in the anti-parallel fashion and a uniform director orientation is observed. (b) A planar aligned device with parallel rubbing directions is shown. Unidirectional alignment is achieved, however the parallel rubbing results in the formation of chevrons affecting the director field.	52
4.9	(a) The un-rubbed homeotropic device is demonstrated. (b) The rubbed homeotropic device is demonstrated, with the rubbing generating a small, typically less than 1° , pre-tilt preferential direction away from 90° . (c) Application of an electric field to a negative dielectric LC in an un-rubbed homeotropic device is demonstrated, with the random re-orientation demonstrated. (d) Application of an electric field to a negative dielectric LC in a rubbed homeotropic device is demonstrated, with the well aligned re-orientation demonstrated.	53
4.10	(a) The HAN device is shown which consists of a homeotropic treated layer and a planar treated layer. (b) The TN device is shown in which the planar substrates are rubbed at 90° with respect to each other generating a twisted director profile.	54

5.1 LC Lyot filter device schematic. The polariser and analyser are in the xy plane, aligned at 45° to the x and y axis. The LC director is oriented along x axis. Control of the LC birefringence is achieved through application of an E-field. 61

5.2 (a) The ON state experimental Lyot filter transmission as a function of wavelength. Theoretical fitting of equation 5.2 to the experimental data shows excellent agreement. (b) The ON ($0V_{rms}$) and OFF ($30V_{rms}$) experimental transmission of the single stage Lyot filter as a function of wavelength. In the ON state rejection at $\lambda=650\text{nm}$ is observed, whilst in the OFF state a uniform transmission across the spectrum is observed. Insert images, taken using a Nikon D7100 camera, demonstrate imaging through the device in the OFF (top) and ON (bottom) states. Even in protection mode partial observations are still possible. 63

5.3 (a) The voltage dependence of the transmission spectra for the LC Lyot filter under investigation. The rejection wavelength clearly blue-shifts with increasing voltage. (b) The rejection wavelength (half-wave plate condition) is observed to depend linearly on voltage applied to the LC component. 64

5.4 (a) Change in intensity with respect to time for switching the device between the OFF ($30V_{rms}$) and ON state ($0.940V_{rms}$) for rejection of the green laser. The switch is clear, with a response time of $\tau_{ON}=(60\pm 10)\text{ms}$. Image inserts demonstrate the laser spot in the far field, taken using a deltaPix camera. (b) The ON and OFF response times associated with switching between protection schemes for typical laser wavelengths. Errors in the millisecond regime are $\pm 10\text{ms}$; in the microsecond regime are $\pm 5\mu\text{s}$ 66

LIST OF FIGURES

- 6.1 (a) The phase transition temperature dependence on RM1790 dye concentration in 5CB is shown, measured via DSC (error in transition temperature given as $\pm 0.1^\circ\text{C}$). (b) The nematic to isotropic phase transition temperature dependence on the concentration of RM1790 in 5CB. Extrapolation of the over saturated concentration to find the solubility limit is demonstrated. (c) POM demonstrates clear phase separation of the dye in the highest concentration sample. (d) The DSC heat flow trace for $14.6\%(\frac{w}{w})$ RM1790 in 5CB. The bottom trace is the sample on heating and the enthalpy change associated with dissolving the re-crystallised dye back into solution is observed at approximately 52°C . This is confirmed via POM, with image inserts demonstrating each temperature regime of the system. 74
- 6.2 (a) The absorption spectrum for $4.98\%(\frac{w}{w})$ RM1790 in 5CB in a planar aligned device with the light polarised parallel and perpendicular to the nematic director, normalised with respect to pure 5CB. (b) The absorption normalised with respect to cell gap (polarisation parallel and perpendicular to the director) dependence on dye concentration in 5CB. The Beer-Lambert relationship is fit to calculate the absorption coefficients for each orientation. 77
- 6.3 The dependence of (a) splay elastic constant, (b) bend elastic constant, and (c) dielectric permittivities on reduced temperature for varying concentration of RM1790 in 5CB. 79
- 6.4 (a) The absorption spectrum for the 15NB3 doped LCE at zero strain and high strain is demonstrated for polarisation angles (ϕ) of 0 and 90° to the strain axis. (b) The low strain macroscopic image of the sample with polarisation at 0 and 90° shown. (c) The high strain macroscopic image of the sample with polarisation at 0 and 90° shown. (b, c) Images have increased contrast and lightness to help demonstrate the variation in transmission between polarisation angle. 83

6.5	The order parameter dependence on strain for the 15NB3 doped LCE as measured via the polarisation angle dependent absorption properties. (a) Room temperature data is directly compared with Raman spectroscopy order parameter data collected by M. Nikkhou. (b) A comparison of 9.5 and 22°C order parameter dependence of strain measured via the 15NB3 absorption properties.	84
6.6	The contrast in transmission at 550nm is demonstrated as a function of strain for 15NB3 doped LCE. Image inserts demonstrate macroscopic view of the material at a strain of (0.276 ± 0.004) demonstrating the colour difference between the two polarisation angles with respect to the strain direction.	85
7.1	The chemical structure of BAAB2 is shown. The <i>trans</i> and <i>cis</i> conformers are demonstrated.	91
7.2	(a) The DSC data showing heat flow with respect to temperature for BAAB2 at a heat rate of $10^{\circ}Cmin^{-1}$. (b) The transmission of a red laser coupled to a POM setup through a randomly aligned planar BAAB2 sample. (c) POM images of a randomly aligned planar BAAB2 sample using a red filter to prevent photo-switching of the material.	93
7.3	The absorption spectrum of BAAB2 dissolved in acetone is shown. There are two distinct peaks in absorption, with $\lambda = (350 \pm 1)nm$ corresponding to the $\pi - \pi^*$ transition for the <i>trans</i> excitation and $\lambda = (435 \pm 3)nm$ corresponds to the $n - \pi^*$ transition for <i>cis</i> excitation.	95
7.4	Un-irradiated nematic to isotropic phase transition temperatures for varying concentration of BAAB2 in 5CB. A comparison of two techniques DSC and red-filtered POM are shown. An increase in nematic to isotropic transition temperature is observed for increasing BAAB2 concentration in 5CB.	98
7.5	Comparison of un-irradiated and laser-irradiated nematic to isotropic transition temperature for varying BAAB2 dopant concentration in 5CB.	101

LIST OF FIGURES

7.6	The relative change (in Kelvin) in the nematic to isotropic phase transition temperature plotted as a function of BAAB2 <i>cis</i> concentration. Fitted with equation 7.2 with intercept fixed at (0, 0).	103
7.7	15NB3OH absorption spectrum is shown with the input light polarisation parallel and perpendicular to the nematic host director. Peak absorption wavelength found at $\lambda = 694nm$	106
7.8	The experimental setup used to measure the optical properties of the samples whilst under UV irradiation is depicted.	107
7.9	A comparison of the measured nematic order parameter for 0.5% 15NB3OH in 5CB (attained via the dichroic ratio) with published literature [7].	108
7.10	The average absorption at $\lambda = 450nm$ (normalised with respect to cell gap) is plotted as a function of BAAB2 <i>cis</i> molar concentration. These absorption measurements are taken during continuous UV irradiation of the BAAB2 doped samples and multiple repeats of the same concentrations are conducted. Fitting of the Beer-Lambert law is employed with the intercept fixed at (0, 0).	110
7.11	The polarisation angle dependence at $\lambda = 450nm$ of the guest-host 0.5% 15NB3OH + 2%($\frac{w}{w}$) BAAB2 in 5CB system in the yellow-filtered and irradiated states. The molar concentration of <i>cis</i> conformers in the un-irradiated and irradiated states are measured to be 0.65% and 1.62%. The 450nm absorption corresponds to the BAAB2 <i>cis</i> conformer absorption.	112
7.12	DSC transition temperatures are shown for varying BAAB2 concentration in 15NB3OH doped 5CB and non-15NB3OH doped 5CB. A general increase in transition temperature with increasing BAAB2 concentration is observed.	113

7.13 An example of the difference in the order parameter dependence on (a) temperature and (b) reduced temperature for two yellow-filtered mixtures of BAAB2 in 15NB3OH doped 5CB. The lower concentration mixture (2%($\frac{w}{w}$) BAAB2) has a lower molar concentration of *cis* conformers (0.91%) whilst the higher concentration mixture (10%($\frac{w}{w}$) BAAB2) has a higher steady state molar concentration of *cis* molecules (4.0%). This higher concentration of *cis* conformers results in a larger reduction in the order parameter curve. Plotting as a function of reduced temperature shows that the two systems follow similar nematic behaviour as expected. . . . 115

7.14 (a) Nematic to isotropic phase transition temperature as a function of *cis* concentration in the yellow-filtered state. (b) The relative change in the nematic to isotropic phase transition temperature as a function of *cis* concentration in the yellow-filtered state. Fitting of the LIOM model (equation 7.2) gives the relative change in interaction energy, intercept fixed at (0, 0). 116

7.15 The transmission spectrum of the red-filter utilised in previous experimental results and the yellow-filter currently employed in experimental procedure is demonstrated. The small increase in transmission at low wavelengths for the yellow-filter is highlighted. 117

7.16 The possible packing of the *cis* molecule with nematic 5CB. The angle of the N=N bond is based on the calculated β value from the order parameter conversion. 120

7.17 The order parameter versus (a) temperature and (b) reduced temperature for different *cis* concentrations in both yellow-filtered and irradiated states. The irradiated state increase in *cis* conformer shows a much larger change in order parameter compared to the increase in yellow-filtered increase in *cis* conformer concentration. It is shown that plotting as a function of reduced temperature results in each sample following the same trend as expected. . . . 122

LIST OF FIGURES

- 7.18 (a) The nematic to isotropic phase transition temperature (T_{NI-UV}) as a function of *cis* concentration for UV irradiated samples compared with previous laser irradiated phase transition temperature ($T_{NI-laser}$). The phase transition temperature decreases with increases *cis* concentration. (b) The relative change in phase transition temperature as a function of *cis* concentration. LIOM model is fit to establish the change in intermolecular interaction energy. (c) Comparison of irradiated and yellow-filtered relative change in phase transition temperature as a function of *cis* concentration, clearly highlighting the different dependencies. 124
- 8.1 (a) The dependence of permittivity on voltage for 0.5%($\frac{w}{w}$) 15NB3OH in 5CB, at a temperature of 20°C. The dielectrics fitting gave parameters of: $k_{11} = 6.98pN$, $k_{33} = 11.54pN$, $\epsilon_{\parallel} = 20.58$, $\epsilon_{\perp} = 6.32$, and $\theta_{tilt} = 2.15^{\circ}$. (b) A comparison of 5CB and 0.5% 15NB3OH in 5CB elastic constants temperature dependence. A slight reduction in k_{33} is observed. (c) A comparison of 5CB and 0.5% 15NB3OH in 5CB parallel and perpendicular electrical permittivity. Very little change is observed from such a small dopant concentration. (b, c) Empirical fitting of equations from [1]. Results are plotted as a function of reduced temperature to remove order parameter discrepancies. 132

- 8.2 (a) The average relative change in splay elastic constant as a function of yellow-filtered *cis* concentration, averaged over $\frac{T}{T_{NI}} = 0.95 \rightarrow 0.99$. An average increase of $(4 \pm 2)\%$ is observed. (b) Depiction of the nematic director deformation occurring in the measurement of the splay elastic constant. The splay restoring force is demonstrated. Possible packing of the *cis* molecules into the splay packing is also shown. (c) The average relative change in the bend elastic constant is shown as a function of yellow-filtered *cis* concentration, averaged over $\frac{T}{T_{NI}} = 0.95 \rightarrow 0.99$. An overall decrease with increasing *cis* concentration is observed. (d) Depiction of the nematic director deformation occurring in the measurement of the bend elastic constant. The bend restoring force is demonstrated. Possible packing of the *cis* molecule into the bend packing is shown. 134
- 8.3 (a) The average relative change in parallel permittivity as a function of yellow-filtered *cis* concentration is shown, averaged over $\frac{T}{T_{NI}} = 0.95 \rightarrow 0.99$. A general decrease with increasing *cis* concentration is observed. (b) The relationship between the director and the measured parallel permittivity is depicted. The packing of the *cis* isomer into this configuration is shown to help draw conclusions on the observed trends. (c) The average relative change in perpendicular permittivity as a function of yellow-filtered *cis* concentration, averaged over $\frac{T}{T_{NI}} = 0.95 \rightarrow 0.99$. (d) The relationship between the director and the measured perpendicular permittivity is depicted. The packing of the *cis* molecule into this configuration is shown to help draw conclusions on the observed results. 136
- 8.4 The average relative change in dielectric anisotropy as a function of yellow-filtered *cis* concentration is shown, averaged over $\frac{T}{T_{NI}} = 0.95 \rightarrow 0.99$. A general decrease with increasing *cis* concentration is observed. 137

LIST OF FIGURES

- 8.5 (a) The average pre-tilt dependence on the yellow-filtered *cis* concentration is shown, averaged over each samples full temperature dataset. After an initial decrease in pre-tilt with the addition of BAAB2 an increase in pre-tilt is observed with increasing *cis* concentration is observed. (b) A depiction of the pre-tilt in the devices measured. The impact of the V-shaped molecule on the director is shown to demonstrate how it could cause an increase in the pre-tilt measured in the device. 138
- 8.6 (a) The average relative change in splay elastic constant dependence on irradiated and yellow-filtered *cis* concentration is shown, averaged over $\frac{T}{T_{NI}} = 0.95 \rightarrow 0.99$. In the irradiated state an overall decrease with increasing *cis* concentration is observed. (b) The splay director deformation is shown with the possible forces acting on the system depicted. (c) The average relative change in bend elastic constant dependence on irradiated and yellow-filtered *cis* concentration is shown, averaged over $\frac{T}{T_{NI}} = 0.95 \rightarrow 0.99$. The irradiated state demonstrates a large decrease with increasing *cis* concentration. (d) The bend director deformation is shown with possible forces acting on the system depicted. 141
- 8.7 (a) The average relative change in parallel permittivity as a function of irradiated and yellow-filtered *cis* concentration, averaged over $\frac{T}{T_{NI}} = 0.95 \rightarrow 0.99$. (b) Depiction of the parallel permittivity measurement with the hypothesised optical torque force direction shown. (c) The average relative change in perpendicular permittivity as a function of irradiated and yellow-filtered *cis* concentration, averaged over $\frac{T}{T_{NI}} = 0.95 \rightarrow 0.99$. An increase is observed with increasing irradiated *cis* concentration. (d) Depiction of the perpendicular permittivity measurement is shown. The impact of an optical torque force acting on the system is shown in the slight reorientation of the director. 143

8.8 (a) The average pre-tilt as a function of irradiated and yellow-filtered *cis* concentration, measured over the full temperature range of each dataset. The irradiated state shows an increase in pre-tilt with increasing *cis* concentration. (b) Depiction of the pre-tilt measurement is shown with the effect of an optical torque acting on the system demonstrated by an increase in the director reorientation. 144

9.1 (a) *cis* concentration measured with respect to time for 2%($\frac{w}{w}$) BAAB2 together with 15NB3OH in 5CB. The first dashed line at t=5s represents the UV switch on time, whilst the second dashed line at t=60s represents the UV switch off time. (b) A closer look at the active photoisomerisation section with the UV switched on at t=5s and saturation of *cis* molecules achieved within 10s. (c) The photoisomerisation rate as a function of temperature measured via a linear fit of (b). 149

9.2 (a) The decay of the *cis* molecules after the UV is switched off. (b) The decay rate of the *cis* conformer into the *trans* conformer as a function of temperature measured via an exponential decay fit to (a). 150

9.3 (a) The order parameter versus time for 2%($\frac{w}{w}$) BAAB2 together with 15NB3OH in 5CB. The first dashed line at t=5s represents the UV light being switched on, whilst the dashed line at t=60s represents the UV light being switched off. (b) The maximum and minimum order parameters measured for various temperature in the time dependent experiment compared with the order parameter versus temperature scan conducted in chapter 7.3. (c) A closer look at the time dependence of the order parameter during the active photoisomerisation process. (d) A closer look at the order parameter recovery during the relaxation of *cis* conformers to the *trans* conformal state. 152

LIST OF FIGURES

9.4	Time dependence of (a) Capacitance and (b) <i>cis</i> molar concentration for 3%($\frac{w}{w}$) BAAB2 together with 0.5%($\frac{w}{w}$), with UV irradiation and yellow-filtered visible irradiation points labelled. (c) The time dependence of capacitance for 2%($\frac{w}{w}$) BAAB2 together with 0.5%($\frac{w}{w}$) post UV irradiation with no yellow-filtered visible light illuminating the system.	153
10.1	The absorption spectrum for BAAB2 dissolved in acetone is shown. The absorption peaks correspond to the <i>trans</i> and <i>cis</i> conformer excitations. The overlap of the laser wavelength with the <i>trans</i> excitation is shown.	161
10.2	(a) The nematic to isotropic transition temperature is evaluated for varying concentration of BAAB2 in 5CB for a variety of irradiation conditions. The blue highlighted zone is the switchable regime in which irradiation with the 405nm laser will result in an isothermal phase transition. (b) The nematic to isotropic transition temperature for 10%($\frac{w}{w}$) BAAB2 in 5CB as a function of broadband white light intensity is shown. The transition temperature decreases with increasing broadband intensity and an exponential decay is fit to guide the eye.	162
10.3	The transmission and blocking spectra for the BAAB2 doped 5CB device is demonstrated.	164
10.4	(a) The response time for 5%($\frac{w}{w}$) and 10%($\frac{w}{w}$) BAAB2 in 5CB as a function of (a) temperature and (b) reduced temperature. (c) The response time dependence of 10%($\frac{w}{w}$) BAAB2 in 5CB on laser intensity.	166

Chapter 1

Motivation and direction

The hypothesis of this thesis was simple at the outset:

”Liquid crystal switchable optical devices.”

The amazing electro-optical properties of LCs continually prove to be an excellent foundation for switchable optics, from display to lens applications, and therefore is an excellent starting point for the development of switchable optics. As time progressed the investigation became focussed on the development of switchable optical shutters, and more specifically optical shutters which could protect cameras or eyesight against laser damage. The increased accessibility of high-powered hand-held lasers has caused a growth in the number of laser incidents surround pilots, cameras, and general retina damage. It is logical to simply apply the selective transmission achieved in many liquid crystal modes/devices to the selective rejection of these damaging laser wavelengths.

This PhD began with the investigation into an electrically switchable and tuneable liquid crystal Lyot filter for laser protection [1]. The exceptional potential for this liquid crystal based optical shutter to provide transmission and blocking modes for cameras and eyesight, providing protection against damaging laser wavelengths, was shown. However, the need of an electric field across the device to switch into protection mode seemed somewhat limiting, requiring an external sensor to tell the system when the laser threat was impacting the system.

1. MOTIVATION AND DIRECTION

Therefore, the research then progressed onto photosensitive materials coupled to liquid crystal systems.

The doping of a typical nematic liquid crystal with an azobenzene-based liquid crystal material was undertaken and the ability for the system to switch between a transmission mode and blocking mode via irradiation of the system with the laser "threat" was considered. The laser-light triggered an isothermal phase transition in the nematic system which switched the device between a twisted nematic and isotropic device, providing automatic switching from transmission to blocking mode [2]. In investigating this photosensitive system many interesting effects were observed, namely the light-induced order modification, and therefore much of the later research in this PhD surrounded untangling the underlying physical mechanisms involved in the light-induced effects observed and its impacts on the physical properties of the system.

This thesis will begin with the introduction of the fundamental physics surrounding liquid crystal phases and key anisotropic properties in chapter 2. Chapter 3 will then introduce the underlying theory of dichroic dyes before taking a close look at the impact of light-sensitive azobenzene based materials on liquid crystals. The experimental methods utilised in the investigation of these materials and devices will then be described in chapter 4 before diving into the experimental results and discussion half of this thesis.

Chapter 5 will describe the investigation into the electrically switchable liquid crystal Lyot filter utilised for laser protection. A slight detour from specific optical protection devices will then be taken with the investigation into some dichroic dye-doped liquid crystal systems in chapter 6. Chapter 7-9 will then describe the investigation into the underlying physical mechanisms involved in the azobenzene doped nematic liquid crystal system, before finally demonstrating the potential for the system to act as an automatic all-optical switchable laser protection device in chapter 10. The thesis will then be summarised and your freedom granted.

References

- [1] E. I. L. Jull and H. F. Gleeson. Tuneable and switchable liquid crystal laser protection system. *Applied Optics*, 56(29):8061–8066, 2017. [1](#)
- [2] E. I. L. Jull and H. F. Gleeson. All-optical responsive azo-doped liquid crystal laser protection filter. *Optics Express*, 26(26):34179–34184, 2018. [2](#)

REFERENCES

Chapter 2

Fundamentals of liquid crystals

Liquid crystals (LC) are a wondrous subset of soft matter physics with intriguing anisotropic properties that combine with light to generate beauty down the microscope, although this typically only happens in the case of poor alignment. This chapter hopes to give a fundamental understanding of the background physics of LC materials, from their place in the phase diagram to quantification of key anisotropic properties such as order parameter, elastic constants, and dielectric permittivity. This chapter is by no means all of the amazing physics of LCs, but hopes to give an excellent foundation for the mechanisms discussed later in this thesis.

2.1 Introduction

LC materials exhibit a phase of matter between isotropic liquid and solid crystalline (figure 2.1), the discovery of which is attributed to F. Renitzer [1]. This phase has liquid-like fluidity, whilst still retaining long range orientational order similar to the order in crystalline materials (unlike isotropic liquids which have no long-range order). LC phases can be largely split into two categories: thermotropic LCs which form as a function of temperature due to molecular geometrical anisotropy and lyotropic LCs which form as a function of amphiphilic molecule concentration in a solvent.

2. FUNDAMENTALS OF LIQUID CRYSTALS

This thesis will focus specifically on investigation into calamitic thermotropic LCs. Calamitic phases are formed from rod-shaped (elongated) molecules. To form a LC phase they typically require a length to width ratio of $\geq 4:1$.

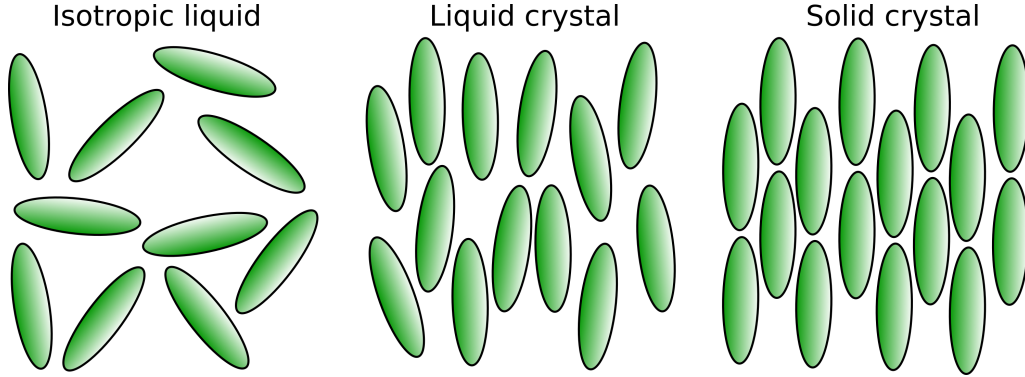


Figure 2.1: The isotropic liquid, LC, and solid crystal phases of matter are depicted. The isotropic liquid exhibits short-range positional order and fluidity. LC phases exhibit long range order (orientational) and fluidity. Solid crystal phases exhibit long range positional order, but are unable to flow.

2.2 Liquid crystal phases

LC phases that form from calamitic molecules do so as a function of temperature and upon cooling from the isotropic liquid phase the LC material will transition into the nematic phase (figure 2.2(a)). The nematic phase has long-range orientational order, the mesogens on average point in a preferred direction denoted the director \underline{n} , but still retain liquid fluidity (the molecules can flow past each other). The molecules are axially symmetric, $\underline{n} = -\underline{n}$, and have no positional order. In the isotropic phase LC materials do not exhibit long range order, however there are some notable short-range ordering effects observed (not observed in non-anisotropic materials), which are discussed in detail in [2, 3].

Cooling further, LC materials can exhibit the smectic-A phase. In the smectic-A phase the molecules' form a layer-like structure (positional order). This is

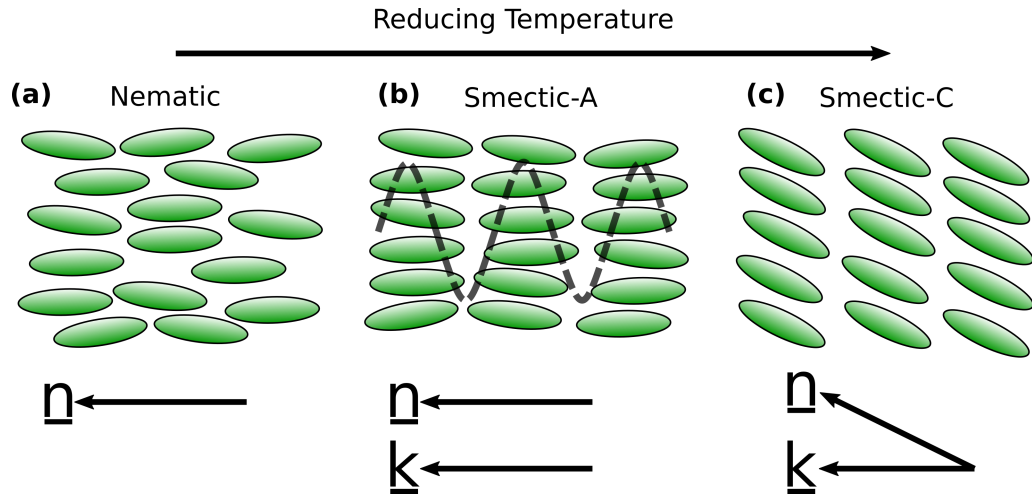


Figure 2.2: The (a) nematic, (b) smectic-A, and (c) smectic-C phases are shown. The director and layer normal are denoted n and k .

described by a 1-dimensional density wave in which the molecules centre of mass on average falls along the layers, this is shown in figure 2.2(b). The director is parallel to the layer normal \underline{k} in this phase. Further cooling can lead to the smectic-C phase which is similar to the smectic-A phase except the director is now at an angle to the layer normal, as shown in figure 2.2(c).

Chirality

Chirality is the property in which the mirror image of an object cannot be superimposed on the original, as shown in figure 2.3(a). This is common in organic chemistry and occurs in some LC materials, or can be induced by the addition of a chiral dopant to a nematic LC. Chirality in LCs generates the chiral nematic or cholesteric phase in which the director rotates through the sample forming a helicoidal structure, see figure 2.3(b). Further detail on the chiral nematic phases and properties are described by Dierking [4].

2. FUNDAMENTALS OF LIQUID CRYSTALS

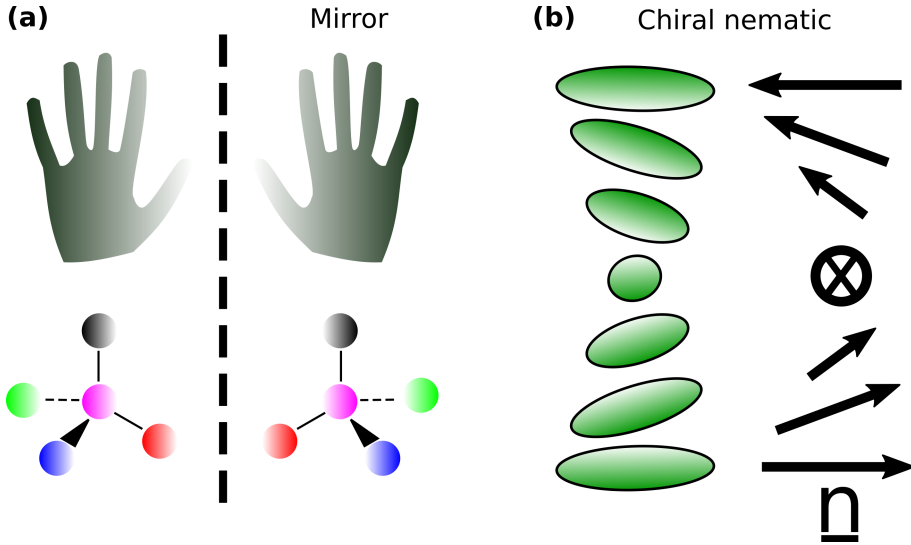


Figure 2.3: (a) Chirality is shown to be when the mirror image cannot be superimposed upon the original object. (b) The chiral nematic (cholesteric) phase is shown in which the director rotates through the sample forming a helicoidal structure.

2.3 Order parameter

The formation of the nematic phase on cooling from the isotropic phase can be considered as simply an increase in the order of the system. To give a quantification of this the order parameter (S) is defined as a function which will be zero in the isotropic phase and non-zero in the nematic LC phase [5]. If a simple rod with cylindrical symmetry is considered, figure 2.4, it can be defined by a unit vector \mathbf{a} which can be written in terms of its polar vectors:

$$\begin{aligned} a_x &= \sin(\theta)\cos(\phi), \\ a_y &= \sin(\theta)\sin(\phi), \\ a_z &= \cos(\theta). \end{aligned} \tag{2.1}$$

If the director \underline{n} is considered along the z-axis the overall rod alignment can be described by a distribution function, $f(\theta, \phi)d\Omega$, which defines the probability of finding the rods in the angle $d\Omega = \sin\theta d\phi$ around (θ, ϕ) .

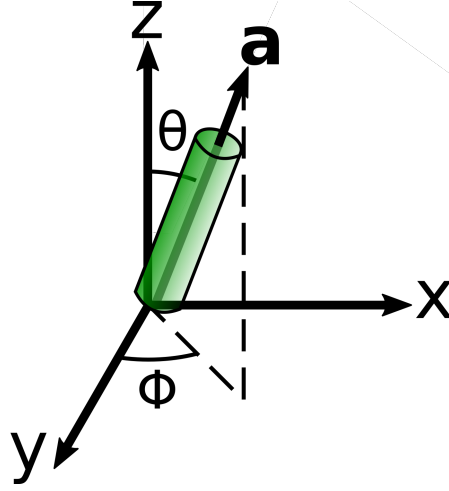


Figure 2.4: The model of simple rods used to generate a numerical order parameter, θ is the angle between the director (z-axis) and the rods vector (\mathbf{a}), whilst ϕ is the angle in the x-y plane.

The cylindrical symmetry of the nematic director requires the distribution function to be independent of ϕ ; $f(\theta, \phi) = f(\theta)$. The uniaxial nature of nematics, $\underline{n} = -\underline{n}$, means that $f(\theta) = f(\pi - \theta)$.

The first multipole which gives a non-trivial result when the nematic characteristics are considered is given by [5]:

$$S = \frac{1}{2} \langle (3\cos^2\theta - 1) \rangle = \int (f(\theta)) \frac{1}{2} (3\cos^2\theta - 1). \quad (2.2)$$

If the distribution function is constrained at $\theta=0$ or π (along the director) this will result in $\cos\theta = \pm 1$ which gives an $S=1$. If however $\theta=\frac{\pi}{2}$ (perpendicular to the director) then you get a negative order parameter of $S=-\frac{1}{2}$. Finally, if the system is isotropic, randomly oriented, $\langle \cos^2(\theta) \rangle = \frac{1}{3}$ and therefore $S=0$ as expected in the isotropic phase. These values of S are consistent with the required conditions first set out for a nematic LC and therefore equation 2.2 gives an useful quantification of the order of the system.

2.4 Refractive indices and birefringence

The refractive indices of any material are described by its refractive index ellipsoid or Fresnel ellipsoid shown in figure 2.5 [6]. The ellipsoid describes how the dielectric susceptibility (χ), and therefore the refractive index (n) varies depending on the propagation direction through the material.

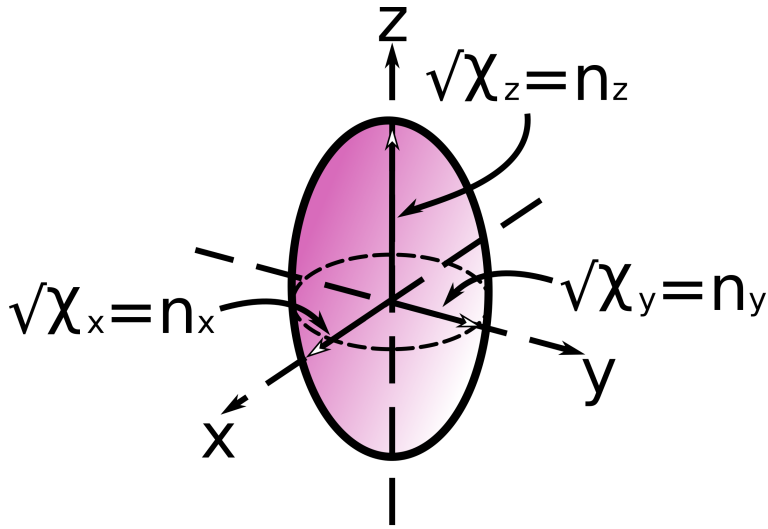


Figure 2.5: The Fresnel or refractive index ellipsoid is shown. This demonstrates the dielectric susceptibility of the material in all directions and shows how the refractive index will be different depending on the propagation direction.

In uniaxial LC materials there are typically two values of dielectric susceptibility, χ_{\parallel} and χ_{\perp} which are parallel and perpendicular to the director [7]. These are related directly to the extraordinary ($n_e = \sqrt{\chi_{\parallel}}$) and ordinary ($n_o = \sqrt{\chi_{\perp}}$) refractive indices. For light propagating at an arbitrary angle (ψ) to the optic axis of the material the refractive index ellipsoid can be used to obtain the effective birefringence of the material by taking the cross-section of the ellipse perpendicular to the direction the light is propagating. The difference in refractive index results in an effective birefringence ($\Delta n = n_x - n_o$), with n_x being the combination of n_e and n_o (equation 2.3) and n_o the perpendicular component.

2.4 Refractive indices and birefringence

$$\frac{1}{n_x^2(\psi)} = \frac{\sin^2\psi}{n_o^2} + \frac{\cos^2\psi}{n_e^2}, \quad (2.3)$$

The propagation of light in an anisotropic medium is crucial to the observation and characterisation of LC materials. The interaction of plane-polarised light with the medium is dependent on the angle between the polarisation (electric field vector) and the optic axis of the material. If the polarisation is parallel or perpendicular to the LC optic axis (parallel to n_e or n_o) then there is no change in the polarisation state of the light. However, if the polarisation is at any other angle the electric field decomposes into the two modes (n_e and n_o). Due to the difference in refractive index each component will propagate at different speeds, resulting in a phase difference [8]. Upon leaving the anisotropic medium the recombination of the modes results in a retardance (Γ) applied to the polarised light which is given as:

$$\Gamma = \frac{2\pi\Delta nd}{\lambda}, \quad (2.4)$$

where d is the cell gap (or light path) and λ is the wavelength. It is important to note here that in a system in which the director varies throughout the device (e.g. a planar device with an applied electric field) the effective birefringence is made of the sum of different n_x values through the layers.

Refractive index dispersion

When investigating LC refractive indices it is important to consider the wavelength dispersion, described in detail in any standard optics text book, such as Hecht [9]. The refractive index is dependent on the wavelength of light due to the coupling of the light's electric field with electron oscillations. This typically manifests itself as an increase in refractive index with decreasing wavelength, see for example figure 2.6 of typical nematic LC wavelength dispersion of refractive indices. There are many models which successfully predict the wavelength dispersion of material's refractive indices and in this thesis the extended Cauchy model is typically employed [10] as we typically limit ourselves to the visible spectrum.

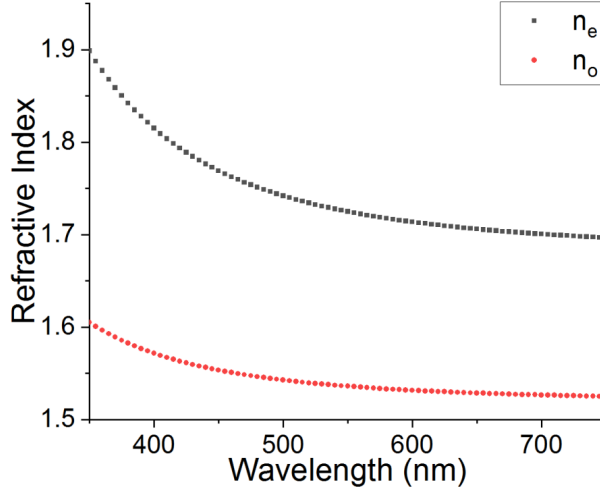


Figure 2.6: The wavelength dispersion of n_e and n_o for nematic LC *4-pentyl-4'-cyanobiphenyl* (5CB). Data acquired from extended Cauchy model fit parameters [10].

2.5 Elastic properties

In a fluid there are no restoring forces generated from the positional displacement of molecules as they are simply able to flow past each other. Therefore, with the elastic properties of nematic LCs (an incompressible fluid), the elastic forces generated from director curvature are instead considered. The elastic properties from director deformations were first described by Oseen [11] and later developed further by Frank [12].

If a Cartesian system is considered with the director parallel to the z -axis, allowing the director to vary its angle locally results in six curvature possibilities, depicted in figure 2.7. The free energy, G , of a LC system is given as the volume integral of the free energy density g :

$$G = \int_{\nu} g d\nu. \quad (2.5)$$

$$g = k_i a_i + \frac{1}{2} k_{ij} a_i a_j, \quad (2.6)$$

where a is the curvature components (s_1, t_1, \dots) and k are the elastic moduli.

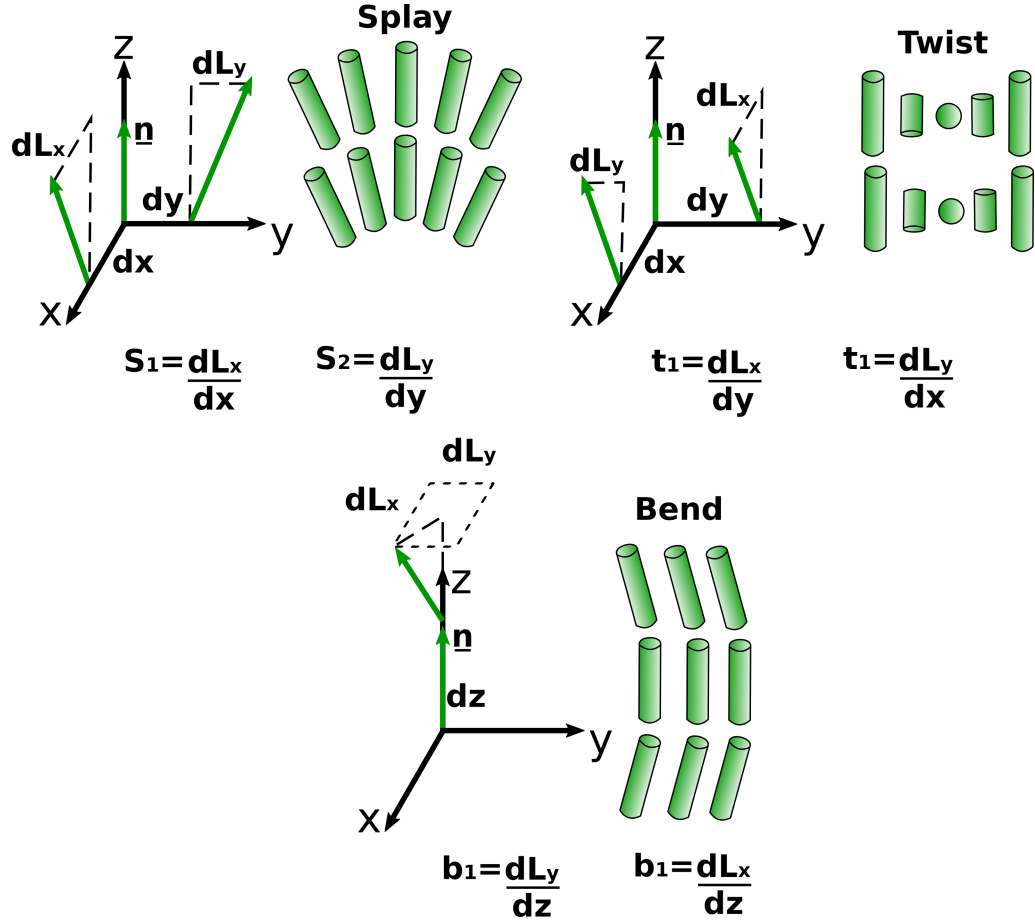


Figure 2.7: The possible torsional deformations available in the LC director. The director n is parallel with the z-axis of the Cartesian frame.

If the co-ordinate system is replaced, such that (x, y, z) is replaced with any other co-ordinate system (x', y', z') the free energy density function and curvature components (g and a'_i) must have the same function. The non-zero terms of the free energy can be isolated by using the following assumptions in the nematic phase (described in further detail [12]):

- Uniaxial symmetry around z-axis (i.e. $x' = y, y' = -x$, and $z' = z$)

2. FUNDAMENTALS OF LIQUID CRYSTALS

- Non-polar molecules, $\underline{n} = -\underline{n}$ (i.e. $x' = x$, $y' = -y$, and $z' = -z$)
- Absence of chirality (i.e. $x' = x$, $y' = -y$, and $z' = z$)

With these assumptions the non-zero terms are isolated giving the following free energy equation:

$$g' = \frac{1}{2}k_{11}(s_1 + s_2 - s_0)^2 + \frac{1}{2}k_{22}(t_1 + t_2 - t_0)^2 + \frac{1}{2}k_{33}(b_1^2 + b_2^2) + k_{12}(s_1 + s_2)(t_1 + t_2) - (k_{22} + k_{24})(s_1s_2 + t_1t_2), \quad (2.7)$$

where $s_0 = \frac{-k_1}{k_{11}}$, $t_0 = \frac{-k_2}{k_{22}}$, $g' = g + \frac{1}{2}k_{11}s_0^2 + \frac{1}{2}k_{22}t_0^2$.

k_{11} , k_{22} , and k_{33} are the bulk splay, twist, and bend deformations. k_{12} and k_{24} are the surface saddle-splay and splay-bend deformations. In this thesis only the standard bulk splay, twist, and bend elastic constants are considered.

2.6 Director deformation under electric fields

LCs molecular anisotropy typically results in two dielectric permittivities parallel (ϵ_{\parallel}) and perpendicular (ϵ_{\perp}) to the optical axis. This results in a dielectric anisotropy, $\Delta\epsilon = \epsilon_{\parallel} - \epsilon_{\perp}$, which when positive ($\Delta\epsilon > 0$) means that the director will reorient to align parallel with an applied electric field.

If a planar aligned nematic LC is considered (figure 2.8(a)), in which the director is uniform along the glass substrate in the y-direction, in the absence of an applied electric field (voltage) the director will be homogeneous. However, if a sufficiently large voltage is applied across the device it will cause a reorientation of the nematic director. However, due to the surface anchoring conditions, typically assumed to be infinitely strong with a pre-tilt angle (θ_{tilt}) of 0° , the application of a voltage will induce a non-uniform director distribution through the cell in the z-direction. This non-uniform distribution in director, depicted in figure 2.8(b, c) results in elastic restoring forces (splay and bend). This means that by indirectly measuring the response of the director to an applied electric field, numerical analysis can obtain dielectric and elastic properties of the nematic material.

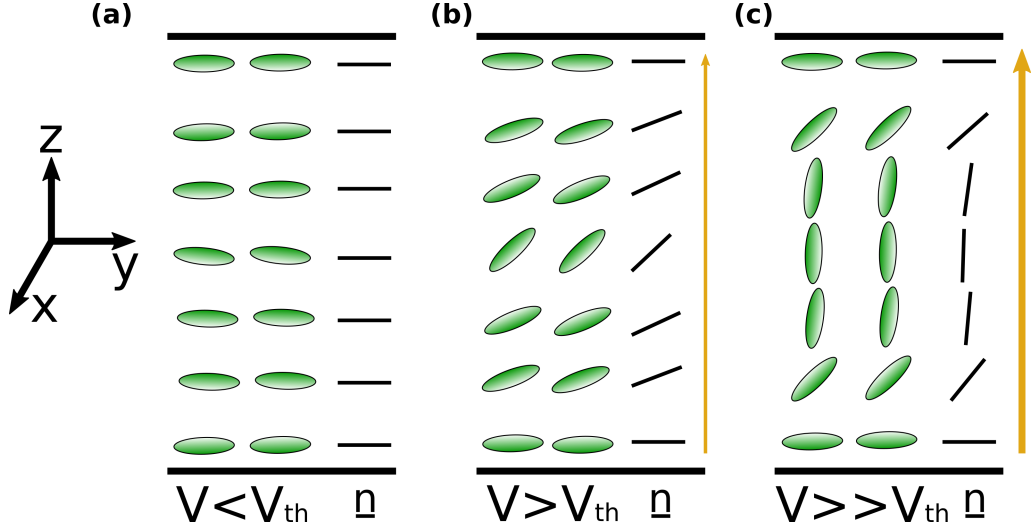


Figure 2.8: A planar aligned nematic is depicted. (a) In the low voltage state, $V < V_{th}$ the director field remains uniform. (b) At just above the threshold voltage the director field in the centre of the device begins to reorient and the splay elastic force dominates. (c) At voltages much greater than the threshold voltage the director reorients to be approximately homeotropic, although anchoring prevents this at the surfaces.

The analysis of the deformation to a nematic director under an applied electric field is described in detail by Dueling [13] and Welford [14]. To begin requires the minimisation of the Gibbs free energy:

$$G = \int_0^L (F_{el} + F_{diel}) dz, \quad (2.8)$$

where the elastic free energy (F_{el}) is given by:

$$F_{el} = \frac{1}{2} \left(\frac{d\Psi}{dz} \right)^2 (k_{11} \cos^2(\Psi) + k_{33} \sin^2(\Psi)), \quad (2.9)$$

with Ψ being the z -dependant director angle. The electric field free energy (F_{diel}) is given by

$$F_{diel} = -\frac{1}{2} \epsilon_0 E^2 (\epsilon_{\parallel} \sin^2(\Psi) + \epsilon_{\perp} \cos^2(\Psi)), \quad (2.10)$$

2. FUNDAMENTALS OF LIQUID CRYSTALS

where ϵ_0 is the permittivity of free space. Setting the boundary pre-tilt conditions at 0° this means that $\Psi(z = 0) = \Psi(z = L) = 0$ leads to the following relationship:

$$\frac{V}{V_{th}} = \frac{2}{\pi} \sqrt{(1 + \gamma \sin^2(\Psi_m))} \int_0^{\Psi_m} \sqrt{\frac{1 + \kappa \sin^2(\Psi)}{(1 + \gamma \sin^2(\Psi))(\sin^2(\Psi_m) - \sin^2(\Psi))}} d\Psi, \quad (2.11)$$

and as Ψ_m is the maximum pre tilt occuring at $\Psi_m = \Psi(z = \frac{L}{2})$,

$$\frac{2z}{L} \int_0^{\Psi_m} \sqrt{\frac{(1 + \kappa \sin^2(\Psi))(1 + \gamma \sin^2(\Psi))}{(\sin^2(\Psi_m) - \sin^2(\Psi))}} d\Psi = \int_0^{\Psi} \sqrt{\frac{(1 + \kappa \sin^2(\Psi))(1 + \gamma \sin^2(\Psi))}{(\sin^2(\Psi_m) - \sin^2(\Psi))}} d\Psi, \quad (2.12)$$

where the threshold voltage V_{th} , γ , and κ are given by:

$$\begin{aligned} V_{th} &= \pi \sqrt{\frac{k_{11}}{\epsilon_0(\epsilon_{\parallel} - \epsilon_{\perp})}}, \\ \gamma &= \frac{\epsilon_{\parallel} - \epsilon_{\perp}}{\epsilon_{\perp}}, \\ \kappa &= \frac{k_{33} - k_{11}}{k_{11}}. \end{aligned} \quad (2.13)$$

This model allows prediction of the director deformation under an applied electric field in terms of the elastic and dielectric properties of the LC. If knowledge of the director field deformation is known then the application of an electric field can be used to deduce the dielectric and elastic properties of a LC material. In practice, measurement of the director field is difficult, however measurement of the capacitance (C) which can be directly related to the director field is easily achieved (indirect measurement of the director field). It was shown by Gruler [15] that the capacitance could be related the the director angle, elastic constants, and dielectric properties via the following equation:

$$C = \frac{\epsilon_0 \epsilon_{\perp}}{L} \frac{\int_0^{\Psi_m} \sqrt{\frac{(1 + \kappa \sin^2(\Psi))(1 + \gamma \sin^2(\Psi))}{(\sin^2(\Psi_m) - \sin^2(\Psi))}} d\Psi}{\int_0^{\Psi_m} \sqrt{\frac{(1 + \kappa \sin^2(\Psi))}{(1 + \gamma \sin^2(\Psi))(\sin^2(\Psi_m) - \sin^2(\Psi))}} d\Psi} \quad (2.14)$$

Equation 2.14 coupled with equation 2.11 allows fitting of capacitance versus voltage curves to deduce dielectric and elastic properties of LC materials and mixtures.

2.7 Summary

This chapter has introduced the fundamental physics surrounding LCs giving a foundation for later discussions in this thesis. The position of LCs in the phase diagram has been demonstrated and the subsets of LC phases has been introduced. The order parameter was defined, critical in later chapters which investigate light-induced order modification.

Some key anisotropic properties of LCs were introduced including, birefringence, dielectric anisotropy, and elastic properties. These are by no means the only interesting properties of LC materials, however they are the key features utilised in investigating specialist materials in this thesis. Finally, the theory surrounding the director response to an applied electric field was introduced which allows measurements of the voltage dependency of LC capacitance to be related to their elastic and dielectric properties.

In the next section a focussed look at dichroic dyes and their interactions with LCs will be introduced. This will give a fundamental understanding of the guest-host interaction as well as the coupling of light to LC systems.

References

- [1] F. Reinitzer. Beiträge zur Kenntniss des Cholesterins. *Monatshefte für Chemie*, 9(1):421–441, 1888. [5](#)
- [2] P. G. de Gennes. Short range order effects in the isotropic phase of nematics and cholesterics. *Molecular Crystals and Liquid Crystals*, 12:193–214, 1971. [6](#)
- [3] N. V. Madhusudana and S. Chandrasekhar. Short range order in the isotropic phase of nematic liquid crystals. *Solid State Communications*, 13:377–380, 1973. [6](#)
- [4] I. Dierking. Chiral liquid crystals: structures, phases, effects. *Symmetry*, 6:444–472, 2014. [7](#)
- [5] P. G. de Gennes. *The Physics of Liquid Crystals*. Oxford University Press, 1974. [8](#), [9](#)
- [6] A. Yariv and P. Yeh. *Optical waves in crystals*. Wiley, 2002. [10](#)
- [7] D. Andrienko. Introduction to liquid crystals. *Journal of Molecular Liquids*, 267:520–541, 2018. [10](#)
- [8] D-K. Yang and S-T. Wu. *Fundamentals of Liquid Crystal Displays*. Wiley, 2006. [11](#)
- [9] E. Hecht and A. Zajac. *Optics*. Pearson, 1980. [11](#)
- [10] J. Li and S-T. Wu. Extended Cauchy equations for the refractive indices of liquid crystals. *Journal of Applied Physics*, 95(3):896–901, 2004. [xv](#), [11](#), [12](#)
- [11] C. W. Oseen. The theory of liquid crystals. *Transactions of the Faraday Society*, 29:883–899, 1933. [12](#)
- [12] F. C. Frank. On the theory of liquid crystals. *Discussions of the Faraday Society*, 25:19–28, 1958. [12](#), [13](#)

REFERENCES

- [13] H. J. Deuling. Deformation of nematic liquid crystals in an electric field. *Molecular Crystals and Liquid Crystals*, 19(2):123–131, 1972. [15](#)
- [14] K. R. Welford and J. R. Sambles. Analysis of electric field induced deformations in a nematic liquid crystal for any applied field. *Molecular Crystals and Liquid Crystals*, 147(1):25–42, 1987. [15](#)
- [15] H. Gruler, T. J. Scheffer, and G. Meier. Elastic constants of nematic liquid crystals. *Naturforsch*, 27a:966–976, 1972. [16](#)

REFERENCES

Chapter 3

Dyes and photoisomerisation

In the previous chapter the fundamentals of liquid crystal (LC) physics were described. In this chapter a detailed look into dichroic dyes and the guest-host effect will be conducted. The underlying theory of guest dye order coupling with the host LC order parameter will be established. This will then be followed by a discussion surrounding optically induced nonlinearities in azo-dye doped nematic LCs. The theoretical explanation behind light-induced molecular reorientation (LIMR) and light-induced order modification (LIOM) will then be discussed.

3.1 Dichroic dyes

Dichroic dyes exhibit an absorption anisotropy (polarisation angle dependent absorption). This is a result of the relationship between the transition dipole moment (TDM) and the molecular long-axis of the dye molecule. There are two broad categories of dichroic dye: L-dyes and T-dyes. L-dyes (longitudinal) have a TDM roughly parallel with the long axis of the molecule, although it is typically at an arbitrary angle β . T-dyes (transverse) have a TDM approximately perpendicular to the molecular long axis. This thesis focusses on the combination of longitudinal dyes with LCs.

An example of an L-dye (anthraquinone) used in this study is shown in figure 3.1, demonstrating the relationship between the TDM and molecular long-axis.

3. DYES AND PHOTOISOMERISATION

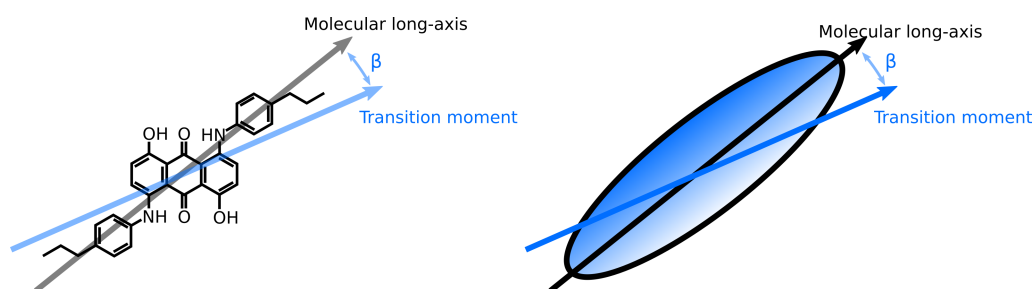


Figure 3.1: Anthraquinone dichroic dye (15NB3OH) is shown with the relationship between molecular long-axis and TDM (absorption axis) demonstrated. The angle $\beta = 15.9^\circ$ is calculated from time-dependent density functional theory [1].

The coupling of dichroic dye orientation with the LC director was first observed by Helmeier and Zanoni in 1968 [2], in which the orientation, and therefore absorption properties, of methyl-red dye was directly controlled by manipulation of the LC director with an applied electric field. This phenomenon is known as the guest-host effect, in which the dichroic dye (guest) is oriented with the molecular long-axis along the LC (host) director. The ability to control the LC orientation via external stimuli meant that this guest-host effect led to many switchable optical devices being proposed, the first of which was demonstrated by White and Taylor [3]. A good review of past and present developments in guest-host systems is given by M. T. Sims [4]. Optical properties of guest-host device are dependant on:

- bulk LC order,
- coupling of dichroic dye with host order,
- order parameter of the dichroic dye,
- dye TDM angle with respect to its long axis,
- absorption coefficient of the dye,
- dichroic dye solubility in LC host.

3.1.1 Dye types and properties

The physical properties of dichroic dyes are dependent on both their chemical structure and the host LC they are doped into. There are broadly two common categories of dichroic dye utilised in guest-host devices: azo-dyes and anthraquinone-dyes. Here their physical properties will be briefly discussed.

Azobenzene-based dichroic dyes depicted in figure 3.2(a) are typically synthesised to generate L-dyes. A comprehensive description of various azo-dyes is given by Bahadur [5]. Azo-dyes demonstrate high order parameters when doped in nematic LCs ($0.5 \rightarrow 0.8$) [6], and high solubility ($2 - 3\%(\frac{w}{w})$) when compared with other dichroic dye types [4, 7, 8]. Higher solubility leads to an increase in colour due to higher levels of overall absorption making these dyes desirable for display applications. However, azo-dyes have a notoriously low photo-stability and degrade rapidly, with UV/blue absorbing azo-dyes degrading at a faster rate than red/yellow absorbing azo-dyes [5].

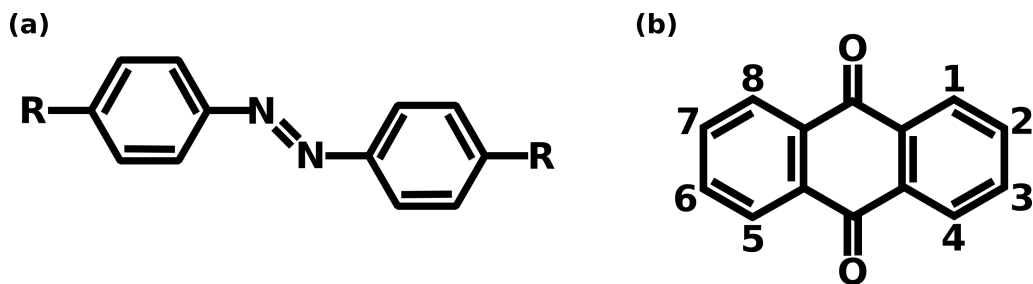


Figure 3.2: The basic chemical foundation of (a) azo-dyes and (b) anthraquinone-dyes. Chemical substitutions can modify the physical properties of these dichroic dyes.

Anthraquinone-based dyes, depicted in figure 3.2(b), can be synthesised to generate both L- and T-dyes. These dyes typically have lower absorption coefficients, and a slightly reduced order parameter compared to their azo-dye counterpart. However, anthraquinone dyes are incredibly attractive in display applications due to their high photo-stability compared with azo-dyes [9]. The main drawback of anthraquinone based dyes is their low solubility, typically

3. DYES AND PHOTOISOMERISATION

< 1% [8, 10], something that will be explored later in this thesis.

3.1.2 Dichroism and the order parameter

The addition of such small quantities of dichroic dyes to LCs only slightly modifies the physical parameters of the mixture. The optical properties of the mixtures can change dramatically, however the dielectric permittivity, phase diagram, order, and viscoelastic properties remain largely unchanged, mostly due to the low concentrations used due to the dichroic dye's typically low solubility in LCs [10].

The coupling of the the dichroic dye orientation with the LC director allows direct insight into the order of the system via optical spectroscopy of the mixture. If the dye-doped guest host system is considered, figure 3.3, it can be stated that the LC order parameter and the dye order parameter are given as:

$$\begin{aligned} S_{LC} &= \frac{1}{2} \langle 3 \cos^2(\theta_{host}) - 1 \rangle, \\ S_D &= \frac{1}{2} \langle 3 \cos^2(\theta_{dye}) - 1 \rangle. \end{aligned} \quad (3.1)$$

where θ_{host} and θ_{dye} are the angle the host and dye molecular long axis makes with respect to the director respectively (as discussed in chapter 2.3). These are the definitions of the molecule's order parameter, however if we now define the order parameter of the TDM:

$$S_{TDM} = \frac{1}{2} \langle 3 \cos^2(\theta_{TDM}) - 1 \rangle, \quad (3.2)$$

where θ_{TDM} is the angle between the TDM and the LC director. Note that due to the angle between the dye's molecular long axis and the TDM, β , $S_{TDM} \neq S_D$.

With this in mind the absorption of light at any angle ψ from the director is given as [11]:

$$A(\beta, \psi) = \alpha dc \left[\left(\frac{S_D}{2} \right) \sin^2(\beta) + \left(\frac{1 - S_D}{3} \right) + \left(\frac{S_D}{2} \right) (2 - 3 \sin^2(\beta) \cos^2(\psi)) \right], \quad (3.3)$$

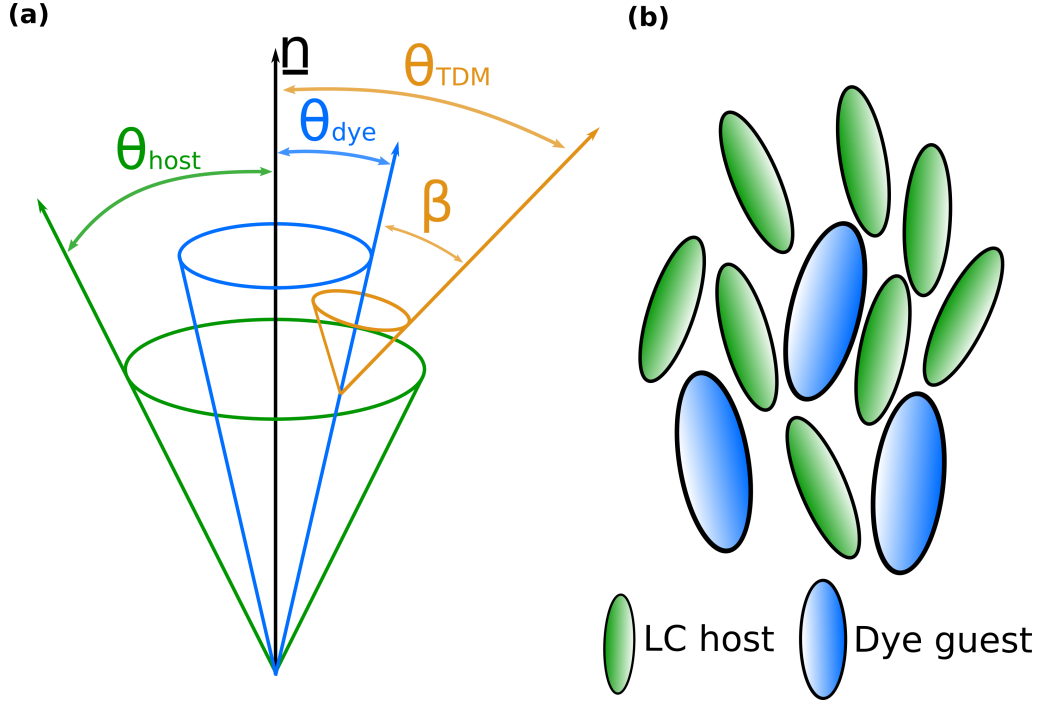


Figure 3.3: (a) The model of a guest-host system is shown. The director is in the z -direction. The LC host can vary by an angle θ_{host} away from the director and the dichroic dye can vary away from the director by an angle θ_{dye} . The dichroic dye TDM varies by an angle β away from the dye's long axis. (b) A depiction of the standard dichroic dye guest-host system. The dichroic dye molecules align with the LC host. The sizes of the molecules are representative of the chemical structure, with the dye 15NB3OH being slightly larger than host 5CB.

where α is absorption coefficient of the TDM, d is the cell gap (light path), and c is the concentration. Now if this is simplified to the case of light absorption with polarisation parallel and perpendicular to the director $\psi = 0^\circ$ and $\psi = 90^\circ$ ($\cos^2(\psi) = 1$ or 0) respectively:

$$\begin{aligned} A_{\parallel} &= 2 + 4S_D - 6S_D \sin^2(\beta), \\ A_{\perp} &= 2 - 2S_D + 3S_D \sin^2(\beta). \end{aligned} \quad (3.4)$$

The dichroic ratio, D , is defined as [12]:

$$D = \frac{A_{\parallel}}{A_{\perp}}, \quad (3.5)$$

3. DYES AND PHOTOISOMERISATION

and the TDM order parameter can be experimentally found via [13–15]:

$$S_{TDM} = \frac{D - 1}{D + 2}. \quad (3.6)$$

Now combining equation 3.4, equation 3.5, and equation 3.6 it can be shown that:

$$S_{TDM} = \frac{D - 1}{D + 2} = S_D \frac{1}{2} (2 - 3 \sin^2(\beta)) = S_D \frac{1}{2} (3 \cos^2(\beta) - 1). \quad (3.7)$$

This assumes that the angle between the TDM and dye molecular long axis is fixed, although in some cases the flexibility of linking groups can cause this to fluctuate [16]. In this thesis the molecular dynamics simulation results will be utilised for β values [1].

Now assuming that the dye order parameter does not vary significantly from the LC order parameter, $S_D \approx S_{LC}$, we can measure the LC host order parameter via absorption spectroscopic measurements:

$$S_{LC} = \frac{D - 1}{D + 2} \frac{2}{3 \cos^2(\beta) - 1}. \quad (3.8)$$

This allows for a simple and direct optical measurement of the order parameter of any LC material doped with a suitable dichroic dye, provided the angle β the TDM makes with the dye long axis is known.

3.2 Photoisomerisation

Azobenzene-based molecules, demonstrated in figure 3.4(a), are the basis of much of the photo sensitive LC field. Azo molecules can exist in two structural conformations, *trans* and *cis*, and a photo-induced conformational change can occur if light of specific wavelengths irradiates the material, this phenomenon is known as photoisomerisation [17]. The *trans* conformer is energetically stable (demonstrated in the energy landscape example in figure 3.4(b)) and exhibits absorption due to the $\pi - \pi^*$ transition (typically in the UV wavelength regime depending on the chemical structure). The *cis* isomer is energetically less favourable and exhibits absorption at higher wavelengths (typically visible) corresponding to the $n - \pi^*$ transition.

Photoisomerisation of azo-based molecules begins with irradiation of the molecule into the excited state, followed by relaxation into either the *cis* or *trans* conformational state. The energy landscape of the photoisomerisation process is depicted in figure 3.4(b) and contains four distinct steps:

1. Excitation from the ground state into the excited state.
2. Relaxation to the energy minimum of the excited state.
3. De-excitation from the excited state to the ground state.
4. Relaxation into the energy minima corresponding to the *cis* or *trans* conformer.

As can be seen from the chemical structure depicted in figure 3.4(a) the *trans* state is an elongated rod-like structure, with the possibility to exaggerate this anisotropy depending on the chemical composition of the *R* substituents. The *cis* conformer is a bent V-shaped molecule with a 120° bend angle. The photoisomerisation process is reversible with UV light exciting *trans* state conformers and increasing the *cis* conformer population, whilst visible light excites the *cis* conformer and increases the *trans* population. Without any external photo-stimuli the molecules will thermally decay from the *cis* to the *trans* state.

3. DYES AND PHOTOISOMERISATION

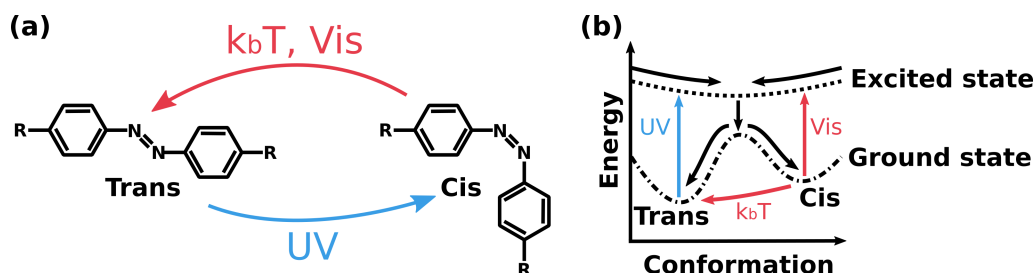


Figure 3.4: (a) The *trans* and *cis* conformers of azobenzene are shown. (b) An example of the energy landscape for the photoisomerisation process is demonstrated.

The anisotropic nature of the azobenzene *trans* conformer leads to an excitation/absorption polarisation sensitivity, due to the TDM lying roughly parallel with the molecular long axis, which leads to some interesting phenomena when coupled with LCs.

3.2.1 Optical nonlinearities in liquid crystals

The first non-linear optical response in LCs was demonstrated by Zeldovich [18] and Zolotko [19], quickly followed by Khoo [20], in which a non-linear shift in refractive index was observed when pumping MBBA with a high intensity laser to induce director re-orientation. This reorientation effect was a coupling of the pump laser's optical electric field with the nematic LC mesogen, this is described in detail by Simoni [21], however here the focus is on the coupling of the photoisomerisation effect with nematic LCs, somewhat different from the high intensity light coupling mechanism.

The photoisomerisation effect was first observed to generate much larger optical nonlinearities, at much lower pump intensities, in azo-dye doped LCs. This was discovered by Khoo [22] in which an incredibly large optical response was induced in methyl-red azobenzene dye doped nematic LC. There are two main mechanisms involved in the effects of photoisomerisation: light-induced molecular reorientation (LIMR) and light-induced order modification (LIOM), each of which will now be discussed in turn.

3.2.2 Light-induced molecular reorientation

As previously stated, the *trans* azobenzene conformer has a polarisation angle-dependent absorption due to the anisotropic nature of the molecule giving a TDM approximately parallel with the long axis of the molecule. This means that the absorption of an excitation photon is proportional to $\cos^2(\psi)$, where ψ is the angle between the TDM and the polarisation of the excitation light. Therefore, molecules with their long-axis aligned with the excitation polarisation have the highest excitation probability. After excitation, the molecule decays back into the ground state *cis* or *trans* conformation (and if *cis* it then thermally relaxes back into *trans*). If the molecule decays/relaxes back into the *trans* state with the long-axis again parallel with the polarisation it will result in a repeat excitation. However, if it relaxes to the *trans* state perpendicular to the polarisation it will not be re-excited.

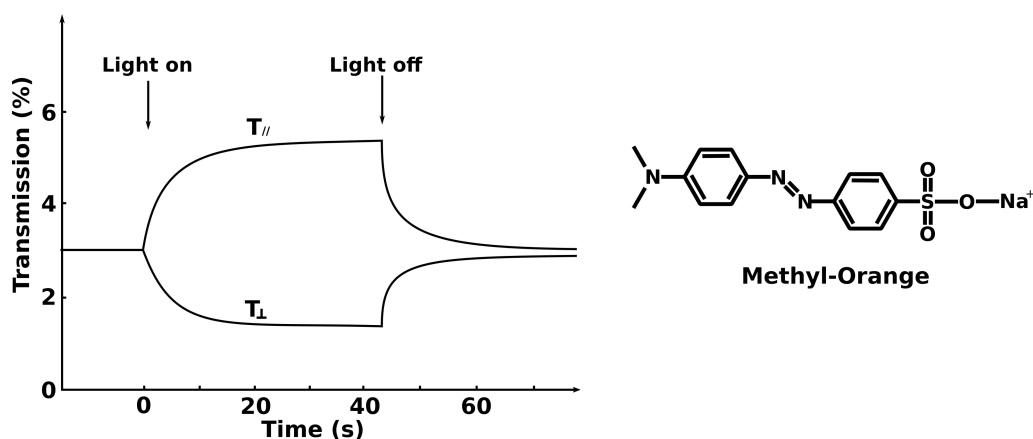


Figure 3.5: Transmission of methyl-orange ($\lambda = 488nm$) as a function of irradiation time parallel (T_{\parallel}) and perpendicular (T_{\perp}) to the pump polarisation is shown, redrawn from [23].

It is this selective excitation process which results in an overall reorientation/optical torque induced to the azobenzene-based molecules, ultimately leading to perpendicular orientation with respect to the excitation polarisation. This reorientation was demonstrated nicely in 1984 by Todorov [23], figure 3.5, in which the absorption due to the *trans* state of methyl-orange in *poly-vinyl alcohol*

3. DYES AND PHOTOISOMERISATION

solution (non-LC) is monitored parallel and perpendicular to the pump polarisation, clearly demonstrating alignment of the mesogens perpendicular to the pump polarisation.

When doped into a LC host this reorientation of azo-based molecules induces an optical torque on the nematic director which can subsequently result in reorientation of the director to be perpendicular to the excitation polarisation [24]. This has been observed in a wide range of experiments [25–27], with the director reorientation fixed during steady-state irradiation and remaining stationary post irradiation if the surface alignment treatment has negligible azimuthal anchoring energy.

LIMR of all kinds can be considered simply as an optical torque acting on the director, in this case the photoisomerisation optical torque applies a force perpendicular to the pump polarisation. Explicit expressions for the optical torque induced are not easy to obtain as they are highly dependent on the conditions involved: director orientations, pump polarisation, anchoring conditions, and dye chemical composition, although modelling of the dynamics can provide insight into this [28, 29]. However, with nematic LCs it can simply be assumed that there is an additional term included with the free energy density such that:

$$F = F_{el} + F_{opt}, \quad (3.9)$$

where F_{el} is the elastic free energy and F_{opt} is the optical free energy. The equilibrium condition given under steady state irradiation is when the sum of elastic torque Υ_{el} and optical torque Υ_{opt} is zero:

$$\Upsilon_{el} + \Upsilon_{opt} = 0. \quad (3.10)$$

3.2.3 Light-induced order modification

The photoisomerisation process from the *trans* to *cis* state shows a distinct change in molecular shape. If the simplest configuration is considered to be a change from rod-like (*trans*) to a bent V-shape (*cis*), it is clear that when in the *trans* conformation the mesogen will pack well with a nematic LC host with very little

disruption. However, the *cis* state isomer will not pack well with a nematic host and will lower the order of its neighbouring molecules, see figure 3.6.

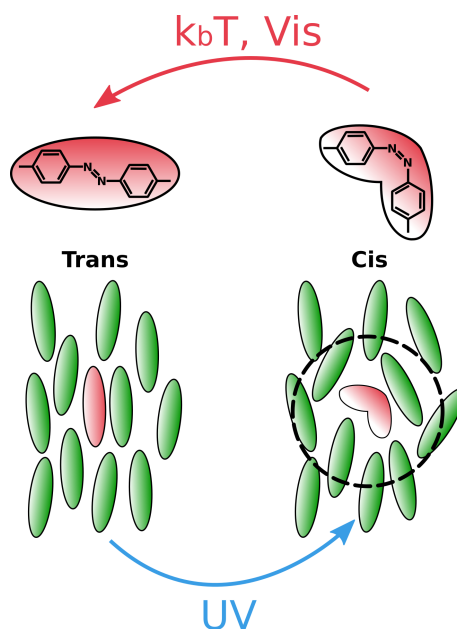


Figure 3.6: The photoisomerisation of an azo-based mesogen from *trans* to *cis*. The molecule goes from a well packed nematic rod-shape, to a bent molecule that disrupts the ordering of the nematic host.

The large optical non-linearities observed in 1980 [18, 19] were first linked to this change in orientational order due to conformational shape change by Odulov [30]. Odulov demonstrated that the change in macroscopic order due to the conformational transition of MBBA, figure 3.7, was the reason such large optical non-linearities were observed.

The conformational change from *trans* to *cis* can be considered as the process of introducing impurities into the system. These impurities (*cis* molecules) are known as light-induced impurities (LIMs) and will impact the material's polarisability and molecular interaction energy. In describing the effect of LIMs on a nematic system a number of assumptions must be made including [31]:

3. DYES AND PHOTOISOMERISATION

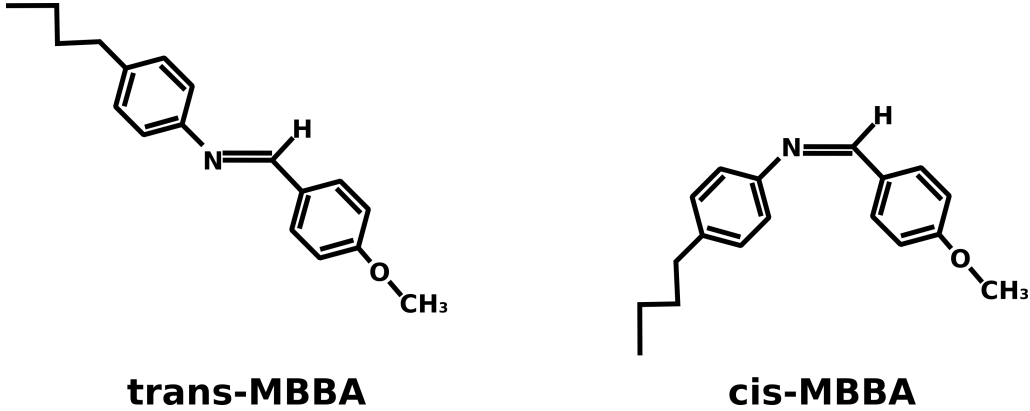


Figure 3.7: The conformational *trans* and *cis* states of LC MBBA used in experiments on optically induced nonlinearities [18, 30].

1. Photoisomerisation is reversible.
2. Phototransformation makes no change to the molecular integrity.
3. Neighbouring LIMs have no overlap.
4. The nematic LC has an equilibrium distribution.
5. The concentration of molecules in the "excited state" is zero. This condition is met if the excited state lifetime is sufficiently short.
6. The symmetry of the nematic state does not change due to the LIMs.

The appearance of LIMs in a nematic LC will result in a shift in the transition temperature (T_{NI}) by $\Delta\tau = \tau_0 - \tau$, where $\tau = \frac{T}{T_{NI}}$ and the sub/super-script "0" corresponds to zero concentration of LIMs. Therefore, the change in refractive index (δn) due to the shift in transition temperature (order parameter) can be given by:

$$\delta n^S = n_0^S(\tau_0 + \Delta\tau) - n^S(\tau_0). \quad (3.11)$$

It is shown by Pinkevich [31] that the change in refractive index caused by the change in polarisability is negligible and therefore any change in the material is dominated by the change in order parameter.

Maier-Saupe theory predicts that the nematic to isotropic phase transition temperature is given by [32]:

$$\begin{aligned}
 T_{NI}^0 &= 0.22 \frac{\Lambda_0}{k_b}, \\
 \Lambda_0 &= \sum_i v_{ij}^0,
 \end{aligned}
 \tag{3.12}$$

where Λ_0 is the intermolecular interaction energy, v_{ij} is the amplitude of intermolecular interaction potential, and k_b is the Boltzmann constant. Now the appearance of LIMs will result in a shift in the phase transition temperature due to their change in intermolecular interaction energy:

$$\begin{aligned}
 T'_{NI} &= 0.22 \frac{\Lambda'}{k_b}, \\
 \Lambda' &= \Lambda_0 + 2c' \sum_i \Delta v_{ij}, \\
 c' &= \frac{N'}{N_0}, \\
 \Delta v_{ij} &= v'_{ij} - v_{ij},
 \end{aligned}
 \tag{3.13}$$

where T'_{NI} is the modified transition temperature, Λ' is the modified intermolecular interaction energy, c' is percentage volume concentration of LIMs (N') with respect to the volume concentration of all molecules (N_0), and Δv_{ij} is the change in intermolecular interaction potential. Combining the equations for T_{NI} and T'_{NI} the following relationship can be found:

$$\frac{\Delta T_{NI}}{T_{NI}^0} = \frac{\Lambda' - \Lambda_0}{\Lambda_0} = 2c' \frac{\sum_j \Delta v_{ij}}{\sum_j v_{ij}^0}.
 \tag{3.14}$$

The ratio of the change in transition temperature ($\Delta T_{NI} = T' - T_{NI}^0$) to the un-irradiated transition temperature is directly related to the LIM concentration multiplied by the relative change in the intermolecular interaction potential.

As the main contributor to any changes in the material is assumed to be due to the shift in order parameter this means that with the measured difference in transition temperature, equation 3.11, can be simplified to:

3. DYES AND PHOTOISOMERISATION

$$\delta n^S = n_0(\tau_0 + \Delta\tau) - n_0(\tau), \quad (3.15)$$

where $n^S(\tau)$ has been replaced with $n_0(\tau)$.

3.3 Summary

In this chapter the two common dichroic dye types, azobenzene and anthraquinone, were shown and their relative advantages and disadvantages in LC systems were discussed. The guest-host phenomenon was introduced, demonstrating how a dichroic dye doped into a nematic LC host will align itself with its long-axis oriented in the same direction as the director. The relationship between the polarisation angle dependent absorption and the LC bulk order parameter was established, with equation 3.8 utilised later in chapter 7 → 9.

The photoisomerisation of azobenzene-based dyes was introduced and the two main light-induced modifications of nematic LCs was discussed: LIMR and LIOM. The polarisation angle-dependent excitation process is shown to generate a reorientation of the azo-dye to be perpendicular to the excitation polarisation. When doped into a nematic LC this can subsequently induce a torque on the director field causing overall director reorientation (LIMR). The conformational shape change in the photoisomerisation process is shown to generate modifications in the order parameter of the nematic host (LIOM). The theory surrounding these were explored, with previous literature assuming this change in order is the main contributor to any physical parameter modifications in the irradiated sample [31]. This assumption will be explored in this thesis and equation 3.14 will also be utilised in experimental data analysis (chapter 7).

References

- [1] M. T. Sims, L. C. Abbott, S. J. Cowling, J. W. Goodby, and J. N. Moore. Molecular Design Parameters of Anthraquinone Dyes for Guest-Host Liquid-Crystal Applications: Experimental and Computational Studies of Spectroscopy, Structure, and Stability. *Journal of Physical Chemistry*, 120:11151–11162, 2016. [xvi](#), [22](#), [26](#)
- [2] G. H. Heilmeyer and L. A. Zanoni. Guest-host interactions in nematic liquid crystals. A new electro-optic effect. *Applied Physics Letters*, 13(3):91–92, 1968. [22](#)
- [3] D. L. White and G. N. Taylor. New absorptive mode reflective liquid-crystal display device. *Journal of Applied Physics*, 45:4718–4723, 1974. [22](#)
- [4] M. T. Sims. Dyes as guests in ordered systems: current understanding and future directions. *Liquid Crystals*, 43(13-15):2363–2374, 2016. [22](#), [23](#)
- [5] B. Bahadur. *Liquid crystals applications and uses Vol. 3*. World Scientific, 1992. [23](#)
- [6] J. W. Goodby, P. J. Collings, T. Kato, C. Tschierske, H. F. Gleeson, and P. Raynes. *Handbook of Liquid Crystals Volume 8: Applications of Liquid Crystals*. Wiley-VCH, 2014. [23](#)
- [7] L. Palsson, M. Szablewski, A. Roberts, A. Masutani, G. D. Love, G. H. Cross, and D. Bloor. Orientation and solvatochromism of dyes in liquid crystals. *Molecular Crystals and Liquid Crystals*, 402:43–53, 2003. [23](#)
- [8] M. Gurulk, H. A. Abdulkadir, M. S. Akkus, F. Akkurt, and A. Alicilar. Comparison of guest-host liquid crystal systems doped with azo or anthraquinone dyes. *Iranian Journal of Science and Technology Transactions A: Science*, 41:1–5, 2017. [23](#), [24](#)
- [9] R. Christie. *Colour Chemistry*. RSC, 2001. [23](#)

REFERENCES

- [10] K. Naito and H. Iwanaga. Relation between molecular structure of dichroic dyes and their solubility in fluorinated liquid crystals. *Japanese Journal of Applied Physics*, 37:3422–3427, 1998. [24](#)
- [11] T. Uchida and M. Wada. Guest-host type liquid crystal displays. *Molecular Crystals and Liquid Crystals*, 63:19–44, 1981. [24](#)
- [12] K. J. Rothschild and N. A. Clark. Polarized infrared spectroscopy of oriented purple membrane. *Biophysical Journal*, 25:473–487, 1979. [25](#)
- [13] M. van Gorp. The use of rotation matrices in the mathematical description of molecular orientations in polymers. *Colloid and Polymer Science*, 273:607–625, 1995. [26](#)
- [14] E. D. Cehelnik, R. B. Cundall, C. J. Timmons, and R. M. Bowley. Spectroscopic studies of trans-1,6-diphenyl-1,3,5-hexatriene in ordered liquid crystal solutions. *Proceedings of the Royal Society of London. Series A, Mathematical and Physical Sciences*, 335(1602):387–405, 1973.
- [15] D. Bauman and E. Wolarz. Application of optical spectroscopy methods to determine orientational order in uniaxial liquid crystal phases of polymers with mesogenic side groups. *Optical Engineering*, 34(12):3412–3417, 1995. [26](#)
- [16] M. T. Sims, L. C. Abbott, S. J. Cowling, J. W. Goodby, and J. N. Moore. Principal molecular axis and transition dipole moment orientations in liquid crystal systems: an assessment based on studies of guest anthraquinone dyes in a nematic host. *Physical Chemistry Chemical Physics*, 19:813–827, 2017. [26](#)
- [17] N. J. Turro, V. Ramamurthy, and J. C. Scaiano. *Modern Molecular Photochemistry of Organic Molecules*. University Science Books, 2010. [27](#)
- [18] B. Y. Zeldovich, N. F. Pilipetskii, A. V. Sukhov, and N. V. Tabiryan. . *Journal of Experimental and Theoretical Physics Letters*, 31:263–269, 1980. [xvii](#), [28](#), [31](#), [32](#)

-
- [19] A. S. Zolotko, V. F. Kitaeva, N. Kroo, N. N. Sobolev, and L. Chillage. . *Journal of Experimental and Theoretical Physics Letters*, 32:158–162, 1980. 28, 31
- [20] I. C. Khoo and S. L. Zhuang. Nonlinear optical amplification in a nematic liquid crystal above the Frederiks transition. *Applied Physics Letters*, 37(3):3–4, 1980. 28
- [21] F. Simoni and O. Francescangeli. Effect of light on molecular orientation of liquid crystals. *Journal of Physics: Condensed Matter*, 11:R439–R487, 1999. 28
- [22] I. C. Khoo, S. Slussarenko, B. D. Guenther, M-Y. Shih, P. Chen, and W. V. Wood. Optically induced space-charge fields, dc voltage, and extraordinarily large nonlinearity in dye-doped nematic liquid crystals. *Optics Letters*, 23(4):253–255, 1998. 28
- [23] T. Todorov, L. Nikolova, and N. Tomova. Polarization holography. 1: A new high-efficiency organic material with reversible photoinduced birefringence. *Applied Optics*, 23(23):4309–4312, 1984. xvi, 29
- [24] L. M. Blinov. Photoinduced molecular reorientation in polymers, langmuir-blodgett films and liquid crystals. *Journal of Nonlinear Optical Physics and Materials*, 5(2):165–187, 1996. 30
- [25] S-T. Sun, W. M. Gibbon, and P. J. Shannon. Alignment of guest-host liquid crystals with polarized laser light. *Liquid Crystals*, 12(5):869–874, 1992. 30
- [26] I. Janossy and T. Kosa. Influence of anthraquinone dyes on optical reorientation of nematic liquid crystals. *Optics Letters*, 17(17):1183–1185, 1992.
- [27] F. Simoni and O. Francescangeli. Dye-doped liquid crystals as high-resolution recording media. *Optics Letters*, 22(8):549–551, 1997. 30
- [28] D. Statman and J. C. Lombardi Sr. Modeling the dynamics of photo-induced reorientation of nematic liquid crystals doped with azo-dye. *Molecular Crystals and Liquid Crystals*, 494:1–10, 2008. 30

REFERENCES

- [29] A. D. Kiselev, V. G. Chigrinov, S. V. Pasechnik, and A. V. Dubstov. Photoinduced reordering in thin azo-dye films and light-induced reorientation dynamics of the nematic liquid-crystal easy axis. *Physical Review E*, 86:011706, 2012. [30](#)
- [30] A. G. Odulov, Y. A. Reznikov, M. S. Soskin, and A. I. Khizhnyak. Photostimulated change of phase-transition temperature and "giant" optical nonlinearity of liquid crystals. *Soviet Physics Journal of Experimental and Theoretical Physics*, 58(6):1154–1158, 1983. [xvii](#), [31](#), [32](#)
- [31] I. P. Pinkevich, Y. A. Reznikov, V. Y. Reshetnyak, and O. V. Yaroshchuk. Conformational optical nonlinearity of nematic liquid crystals. *International Journal of Nonlinear Optical Physics*, 1(3):447–472, 1992. [31](#), [32](#), [34](#)
- [32] V. W. Maier and A. Saupe. Eine einfache molekulare Theorie des nematischen kristallinflüssigen Zustandes. *Zeitschrift für Naturforschung*, 13(a):564–566, 1958. [33](#)

Chapter 4

Experimental methods and materials

This chapter will introduce the materials utilised throughout this thesis and will also describe some of the general experimental methods used in the investigation of the underlying properties of these materials. Experimental procedures specific to an investigation will be described in further detail in the respective chapters.

4.1 Materials

This thesis will focus mainly on the combination of light-sensitive materials with the nematic liquid crystal (LC) phase. There are three main materials utilised which will each be introduced here in turn, whilst other materials less frequently used will be introduced in the respective chapters.

4-Cyano-4'-pentylbiphenyl (5CB), figure 4.1, was the first stable room temperature nematic LC developed by Gray in 1973 [1]. This ubiquitous nematic LC was the first stable LC to exhibit a room temperature nematic phase ($25 \rightarrow 35^\circ\text{C}$) making it applicable to LC technologies. It has subsequently been studied extensively by the LC research community and there is a swath of literature available describing this material. It is therefore an excellent nematic LC to utilise in combination with interesting dopant's or mechanisms due to the amount of literature

4. EXPERIMENTAL METHODS AND MATERIALS

available for comparison.

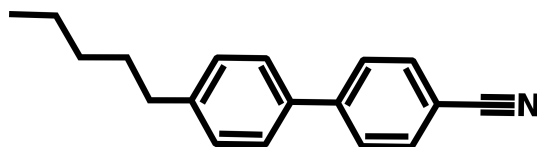


Figure 4.1: The chemical structure of 5CB is shown. The crystal to nematic phase transition temperature is 25.0°C and the nematic to isotropic phase transition temperature is 36.3°C .

4-2-butyl-4'-2-alkoxyazobenzene (BAAB2), figure 4.2, is a LC material with an azobenzene linkage group. It is part of a series synthesised by V. A. Grozhik [2]. The BAAB- series has been characterised in terms of its light induced switching properties [3, 4], potential use as a drug delivery system [5], and their effect on cholesteric LCs [6]. BAAB2 exhibits two conformational states, *trans* and *cis*, depicted in figure 4.2 and this material is discussed in detail in chapters 7 → 9.

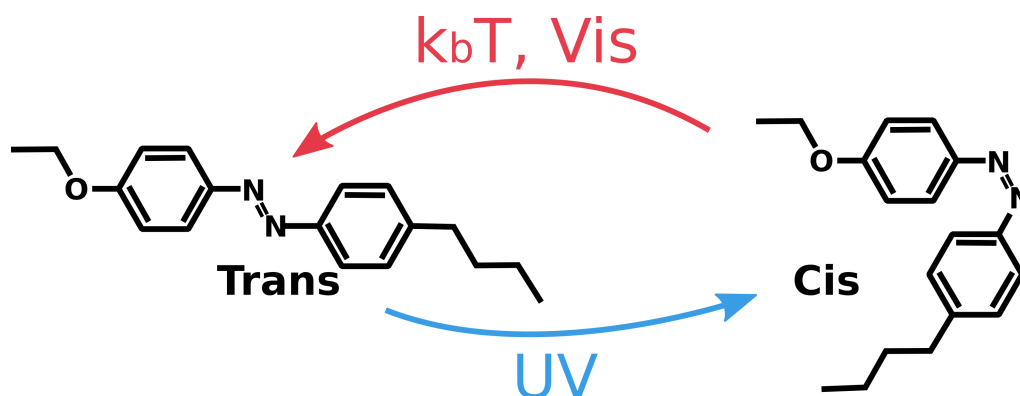


Figure 4.2: The chemical structure of BAAB2 is shown. The crystal to nematic phase transition temperature is 48.5°C and the nematic to isotropic phase transition temperature is 83.5°C .

1,5-Dihydroxy-4,8-bis-(4-propylphenylamino)anthraquinone (15NB3OH), figure 4.3, is part of a set of anthraquinone dyes synthesised by Cowling [7]. 15NB3OH

is an anthraquinone based dichroic dye that exhibits polarisation angle dependent absorption which peaks at $\lambda = 694nm$. It has been investigated extensively by researchers at the University of York [8–10], and other anthraquinone dyes from this synthesis set have been utilised in LC switchable optics [11]. The coupling of the dichroic dye’s polarisation angle dependent absorption to the order parameter of the nematic system is utilised in later chapters as a simple optical measurement of the order parameter of the host LC.

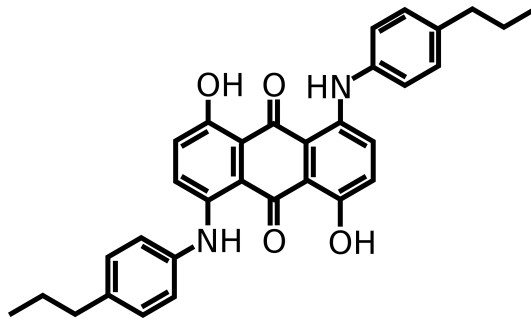


Figure 4.3: The chemical structure of 15NB3OH is shown. The absorption peaks at $\lambda = 694nm$ and the angle the TDM makes with the molecular long axis is $\beta = 15.9^\circ$ [8].

4.2 Polarised optical microscopy

In LC characterisation the key experimental procedure in the identification of phases, optical properties, and phase transition temperatures is observation of the LC sample using polarised optical microscopy (POM). The general POM observation of a birefringent sample is depicted in figure 4.4(a) and involves the illumination of the birefringent sample held between crossed polarisers (polarisation axis of each polariser at 90° with respect to one another).

An isotropic sample will appear dark when observed using POM as the polarised light remains unaffected by the isotropic medium and is therefore blocked by the analyser. However, if a birefringent sample is observed using POM (such

4. EXPERIMENTAL METHODS AND MATERIALS

as LCs), with the optic axis at any arbitrary angle away from the polariser axis, then a bright/coloured state is observed. Orientation of the optic axis at an angle to the polarisation will result in the light's electric field decomposing into two modes, corresponding to each refractive index of the birefringent medium. These modes then propagate at different speeds (due to the birefringence) and upon recombination a wavelength-dependent phase difference is induced to the light and therefore results in wavelength-dependent transmission through the analyser.

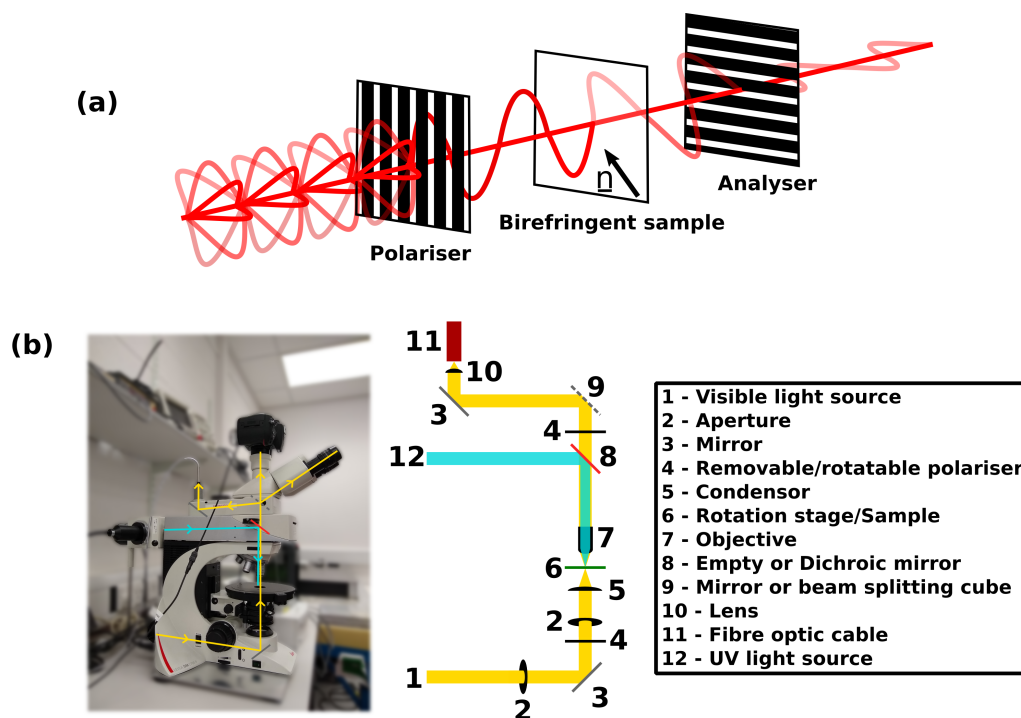


Figure 4.4: (a) Unpolarised light is polarised by a polariser, upon passing through a birefringent medium a retardance is applied. Although this will typically generate elliptically polarised light here it is simply depicted as a rotation in the polarisation. Partial transmission of light is then achieved through the analyser due to the modification to the polarised light. (b) The Leica DM2700 polarising microscope used in the majority of experiments is shown. The entire system is depicted in terms of optical path and microscope parts.

The wavelength-dependent transmission in POM with crossed polarisers and optic axis at 45° to the polarisers is given by equation 4.1. When an aligned polariser setup is utilised (polarisation axes aligned) the \sin^2 function is replaced with a \cos^2 function, utilised in chapter 5. A wavelength dependent transmission is achieved in both states which results in a typically coloured appearance when LCs are observed using POM, the transmission spectrum between crossed polarisers can be measured using a coupled spectrometer as shown in figure 4.4(b).

$$T = \sin^2\left(\frac{\pi d \Delta n}{\lambda}\right), \quad (4.1)$$

where d is the cell gap, Δn is the effective birefringence, and λ is the wavelength.

In this thesis POM is modified in a number of ways to allow for different experiments to be conducted. Figure 4.4(b) shows the Leica DM2700 polarising microscope utilised for the majority of investigations.

UV/Vis Spectrometer

One such modification involves the direct measurement of the visible transmission spectrum via coupling of the UV/Vis Avantes AvaSpec-2048 XL spectrometer (sensitivity of $\pm 1nm$) via optical coupling of an Avantes FC-UV050-2 200 \rightarrow 800nm optical fibre into position 11. The measured spectrum is post-analyser and allows the crossed, uncrossed, or single polariser transmission of light through the sample to be accurately measured. The visible light source produces light of wavelengths 400 \rightarrow 740nm, with varying intensity typical of a broadband light source. The polarisers utilised have an extinction ratio of 1000:1 measured via the spectrometer (transmitted light through crossed polarisers is approximately 0.1%). During experimentation utilising spectrometer measurements a mirror is employed in position 9 of figure 4.4(b) to remove the polarisation dependent transmission generated from the beam-splitting cube.

The normalisation procedure is key in spectrometer measurements if accurate values for the optical properties of a sample or device is to be attained. Additional

4. EXPERIMENTAL METHODS AND MATERIALS

error can be introduced into the measurement if, for example, different alignment substrates are utilised between the measurement and normalisation measurement.

In chapter 5 and 10 the normalisation procedure for spectrometer measurements simply involves removing the losses generated from the polarisers and experimental losses (approximately 55% for unpolarised light) and therefore involves setting the bright state as an empty hot stage with aligned polarisers. This is done to allow for accurate representation of the **device** capabilities.

In chapter 6 → 9 the majority of experimentation involving dye-doped samples the transmission/absorption spectrum of a dye-doped sample held in a LC device is normalised to an effectively identical device, with identical ITO/alignment layers and a cell gap within $\pm 1\mu m$, filled with the non-dye doped sample. This removes any optical losses generated by the LC host and device substrates, as well as experimental losses such as hot stage reflections, to give an accurate representation of the **dyes** optical properties and ensure that no additional error is introduced into the experiment by varying alignment/ITO substrates between measurements. During all normalisation procedures it is also crucial that the temperature is consistent between all measurements and that the director is oriented in an identical manner with respect to the polariser ($\pm 1^\circ$). The impact of this variation in director angle on the result can be considered simply through calculating the effective change in the refractive index. If the refractive indices of 5CB are considered ($n_e = 1.730$ and $n_o = 1.53$) a variation of 1° away from the director will result in a shift in refractive index from $n_e = 1.730$ to $n_x = 1.729$, a very small shift introducing minimal error to the measurement. These steps are crucial as any change in the refractive index will change the reflections at the glass/ITO/alignment - LC interface. Following these normalisation procedures results in accurate representation of the optical properties of the samples or devices, however multiple runs must always be conducted to ensure confidence in results.

Single polarising microscopy

Measurements of dichroic dye polarisation angle-dependant absorption is achieved in a single polariser microscopy setup coupled to the spectrometer. During these measurements the bottom polariser of figure 4.4(b) is removed, whilst the optic axis of the sample under consideration is oriented at 0 or 90° to the analyser (upper polariser).

UV Irradiation

UV irradiation is key in measurements surrounding photo-sensitive materials and coupling is achieved in this setup via the reflection arm. A Leica external UV light source EL 6000 is coupled via a liquid light guide into the reflection arm of the setup shown in figure 4.4(b), which produces unpolarised light of wavelengths 360 → 680nm. A dichroic mirror is utilised in position 8 which reflects light of wavelengths < 400nm to the sample, whilst transmitting wavelengths > 400nm. This means that only UV light from the external UV light source impacts the system, whilst still allowing optical measurements via visible light from the transmission mode to pass through the dichroic mirror to the spectrometer.

The soda-lime glass utilised in LC device construction has an associated absorption spectrum which increases in the UV regime. The transmission of ITO coated soda-lime glass is still greater than 50% at wavelengths greater than $\lambda = 330nm$ [12] and therefore the glass absorption will not greatly impact the UV irradiation experiments as wavelengths between 360 and 400nm are utilised. The UV wavelengths used during these experiments are in the high wavelength UV regime and as such are not greatly impacted by glass absorption properties of the devices or microscope parts. Ensuring consistency between all measurements, in the optics employed and device substrates used, allows for comparisons between results to be made, with strong certainty that the UV intensity impacting the sample is constant between runs.

4. EXPERIMENTAL METHODS AND MATERIALS

Temperature control

In all POM measurements a Linkam LTSE120 hotstage was used with a Linkam T95-PE temperature controller to maintain the sample temperature during experimentation. This was used with active water cooling from a cold water bath flowing through the system allowing active cooling and sub-room temperature measurements to be conducted. The hotstage measures to an accuracy of $\pm 0.1^\circ\text{C}$ and all measurements are compared as a function of reduced temperature to reduce the error in the calibration of different temperature control experimental methods.

4.3 Differential scanning calorimetry

Differential scanning calorimetry (DSC) [13] is a method utilised in this thesis to identify first-order phase transitions in LC samples. The technique involves the measurement of the difference in heat flow ($\frac{dQ}{dt}$), on heating or cooling, between a sample and a well characterised reference material (in this case indium). The sample is held in a hermetically sealed aluminium pan and an example DSC trace (heating and cooling cycle) for nematic LC 5CB measured using the TA Instruments Q20 DSC is demonstrated in figure 4.5.

Upon heating the sample the heat flow is negative as expected it requires energy in order to increase the temperature. Two minima in heat flow are observed on heating relating to first-order phase transitions, the first of which is the melting of the crystal phase into the nematic phase which is a large endothermic reaction and therefore requires a higher heat flow compared to the reference pan to increase the temperature of the sample. The second trough in heat flow corresponds to the nematic to isotropic transition, with a much smaller enthalpy change generated during this transition and therefore a smaller change in heat flow is observed. Upon cooling the heat flow is positive, energy is not required in order to actively cool the sample. A single peak is observed on cooling corresponding to the isotropic to nematic transition, an exothermic first order

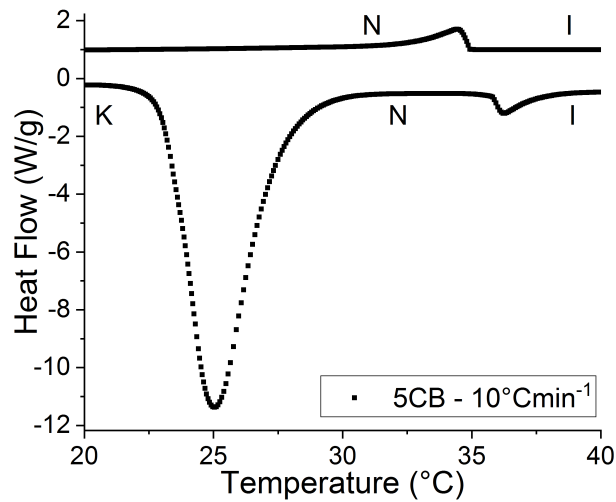


Figure 4.5: The DSC heat flow trace for typical LC material 5CB, with a heating rate of $10^{\circ}\text{Cmin}^{-1}$. On heating the enthalpy change associated with the crystal (K) to nematic (N) phase and the nematic to isotropic (I) phase transition is observed. On cooling the enthalpy change associated with the isotropic to nematic phase transition is observed, however the nematic to crystal phase transition isn't observed in the demonstrated temperature range as a result of the sample super cooling.

transition which therefore results in a peak in heat flow. The nematic to crystal transition is not observed in the temperature range demonstrated of the DSC trace due to supercooling of the sample.

DSC is utilised in this thesis to identify the first-order phase transition temperatures of LC materials identified by the peak positions in the transitions. Whilst identification of the peak in the enthalpy change is possible to an accuracy of $\pm 0.05^{\circ}\text{C}$ the position at which it appears is dependent on the sample mass and the heating/cooling rate employed. By keeping the heating/cooling rate constant between all measurements, at $10^{\circ}\text{Cmin}^{-1}$, the DSC transition temperatures are then quoted to an accuracy of $\pm 0.1^{\circ}\text{C}$ throughout this thesis. However, comparison between different experimental procedures, such as hot stage transition

4. EXPERIMENTAL METHODS AND MATERIALS

temperature measurement and DSC, has a higher associated error due to differences in temperature calibration, thermal contact, and heat rates. Therefore, in comparing experimental procedures the transition temperatures are typically within $\pm 1^\circ C$ of each other.

4.4 Dielectrics

The theory discussed in chapter 2.6 describes how the director deformation under an applied voltage can be directly related to physical parameters of the LC material including elastic constants and dielectric permittivity. This is generated by fitting of theoretical equations to the voltage dependence of permittivity of the LC material.

The permittivity dependence on voltage is achieved by measuring how the capacitance of a LC sample varies as a function of voltage in a LC cell. The cell is constructed with overlapping ITO electrodes on each surface, with the ITO etched to give a central region of applied electric field such that only the LC material is measured (away from the glue seals). In the experiments conducted in Chapter 6.1 the LC cell had etched ITO layers in a guard ring design. This pattern involves a third electrode, held at ground, circling the central electrode with a small spacing between them, which results in displacement of the fringing of the electric field away from the area of study and therefore reduces the error associated with the capacitance measurement [14]. However, the experiments conducted in Chapter 8 were not conducted using this guard-ring design, increasing the error slightly in the measurement, however this error is still small when compared to error introduced from other parameters (e.g. fitting).

The capacitance is measured using an Agilent E4980A Precision LCR Meter for varying voltages $0 \rightarrow 20V_{rms}$ in steps of $0.05V_{rms}$. A frequency of 10kHz is used to prevent ion build up on the electrodes, whilst also avoiding any significant relaxations in the LC material. The temperature of the system is controlled using

an active water cooling Linkham LTSE120 hotstage coupled to a Linkham T95-PE temperature controller. The empty cell capacitance (C_0) was first measured in the device without LC material which is given as:

$$C_0 = \frac{\epsilon_0 A}{d} + C_s, \quad (4.2)$$

where ϵ_0 is the permittivity of free space, A is the electrode area, d is the cell gap, and C_s is the stray capacitance. The capacitance of the device filled with LC material (C_{LC}) can then be measured which is given as:

$$C_{LC} = \frac{\epsilon_{LC} \epsilon_0 A}{d} + C_s, \quad (4.3)$$

where ϵ_{LC} is the measured material permittivity. Equation 4.3 can then be subtracted from equation 4.2 to give:

$$C_{LC} - C_0 = \frac{\epsilon_0 A}{d} (\epsilon_{LC} - 1) \quad (4.4)$$

$$\epsilon_{LC} = \frac{d}{\epsilon_0 A} (C_{LC} - C_0) + 1 \quad (4.5)$$

This is the relationship used to relate the measured capacitance to the permittivity measured in the LC devices. This can then be fit with the theoretical description in chapter 2.6, utilising software developed internally by P. Brimicombe which follows the method developed by Welford and Sambles [15] to give physical parameters of the LC material, as shown in figure 4.6(a). If pre-tilt is not included in the fitting procedure a poor fit around the threshold voltage is attained as seen in figure 4.6(b), which in turn results in poor calculations of the splay and bend elastic constant, as well as the perpendicular dielectric permittivity.

In comparing the results of dielectric fittings of different mixtures, devices, and experimental conditions the standard error propagation quickly loses accuracy in fully representing the error associated with the measurement. By comparing the 5CB physical parameters with accepted literature values [16], figure 4.7, it can be seen that the parameters maximum variation away from the accepted values is approximately 5% (both datasets did not use guard rings). Therefore, in quoting physical parameters attained from dielectric fitting the values will be quoted with

4. EXPERIMENTAL METHODS AND MATERIALS

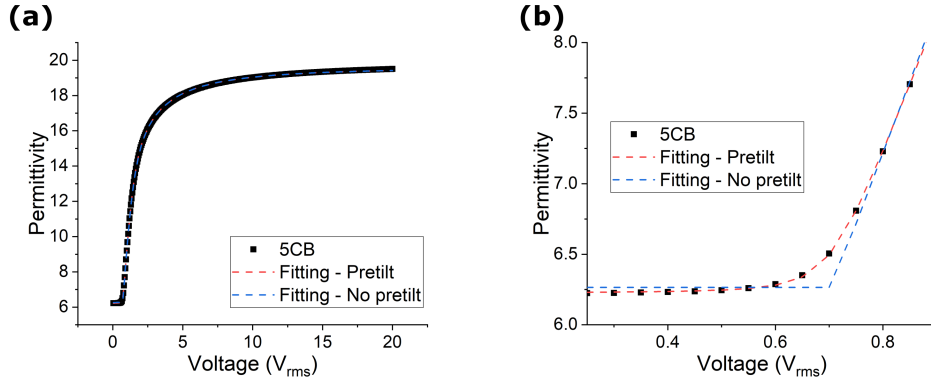


Figure 4.6: (a) The voltage dependence of capacitance is shown for 5CB sample at 20°C. The dielectrics fitting with pre-tilt gave parameters of $k_{11} = 6.8pN$, $k_{33} = 10.5pN$, $\epsilon_{||} = 20.0$, $\epsilon_{\perp} = 6.2$, and $\theta_{tilt} = 1.5^{\circ}$. The dielectrics fitting without pre-tilt gave parameters of $k_{11} = 6.1pN$, $k_{33} = 10.9pN$, $\epsilon_{||} = 20.0$, and $\epsilon_{\perp} = 6.3$. (b) A clear demonstration of the difference in fitting when pre-tilt is included into the fitting procedure.

a 5% error to accurately represent the errors which will not be accounted for in standard error propagation (e.g. variation between devices alignment, cell gap variation, wire length...).

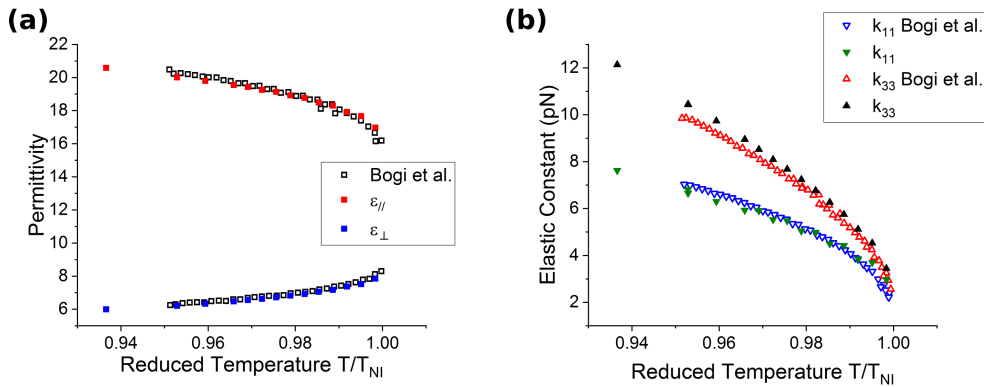


Figure 4.7: The comparison of dielectric fitting results for 5CB (a) dielectric permittivity and (b) elastic constants with accepted literature values [16].

4.5 LC devices

LC materials are typically observed using POM and other experimental methods whilst the material is constrained in a device or cell. The cell constrains the LC material between two substrates (typically glass) with a pre-defined thickness or cell gap (usually between 2 and $50\mu\text{m}$). The glass substrates can be coated with an indium-tin-oxide (ITO) layer (quoted resistivity $100\Omega/\square$) which allows the application of an electric field perpendicular to the substrates (utilised in dielectrics measurements). During optical characterisation of materials the measurements were typically conducted using non-ITO coated devices to remove the additional interaction of light with the ITO layer discussed in detail in [17].

The surface of each glass substrate (or on top of the ITO layer) can be treated with an alignment layer (around $0.1\mu\text{m}$ thickness) to generate a preferred director orientation and devices can be constructed in specific ways to generate a desired director profile. In this thesis the majority of experimentation was carried out on a planar aligned device with the director lying homogeneously in the substrate plane. However, for clarity in later discussions the common alignment types and director profiles will be described here.

4.5.1 Device types

The planar aligned LC device, depicted in figure 4.8(a), has substrates typically treated with rubbed polymer, in the case here, either $0.5\%(\frac{w}{w})$ *poly-vinyl-alcohol* (PVA) in de-ionised water or polyimide alignment SE3510 or SE130. Both of these alignment materials are rubbed with felt to generate unidirectional alignment in the substrate plane. Polyimide alignment layers provide better temperature stability compared with PVA and also generate a variety of pre-tilt angles (the angle the director makes out of the plane at the substrate) with SE3510 and SE130 giving pre-tilt angles of $6-8^\circ$ and $1-2^\circ$ respectively.

Planar devices are typically constructed with each substrate rubbing direction oriented away from each other (anti-parallel), figure 4.8(a), to prevent the formation of chevrons in a nematic LC which is observed in devices with substrates

4. EXPERIMENTAL METHODS AND MATERIALS

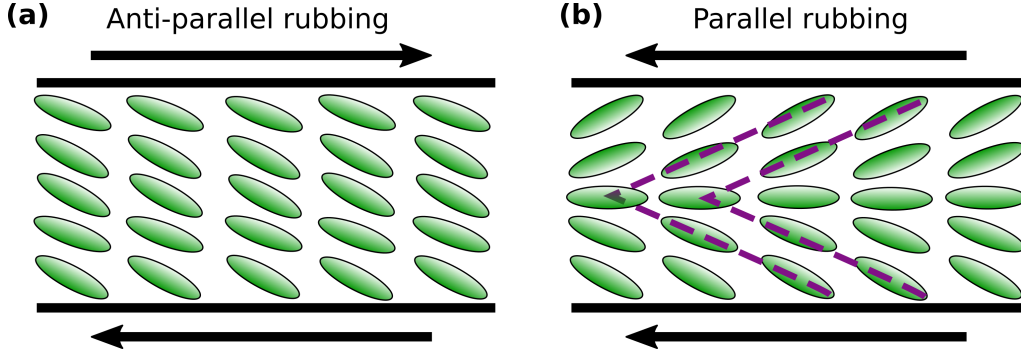


Figure 4.8: (a) The standard planar aligned LC device is depicted. The substrates are rubbed in the anti-parallel fashion and a uniform director orientation is observed. (b) A planar aligned device with parallel rubbing directions is shown. Unidirectional alignment is achieved, however the parallel rubbing results in the formation of chevrons affecting the director field.

rubbed in the same direction (parallel), depicted in figure 4.8(b).

Homeotropic LC devices have substrates treated such that the director orients out of the substrate plane. This can be achieved with either with $0.5\% \frac{w}{w}$ *cetyl trimethyl ammonium bromide* (CTAB) in de-ionised water or through SE1211 polyimide treatment. In the homeotropic case the alignment layer does not require rubbing for unidirectional alignment and is depicted in figure 4.9(a). However, should a negative dielectric material be utilised for a switchable LC device that re-orient from homeotropic towards planar orientation under the application of an electric field, then rubbing of the homeotropic alignment layer can be utilised to ensure a well aligned material when the field is applied, demonstrated in figure 4.9(b, d). Without rubbing of the homeotropic layer the director will re-orient in any in-plane direction under an applied field. However, with rubbing the generation of a preferential re-orientation direction is generated and results in a uniform director distribution under an applied field.

A hybrid-aligned-nematic (HAN) device consists of one homeotropic substrate and one planar substrate, depicted in figure 4.10(a). The director in the HAN

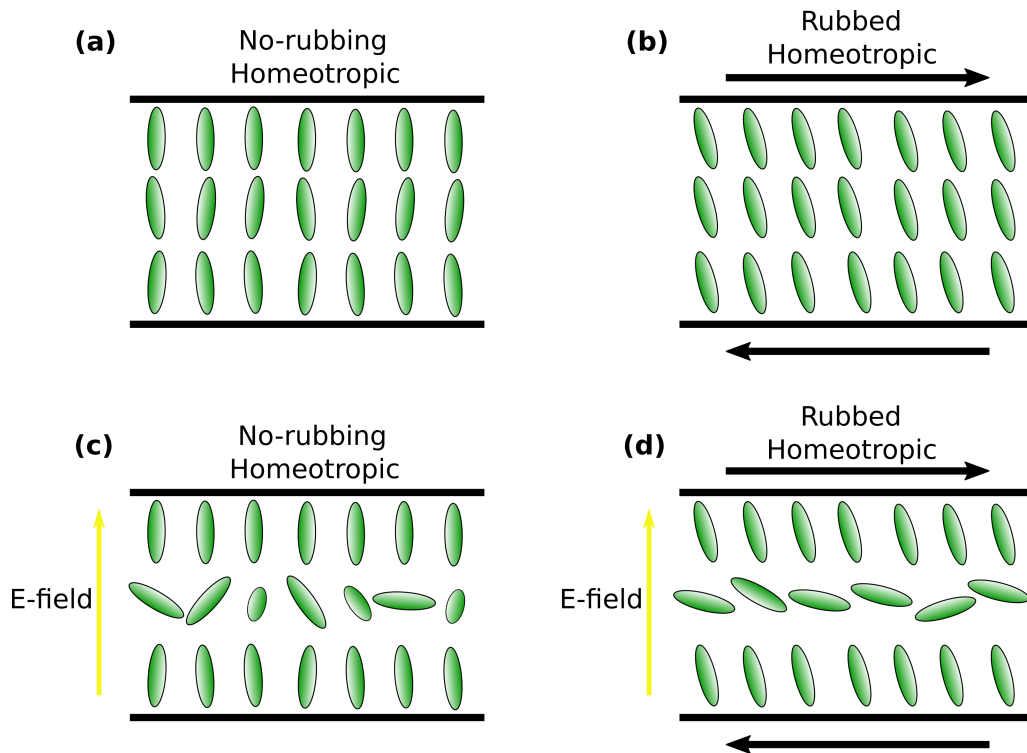


Figure 4.9: (a) The un-rubbed homeotropic device is demonstrated. (b) The rubbed homeotropic device is demonstrated, with the rubbing generating a small, typically less than 1° , pre-tilt preferential direction away from 90° . (c) Application of an electric field to a negative dielectric LC in an un-rubbed homeotropic device is demonstrated, with the random re-orientation demonstrated. (d) Application of an electric field to a negative dielectric LC in a rubbed homeotropic device is demonstrated, with the well aligned re-orientation demonstrated.

device re-orientes between the two substrates and can be used to generate interesting LC devices. A twisted-nematic (TN) device consists of two planar aligned substrates with the rubbing direction oriented at 90° with respect to one another. This is shown in figure 4.10(b), generating a director which re-orientes through the device. When this device type is combined with specific LC materials it can generate wave-guiding of polarised light, rotating the polarisation by 90° , allowing transmission of light between crossed polarisers.

These are some of the basic LC devices utilised in applications and investiga-

4. EXPERIMENTAL METHODS AND MATERIALS

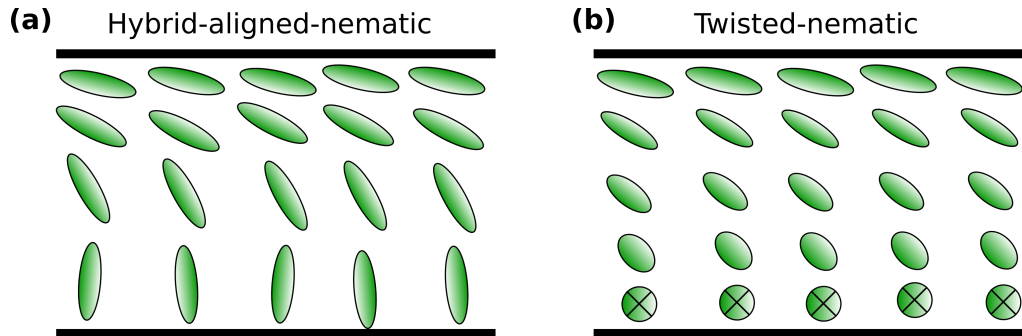


Figure 4.10: (a) The HAN device is shown which consists of a homeotropic treated layer and a planar treated layer. (b) The TN device is shown in which the planar substrates are rubbed at 90° with respect to each other generating a twisted director profile.

tions into LC materials. They are by no means the only possible device orientations or the only alignment materials available, but cover the devices generated during the research period discussed in this thesis.

4.5.2 Device fabrication

The general LC device fabrication procedure will now be outlined to give an overview of the steps involved in generating consistent, well oriented, and uniform cell gap devices.

First, the substrates (15x10mm) are cleaned to remove any dust or organic thin films. The substrate cleanliness is key in achieving a well oriented LC device as any dust particles or debris will generate defects in the director field and disrupt experimental measurements. The cleaning process involves the following steps:

- 30 minutes of sonication in de-ionised water + Decon-90 surfactant to remove dust/debris particles (repeat 2 times).
- 30 minutes of sonication in de-ionised water to remove any surfactant residue (repeat 3 times).
- 30 minutes of sonication in Acetone to remove organic thin-films.

- 30 minutes of sonication in Methanol to remove organic thin-films (also removes drying marks generated by Acetone).
- 10 minutes of irradiation in UV/Ozone to remove any final organic matter on the substrate.

Once the substrates are clean the alignment layer is spin coated onto the substrate with: spin-speed=3000rpm, time=60s, and acceleration=200rpm/s (giving a thickness of approximately $0.1\mu m$). Once spin coated the polyimide treated substrates are baked at $180^{\circ}C$ for 60 minutes to set the alignment layer. The PVA and CTAB alignment is heated at $40^{\circ}C$ for 5 minutes to evaporate any remaining solvent.

Substrates which require rubbing are then rubbed using a felt rubbing machine to give unidirectional alignment, 4 passes under the roller are conducted to give uniform alignment, with the substrate oriented with its long axis in the rubbing direction. Glass spacer beads are then deposited onto one substrates to give the desired cell gap, measured to typically vary by $\pm 0.2\mu m$ across the device. The cells are then constructed with the required alignment orientation and sealed with thermal or UV glue. The glue is set and then the devices are ready for testing. The device thickness is measured to ensure an even cell gap and good alignment of the director in the device is confirmed using POM.

4.5.3 Summary

This section has introduced some of the key materials, experimental methodologies, and LC device fabrication techniques crucial for the research conducted in this thesis. In the next section the research, development, and characterisation of an electrically switchable laser protection filter will be discussed.

References

- [1] G. W. Gray, K. J. Harrison, and J. A. Nash. New family of nematic liquid crystals for displays. *Electronic Letters*, 9(6):130–131, 1973. [39](#)
- [2] P. V. Adomenas and V. A. Grozhik. . *Izv. AN BSSR, Ser. Chem.*, 36:N2, 1977. [40](#)
- [3] V. Grozhik, H. F. Gleeson, S. Serak, S. Watson, and A. Agashkov. Study of optical switching and reorientation in liquid crystals of homologous series of 4-n-butyl-4'-n-alkoxybenzenes. *Molecular Crystals and Liquid Crystals*, 320:433–444, 1998. [40](#)
- [4] U. Hrozhyk, S. Serak, N. Tabiryan, and T. J. Bunning. Wide temperature range azobenzene nematic and smectic LC materials. *Molecular Crystals and Liquid Crystals*, 454:235–245, 2006. [40](#)
- [5] S. J. Watson, H. F. Gleeson, A. D'emanuele, S. Serak, and V. Grozhik. A Study of Photochromic Azobenzene Liquid Crystals as Controlled Release Drug Delivery Systems. *Molecular Crystals and Liquid Crystals*, 331:375–382, 1999. [40](#)
- [6] S. V. Serak, E. O. Arikainen, H. F. Gleeson, V. A. Grozhik, J. P. Guillou, and N. A. Usova. Laser-induced concentric colour domains in a cholesteric liquid crystal mixture containing a nematic azobenzene dopant. *Liquid Crystals*, 29(1):19–26, 2002. [40](#)
- [7] S. J. Cowling, C. Ellis, and J. W. Goodby. Anthraquinone liquid crystal dichroic dyes - a new form of chromonic dye? *Liquid Crystals*, 38(11-12):1683–1698, 2011. [40](#)
- [8] M. T. Sims, L. C. Abbott, S. J. Cowling, J. W. Goodby, and J. N. Moore. Molecular design parameters of anthraquinone dyes for guest-host liquid-crystal applications: Experimental and computational studies of spectroscopy, structure, and stability. *The Journal of Physical Chemistry C*, 120:11151–11162, 2016. [xvii](#), [41](#)

-
- [9] M. T. Sims, L. C. Abbott, S. J. Cowling, J. W. Goodby, and J. N. Moore. Experimental and molecular dynamics studies of anthraquinone dyes in a nematic liquid-crystal host: a rationale for observed alignment trends. *Physical Chemistry Chemical Physics*, 18:20651–20663, 2016.
- [10] M. T. Sims, L. C. Abbott, S. J. Cowling, J. W. Goodby, and J. N. Moore. Principal molecular axis and transition dipole moment orientations in liquid crystal systems: an assessment based on studies of guest anthraquinone dyes in a nematic host. *Physical Chemistry Chemical Physics*, 19:813–827, 2017. [41](#)
- [11] E. I. L. Jull, M. Wahle, P. J. M. Wyatt, C. Ellis, S. J. Cowling, J. W. Goodby, K. Usami, and H. F. Gleeson. Efficiency improvements in a dichroic dye-doped liquid crystal Fresnel lens. *Optics Express*, 27(19):26799–26806, 2019. [41](#)
- [12] M. Baum, J. Strauß, F. Grübel, I. Alexeev, and M. Schmidt. Generation of phase-only holograms by laser ablation of nanoparticulate ITO layers. *Journal of Optics*, 16:125706, 2014. [45](#)
- [13] G. W. H. Hohne, W. F. Hemminger, and H. J. Flammersheim. *Differential Scanning Calorimetry Second Edition*. Springer-Verlag, 2003. [46](#)
- [14] James Hind. *Experimental and theoretical investigations into the switching of liquid crystal devices*. PhD thesis, The Nottingham Trent University, 2007. [48](#)
- [15] K. R. Welford and J. R. Sambles. Analysis of electric field induced deformations in a nematic liquid crystal for any applied field. *Molecular Crystals and Liquid Crystals*, 147(1):25–42, 1987. [49](#)
- [16] A. Bogi and S. Faetti. Elastic, dielectric and optical constants of 4’pentyl-4-cyanobiphenyl. *Liquid Crystals*, 28(5):729–739, 2001. [xviii](#), [49](#), [50](#)
- [17] H. G. Yoon and H. F. Gleeson. Accurate modelling of multilayer chiral nematic devices through the Berreman 4 x 4 matrix methods. *Journal of Physics D: Applied Physics*, 40:3579–3586, 2007. [51](#)

REFERENCES

Chapter 5

Liquid crystal Lyot filter

In this chapter a electrically switchable LC Lyot filter is investigated as a switchable optical filter, specifically for protection against laser damage. High-powered hand-held continuous wave lasers are readily available and are increasingly involved in incidents surrounding camera and eyesight damage or dazzling, malevolent or otherwise. Here this LC device is utilised as a switchable optical filter which prevents damage and dazzling. The capabilities of this device are directly compared to literature for CCD camera damage from a continuous wave laser, as this is fully characterised with threshold damages well established, and demonstrates excellent protection. However, it is difficult to evaluate the ability for this device to protect eyesight as it is obviously less characterised in the literature.

Much of the work contained in this chapter was published by Ethan I. L. Jull and Helen F. Gleeson, "Tuneable and switchable liquid crystal laser protection system", *Applied Optics*, **56**(29), 2017 [1]. Should any of the work included be specific to an author that is not E. I. L. Jull it will be noted in the text.

5.1 Introduction

LC Lyot filters have been previously used as a method of selective wavelength transmission via application of a wavelength-dependent retardance to light propagating between aligned polarisers. The Lyot filter was first developed by Lyot [2], with initial applications focused on astronomical observations [3]. In 1991 Miller

5. LIQUID CRYSTAL LYOT FILTER

included a LC component demonstrating the first LC based Lyot filter [4]. The ease of birefringence modulation through application of an E or B-field to the LC director led to many further developments and applications of controllable LC based Lyot filters including: astronomical observations [5–9], remote sensing [10, 11], laser tuning [12], and biological imaging [13, 14].

Previous Lyot filter applications aimed to generate narrow wavelength transmission window in an attempt to reduce the signal to noise ratio of observations. However, here we utilise the optical properties of a LC Lyot filter to generate the inverse effect - creating a narrow wavelength blocking window to filter damaging laser wavelengths.

There are two previous reports of LC based Lyot filters being implemented in the filtering of laser radiation [15, 16]. Although these designs performed well in their respective applications, they were unable to demonstrate switching between a full transmission mode to a wavelength-dependent rejection mode. The full transmission mode is clearly realised when high voltage application to an LC Lyot filter is considered resulting a close to zero birefringence and therefore clear transmission of light between aligned polarisers. Further, in one case the response time was not quantified [15], and in the other the design was not compact [16].

In this chapter the design and evaluation of a simple, compact, and tuneable LC Lyot filter is fully explored. Demonstration of switching between a full transmission mode and a specific (laser) wavelength rejection mode is shown. The ability to tune to any arbitrary rejection wavelength is achieved via voltage variation in the low-voltage regime. The response time of the device is fully characterised, not only between the OFF to ON states, but also the switching speed between different ON states.

5.2 Liquid crystal Lyot filter

A single-stage LC Lyot filter is comprised of a LC device with the director oriented at 45° to the aligned polariser axes, see figure 5.1.

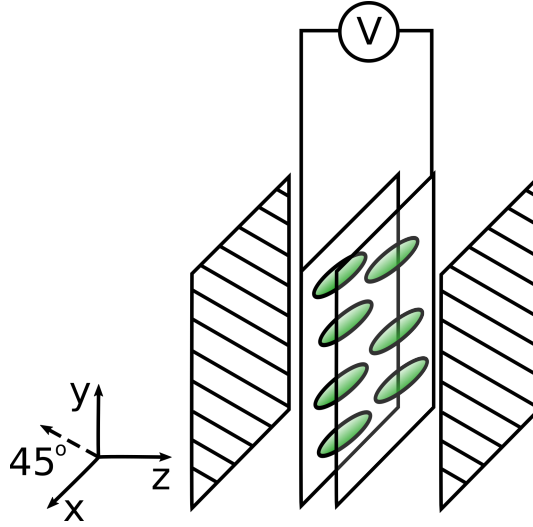


Figure 5.1: LC Lyot filter device schematic. The polariser and analyser are in the xy plane, aligned at 45° to the x and y axis. The LC director is oriented along x axis. Control of the LC birefringence is achieved through application of an E-field.

With the LC director at 45° to the polarisation, a retardance (Γ) is applied to the polarised light transmitting through the birefringent LC sample,

$$\Gamma = \frac{2\pi\Delta n(V)d}{\lambda}, \quad (5.1)$$

where d is the cell gap ($6\mu\text{m}$), $\Delta n(V)$ is the voltage dependent birefringence ($\sim 0.2 \rightarrow 0$), and λ is the wavelength. The transmission through the analyser is then described by equation 5.2 in which polariser and Fresnel losses are neglected ($\sim 55\%$ for unpolarised light). This equation demonstrates that wavelengths of light corresponding to half wave-plate conditions, $\Gamma = 2\pi(m - \frac{1}{2})$ (where m is any integer), will be rejected by the analyser. It is this rejection effect that is utilised for specific wavelength filtering. It is important to note that this will have an angular dependence due to the effective birefringence observed by the light being a function of incident angle.

$$T = \cos^2\left(\frac{\Gamma}{2}\right) = \cos^2\left(\frac{\pi\Delta n(V)d}{\lambda}\right). \quad (5.2)$$

5. LIQUID CRYSTAL LYOT FILTER

The LC material used here is *4-pentyl-4'cyanobiphenyl* (5CB) with an initial birefringence of ~ 0.2 . 5CB was filled into a *poly-vinyl-alcohol* (PVA) unidirectional planar aligned device (device fabrication described in further detail in chapter 4.2) with a cell gap of $d=(6.0\pm 0.2)\mu\text{m}$.

5.3 Results and discussion

5.3.1 Device spectra

The visible transmission spectra of the Lyot filter device was measured as a function of voltage ($V=0\rightarrow 30V_{rms}$, $f=1.0\text{kHz}$) using an **aligned** POM set up coupled to a UV/Vis spectrometer (described in chapter 4.2). The transmission spectra were normalised with respect to experimental losses and the temperature was kept at $T=(24.0\pm 0.1)^\circ\text{C}$.

The transmission of the LC Lyot filter with $0V_{rms}$ applied is shown in figure 5.2(a) where the fitting of equation 5.2 shows excellent agreement with experimental data. The spectrum seen in figure 5.2(a) is defined as the ON state, with the LC Lyot filter rejecting at specific wavelengths corresponding to the half wave-plate condition ($\lambda = 655\text{nm}$). Here we see rejection at this wavelength, with the transmission $<1.0\%$ between 648 and 665nm. Considering a red laser with power $P=500\text{mW}$, the incident power would be reduced to $\sim 5\text{mW}$, a class 3R low risk laser, providing protection against the damaging intensities. In reality this minimum in transmission at the rejection wavelength is limited solely by the polariser extinction ratio.

On application of higher voltage ($30V_{rms}$), figure 5.2(b), the LC birefringence approaches zero, as the device goes from the planar state towards the homeotropic state, thus achieving the OFF state. It is important to note that the OFF state corresponds to the high-voltage state and is denoted OFF to refer to the optical state, rather than the voltage state of the device. In the OFF state an almost uniform transmission across the viable spectrum is observed. Figure 5.2(b) also demonstrates the ability of the device to switch from transmitting uniformly across the visible spectrum (OFF), to rejection of specific wavelengths (ON).

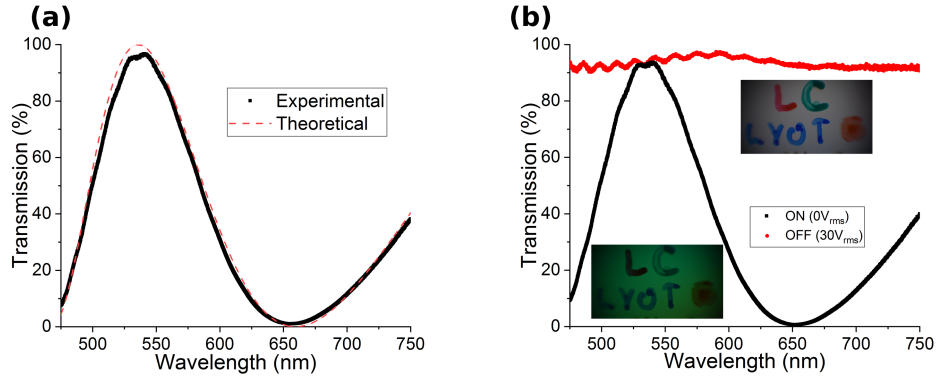


Figure 5.2: (a) The ON state experimental Lyot filter transmission as a function of wavelength. Theoretical fitting of equation 5.2 to the experimental data shows excellent agreement. (b) The ON ($0V_{rms}$) and OFF ($30V_{rms}$) experimental transmission of the single stage Lyot filter as a function of wavelength. In the ON state rejection at $\lambda=650\text{nm}$ is observed, whilst in the OFF state a uniform transmission across the spectrum is observed. Insert images, taken using a Nikon D7100 camera, demonstrate imaging through the device in the OFF (top) and ON (bottom) states. Even in protection mode partial observations are still possible.

The relatively high voltage required to achieve the OFF state would not impede the implementation of this device as the power requirements for LC devices is low. It can also be seen via the inserts in figure 5.2(b) that observations through the device whilst in protection mode are still possible, though at a reduced wavelength range.

5.3.2 Rejection wavelength tuning

Wavelength rejection tunability is achieved over the entire visible spectrum by varying the voltage applied to the LC Lyot filter. Continual variation of the applied voltage provides a continuous variation in the effective birefringence of the LC layer and therefore a continual shift to the half wave-plate condition. Figure 5.3(a) demonstrates that by varying voltage between 0.67 and $1.06V_{rms}$ the transmission spectrum blue-shifts. The rejected wavelength (half wave-plate

5. LIQUID CRYSTAL LYOT FILTER

condition) was tracked as a function of voltage and the subsequent relationship is demonstrated in figure 5.3(b). The relationship is effectively linear, although slight variation is observed close to the threshold voltage of the LC material. A wide tuneable range of possible rejection wavelengths is demonstrated (475 to 650nm), whilst in principle a much larger range can be accessed by utilising higher-order (increasing integer values of m) half-wave-plate conditions.

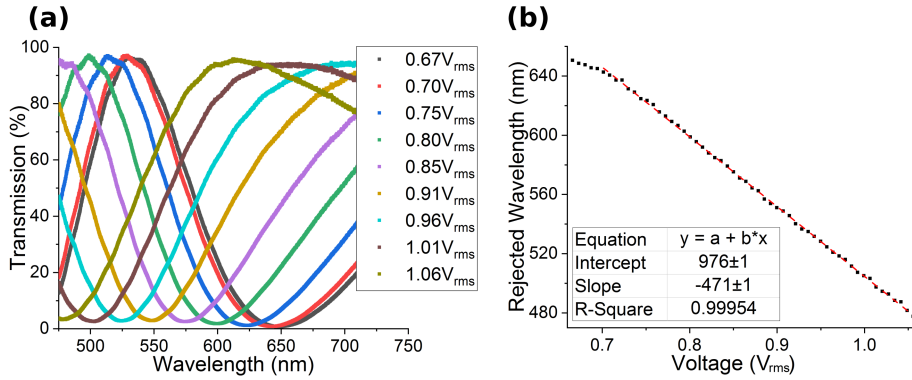


Figure 5.3: (a) The voltage dependence of the transmission spectra for the LC Lyot filter under investigation. The rejection wavelength clearly blue-shifts with increasing voltage. (b) The rejection wavelength (half-wave plate condition) is observed to depend linearly on voltage applied to the LC component.

The fitted linear relationship between rejection wavelength and applied voltage can be used as a calibration equation for this specific system.

$$\lambda_{rej} = 646 - \frac{471}{V - 0.70}. \quad (5.3)$$

For example, if a laser wavelength of $\lambda=532\text{nm}$ was dazzling the system the calibration equation can be used to calculate the required voltage to shift the half-wave-plate condition to match this wavelength. In this example a voltage of $(0.943 \pm 0.003)V_{rms}$ would be required.

5.3.3 Response speed

Coupling of the switching ability demonstrated in figure 5.2(b) and the tuning demonstrated in figure 5.3(a) the system can be switched from the OFF state to any arbitrary ON rejection state, with the response time limited by the detection system and the response time of the LC device (typically ms). The response time of the LC device was measured using a green laser diode ($\lambda=532\text{nm}$) with a POM setup coupled to a photodiode. The 10 \rightarrow 90% intensity values were used to measure the response time. Two waveform generators coupled to a high-voltage wideband amplifier were implemented to allow smooth switching between the ON (low voltage) and OFF (high voltage) states and also to allow smooth switching between different rejection (intermediate voltages) states.

Using equation 5.3 the blocking voltage required for this green laser diode is $(0.943\pm 0.003)V_{rms}$ and figure 5.4(a) demonstrates switching between the OFF ($30V_{rms}$) and the ON ($0.94V_{rms}$) state. The device demonstrated here reduces the green laser intensity to $(4.7\pm 0.1)\%$ of the maximum intensity.

The response time of a laser protection device is of crucial importance. It was demonstrated by Schwarz *et al.* [17] that the longer the exposure time the lower the laser power required to damage sensor systems. For this device the ON switching mechanism is a relaxation, rather than driven by an E-field, and is measured to be $\tau_{ON}=(60\pm 10)\text{ms}$. Switching back to the OFF transmission state is driven by an E-field and is therefore faster with $\tau_{OFF}=(45\pm 5)\mu\text{s}$.

Looking closely at figure 5.4(a) it can be seen that the transmitted intensity goes through an initial minimum before reaching the final ON state. This corresponds to the lower order half-wave-plate condition ($m=1$) passing through $\lambda=532\text{nm}$. In figure 5.2 and 5.3 the minima corresponds to the $m=2$ half-wave-plate condition. Here the response speed of the device could potentially be increased by utilising the $m=1$ half-wave-plate condition, however it has the disadvantage of a large full-width-half-maximum resulting in poor partial observations through the device. To further test the response speed of this device the three

5. LIQUID CRYSTAL LYOT FILTER

most currently accessible hand-held laser wavelengths were taken as $\lambda=650$, 532, and 405nm. From the calibration equation 5.3 this gives blocking voltages of 0.69, 0.94, and 1.21 V_{rms} respectively. The switching time between all the possible states is shown in figure 5.4(b).

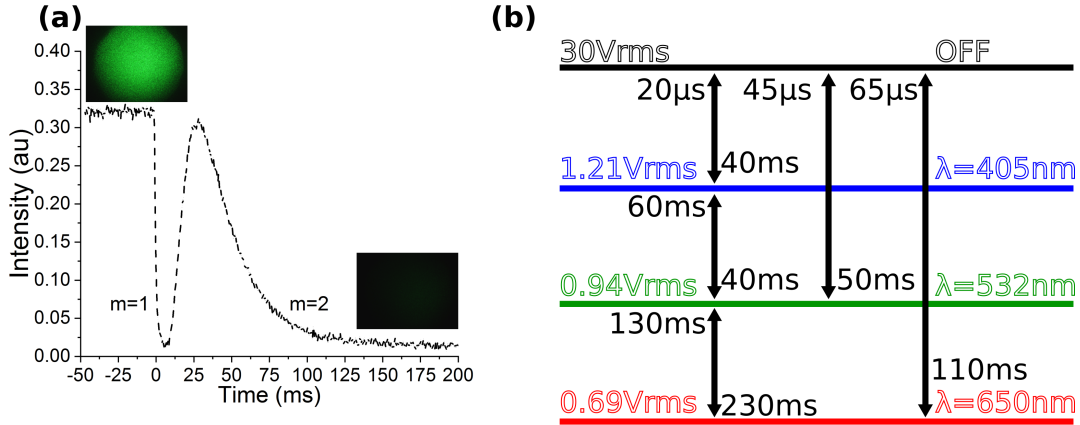


Figure 5.4: (a) Change in intensity with respect to time for switching the device between the OFF ($30V_{rms}$) and ON state ($0.940V_{rms}$) for rejection of the green laser. The switch is clear, with a response time of $\tau_{ON}=(60\pm 10)$ ms. Image inserts demonstrate the laser spot in the far field, taken using a deltaPix camera. (b) The ON and OFF response times associated with switching between protection schemes for typical laser wavelengths. Errors in the millisecond regime are ± 10 ms; in the microsecond regime are $\pm 5\mu$ s

In switching from the OFF state to a specific ON state the response time varied from 40-110ms. When switching between specific rejection states the response time varied from 40-230ms. The effectiveness of the system can be put into context by comparison with the laser threshold damage times measured by Schwarz [17]. It was found that if the exposure time of the continuous wave laser was kept below 250ms then power densities of up to 159kWcm^{-2} were unable to damage to the CCD camera. If a beam diameter of 6mm is assumed, then this power density corresponds to a laser power of 18W. Therefore, the switch speeds measured in this LC Lyot filter for switching into protection modes, all faster than 110ms, should provide excellent protection for CCD cameras against

continuous wave laser powers of up to 18W.

All together these results demonstrate the ease of implementation of this protective device. The validity of the calibration equation 5.3 has also been clearly shown and the response speed of the system is shown to protect for some large laser powers.

5.4 Summary

The design and testing of a tuneable, switchable, LC Lyot filter for laser protection was conducted using broadband and monochromatic sources. Rejection of laser wavelengths across the visible spectrum (475-650nm) was demonstrated by varying the voltage applied (0.67-1.06V_{rms}). However, the tuning range can be extended (avoiding LC and device absorptions) due to the extended transmission spectrum of the LC Lyot filter (higher/lower order half-wave-plate-conditions). The relationship between rejected wavelength and applied voltage was explored, allowing extraction of a calibration equation which can directly relate the voltage applied to the wavelength rejected. Switching between the OFF transmission mode and the ON protective mode was demonstrated by simply switching from a high voltage (30V_{rms}) to a lower voltage (0-1.06V_{rms}). The LC response time was investigated and found that switching from the OFF to ON states varied between 40 and 110ms, fast enough to provide protection for up to 18W laser sources.

The implementation of this device in sensor protection would be simple, with the calibration equation testing allowing for any temperature dependence to be accounted for. The system has been shown to be an strong candidate as a compact, rapid, and tuneable laser protection device.

In the next section a slight detour away from specific applications will be taken and the investigation into some specific dye-doped systems will be undertaken.

References

- [1] E. I. L. Jull and H. F. Gleeson. Tuneable and switchable liquid crystal laser protection system. *Applied Optics*, 56(29):8061–8066, 2017. [59](#)
- [2] B. M. Lyot and C. M. Fabry. Un monochromateur a grand champ utilisant les interferences en lumier polarisee. *Comptes rendus de l'Academie des Sciences Paris*, 197:1593–1595, 1933. [59](#)
- [3] B. M. Lyot. Planetary and solar observations on the pic du midi in 1941, 1942, and 1943. *Journal of Astrophysics*, 101:255–259, 1945. [59](#)
- [4] P. J. Miller. Use of tunable liquid crystal filters to link radiometric and photometric standards. *Metrologia*, 28:143–149, 1991. [60](#)
- [5] L. J. November and L. M. Wilkins. Liquid crystal polarimeter: a solid state imager for solar vector magnetic fields. *Optical Engineering*, 34:1659–1668, 1995. [60](#)
- [6] G. A. Kopp, M. J. Derks, D. F. Elmore, D. M. Hassler, J. C. Woods, J. L. Streete, and J. G. Blankner. Tunable liquid-crystal filter for solar imaging at the He I 1083-nm line. *Applied Optics*, 36:291–296, 1997.
- [7] W. Cau, J. Jing, J. Ma, Y. Xu, H. Wang, and P. R. Goode. Diffraction-limited polarimetry from the infrared imaging magnetograph at big bear solar observatory. *Publications of the Astronomical Society of the Pacific*, 118:838–844, 2006.
- [8] D. F. Elmore, G. L. Card, C. W. Chambellan, D. M. Hassler, H. L. Hull, A. R. Lecinski, R. M. MacQueen, K. V. Streander, J. L. Streete, and O. R. White. Chromospheric helium imaging photometer (an instrument for high time cadence 1083-nm wavelength solar observations). *Applied Optics*, 37:4270–4276, 1998.
- [9] K. Ichimoto, M. Noguchi, N. Tanaka, K. Kumagai, K. Shinoda, T. Nishino, T. Fukuda, and T. Sakurai. A new imaging system of the corona at norikura. *Publications of the Astronomical Society of Japan*, 51:383–391, 1999. [60](#)

- [10] S. M. Rees, J. Staromlynska, M. Gillyon, and J. R. Davy. Final design and testing of the laser airborne depth sounder filter. *Optical Engineering*, 36:1204–1213, 1997. [60](#)
- [11] R. S. Seymour, S. M. Rees, J. Staromlynska, J. Richards, and P. Wilson. Design considerations for a liquid crystal tuned Lyot filter for laser bathymetry. *Optical Engineering*, 33:915–923, 1994. [60](#)
- [12] H. F. Gleeson, A. J. Murray, E. Fraser, and A. Zoro. An electrically addressed liquid crystal filter for tunable lasers. *Optical Communications*, 212:165–168, 2002. [60](#)
- [13] H. R. Morris, C. C. Hoyt, and P. J. Treado. Imaging spectrometers for fluorescence and raman microscopy: acousto-optic and liquid crystal tunable filters. *Applied Spectroscopy*, 48:857–866, 1994. [60](#)
- [14] H. R. Morris, C. C. Hoyt, P. Miller, and P. J. Treado. Liquid crystal tunable filter Raman chemical imaging. *Applied Spectroscopy*, 50:805–811, 1996. [60](#)
- [15] A. Rees and J. Staromlynska. Automatic laser light detection and filtering using a liquid crystal Lyot filter. *International Journal of Nonlinear Optical Physics*, 2:661–676, 1993. [60](#)
- [16] C. Wu and S. Wu. Liquid-crystal-based switchable polarizers for sensor protection. *Applied Optics*, 34:7221–7227, 1995. [60](#)
- [17] B. Schwarz, G. Ritt, M. Koerber, and B. Eberle. Laser-induced damage threshold of camera sensors and micro-optoelectromechanical systems. *Optical Engineering*, 56:034108, 2017. [65](#), [66](#)

REFERENCES

Chapter 6

Dichroic dye doped systems

In this chapter a small detour away from specific switchable optical devices is taken and the investigation into some dichroic dyed guest-host systems will be presented. Research into the impact of high concentrations of a high-solubility anthraquinone-based dichroic dye on the physical parameters of a nematic LC host will be undertaken. The ability to dissolve high concentrations of dyes into a LC system is desirable in generating saturated colour in guest-host applications, but the impact of high concentrations on the nematic system is somewhat unclear due to typical concentrations being limited to less than 1% by weight [1].

The coupling of an anthraquinone dichroic dye into a LC elastomer (LCE) will also be investigated as a probe into the order of the system. Utilising the anisotropic absorption properties of the dichroic dye to directly measure the order parameter. This system will then be discussed in terms of its possible application as a rudimentary optical strain sensor. It is important to note that the LCE section of this chapter was done in collaboration with D. Mistry, M. Nikkhou, T. Raistrick, D. Baker, and H. F. Gleeson and should any of the work presented not be conducted by E. I. L. Jull it will be noted in the text [2].

6.1 High-solubility anthraquinone dye

As discussed in chapter 3 the solubility of anthraquinone-based dichroic dyes in LCs is typically very low at less than 1% ($\frac{w}{w}$) being common [1, 3-7]. Previous

6. DICHOIC DYE DOPED SYSTEMS

research has demonstrated some anthraquinone dyes which exceed $2\%(\frac{w}{w})$ [4–8] with the maximum solubility of an anthraquinone based dichroic dye in LCs measured to be $5.8\%(\frac{w}{w})$ [4, 7, 9].

In this section, a newly developed high-solubility anthraquinone dye, synthesised by the Chemistry Department at the University of York, is investigated. The effect of high-concentrations of this dye on the nematic LC host physical parameters will be experimentally determined. Due to standard anthraquinone-based dichroic dye’s typically low solubility in LCs the general effect of the addition of these dye’s on the LC physical parameters is somewhat uncharacterised (typically assumed to be a negligible effect). High concentrations of dopant will clearly generate an impact on the system and therefore characterisation of this is important when considering guest-host applications utilising high concentrations of dye to achieved high colour saturation.

The impact of high concentrations of anthraquinone dye on the nematic system phase diagram, elastic properties, dielectric properties, and optical properties will be investigated. The low availability of the high-solubility dye resulted in limited datasets and also meant that the maximum solubility of the dye in the typical LC 5CB could not be directly established, although it is estimated, as demonstrated later in this section, to be approximately $7\%(\frac{w}{w})$.

6.1.1 Materials and methods

2,6-bis(4-((butyldimethylsilyl)oxy)phenyl)anthracene-9,10-dione (RM1790) demonstrates variation from typical anthraquinone-based dyes [10] in the inclusion of silicon into the extended structure, it is this inclusion which is attributed to the material’s high-solubility. This dye is doped into typical nematic host 5CB in concentrations of 1.0, 5.0, and $14.6\%(\frac{w}{w})$.

These mixtures were filled into planar aligned (SE3510 polyimide treated), approximately $5\mu m$ and $10\mu m$ cell gap, LC cells for experimental analysis in

optical, elastic, and electric properties.

The phase diagram was established through a combination of DSC and POM. The optical/absorption properties of RM1790 is found through single polarised microscopy coupled with a spectrometer. Finally, the elastic and electrical properties of each mixture are established via measurements of the capacitance dependence on applied voltage. Fitting of the relationship between capacitance and voltage, discussed in chapter 2.6, allows the elastic and dielectric properties of the system to be found. The dependence of these properties on dye concentration will then be described. All methodology used here is described in detail in chapter 4.

6.1.2 Phase effects

The variation of phase transition temperatures on RM1790 dye concentration in 5CB was measured via DSC, results summarised in table 6.1 and shown in figure 6.1(a). An increased nematic temperature range is demonstrated across all dye concentrations, similar to that observed by Gurulk [1] in which a 0.8°C increase in the nematic to isotropic phase transition temperature was observed for $0.2\%(\frac{w}{w})$ anthraquinone dye concentration in nematic E63 LC. The nematic (N) to isotropic (I) transition temperature is found to increase with increasing RM1790 concentration in 5CB from $36.1 \rightarrow 39.7^{\circ}\text{C}$. The crystal (K) to nematic phase transition temperature is found to decrease roughly with increasing dye concentration in 5CB, although a slight inflection is noted at the highest concentration.

It is found that the highest concentration mixture, $14.6\%(\frac{w}{w})$ RM1790 in 5CB, exhibits phase separation of the dye, confirmed through POM (figure 6.1(c)) and DSC measurements (figure 6.1(d)). This indicates that this concentration is above the solubility limit of this dye in 5CB, with recrystallisation of the dye out of solution found at temperature of less than approximately 60°C . Analysis of lower concentrations of RM1790 in 5CB would have been conducted, however availability of the material meant this was unable to be investigated fully.

6. DICHOIC DYE DOPED SYSTEMS

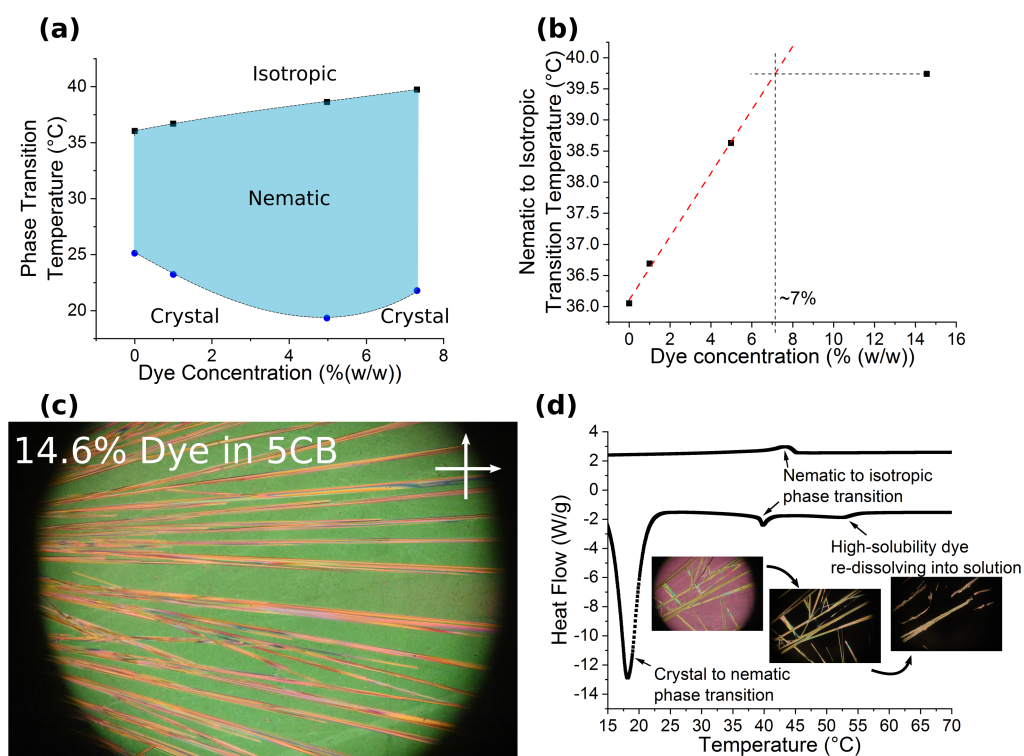


Figure 6.1: (a) The phase transition temperature dependence on RM1790 dye concentration in 5CB is shown, measured via DSC (error in transition temperature given as $\pm 0.1^\circ\text{C}$). (b) The nematic to isotropic phase transition temperature dependence on the concentration of RM1790 in 5CB. Extrapolation of the over saturated concentration to find the solubility limit is demonstrated. (c) POM demonstrates clear phase separation of the dye in the highest concentration sample. (d) The DSC heat flow trace for 14.6% ($\frac{w}{w}$) RM1790 in 5CB. The bottom trace is the sample on heating and the enthalpy change associated with dissolving the re-crystallised dye back into solution is observed at approximately 52°C . This is confirmed via POM, with image inserts demonstrating each temperature regime of the system.

The enthalpy change measured on the **heating** cycle of the 14.6% ($\frac{w}{w}$) dye-doped sample during DSC can be considered to be the phase transition temperature for the *maximum* solubility limit. This can be assumed as any "excess" dye will have phase separated out of the solution during the cooling cycle of the

6.1 High-solubility anthraquinone dye

Dye concentration ($\%(\frac{w}{w})$)	T_{KN} ($^{\circ}C$) [$\pm 0.1^{\circ}C$]	T_{NI} ($^{\circ}C$) [$\pm 0.1^{\circ}C$]
0 [5CB]	25.1	36.1
1.0	23.2	36.7
5.0	19.3	38.6
14.6	21.8	39.7
100 [Pure dye]	$T_{KI} = 48.5$	N/A

Table 6.1: Table summarising the phase transition temperatures of varying high-solubility dye concentration in 5CB, measured via DSC. This data is shown in figure 6.1(a).

experiment, to confirm this a closer look at the DSC trace is undertaken.

Looking at the DSC trace for the highest concentration solution, figure 6.1(d), it is firstly noted that the re-dissolving of the dye into solution is observed at approximately $52^{\circ}C$, this is confirmed via POM measurements demonstrating how the excess dye appears in the system on heating, and re-dissolves into the solution at temperatures greater than approximately $52^{\circ}C$.

DSC as a method for the identification of phase transition temperatures in LC samples typically demonstrates a small amount of hysteresis between the cooling and heating cycles, typically demonstrating a lower nematic to isotropic phase transition temperature on cooling. However, in the DSC trace shown in figure 6.1(d) it can be seen that there is in fact an increased nematic to isotropic phase transition on the cooling cycle (39.7 compared to $43.4^{\circ}C$). This is a direct result of the additional (excess) dye in the system that has re-dissolved into the solution at high temperatures and has yet to phase separate back out (which is time and temperature dependant). The lower nematic to isotropic phase transition temperature on heating, coupled with the low temperatures reached in this experimental procedure ($-50^{\circ}C$), allows for the assumption that all the excess dye will have re-crystallised out of the system on the cooling cycle and that the phase transition temperature on heating is that of the highest-solubility concentration of dye in 5CB.

6. DICHOIC DYE DOPED SYSTEMS

Therefore, if it is assumed that the relationship between nematic to isotropic phase transition temperature and dye concentration in 5CB is linear as shown in figure 6.1(b), the phase transition temperature measured on heating for the over-solubility-limit concentration can be extrapolated back to give the maximum possible solubility of this dye in 5CB, shown to be approximately $7\%(\frac{w}{w})$.

The approximated maximum solubility limit projected demonstrates the highest measured solubility of an anthraquinone dye in LCs, although it is noted that further experiments are required to confirm this. The mapping of the nematic to isotropic and the crystal to nematic phase transition temperatures has demonstrated that the incorporation of this specific dichroic dye into the nematic LC 5CB has generated an increase in the effective nematic temperature regime. This is a desirable property for guest-host applications as the addition of the dichroic dye to the LC does not cause detrimental effects to the effective temperature regime.

6.1.3 Optical properties

The optical properties of RM1790 in 5CB will now be investigated using single polarised microscopy coupled to a visible spectrometer. The absorption spectrum of the RM1790 in 5CB is shown in figure 6.2(a) with the absorption of polarised light parallel and perpendicular to the nematic director. The absorption peak is clearly seen at $\lambda = (403.1 \pm 0.4)nm$, with Gaussian fitting utilised to aid in identification of the peak wavelength. The dependence of absorption on the input polarisation angle with respect to the director is also demonstrated. As expected the absorption is greater when the polarisation is parallel to the director (closely aligned with the transitional dipole moment).

The absorption coefficient parallel and perpendicular to the director is an important parameter when considering the optical capabilities of any dye doped guest-host device. In measuring the absorption coefficients for this high-solubility dye doped system the absorption at 400nm was measured with the polarised light

6.1 High-solubility anthraquinone dye

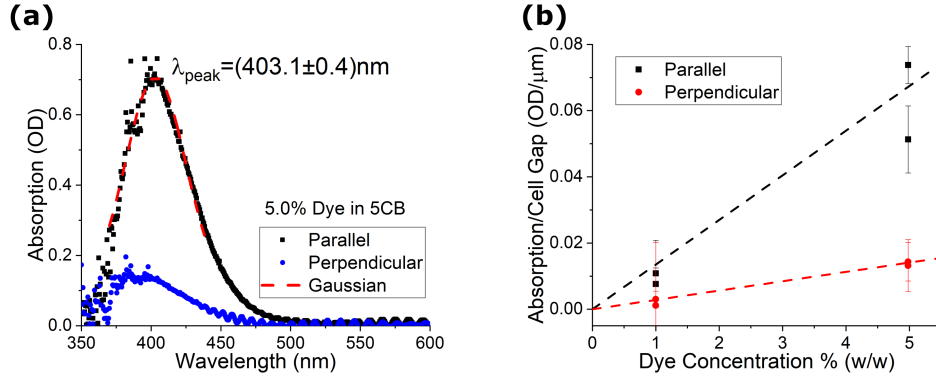


Figure 6.2: (a) The absorption spectrum for 4.98% ($\frac{w}{w}$) RM1790 in 5CB in a planar aligned device with the light polarised parallel and perpendicular to the nematic director, normalised with respect to pure 5CB. (b) The absorption normalised with respect to cell gap (polarisation parallel and perpendicular to the director) dependence on dye concentration in 5CB. The Beer-Lambert relationship is fit to calculate the absorption coefficients for each orientation.

parallel and perpendicular to the director for various concentrations. This absorption was normalised with respect to cell gap (light path) and the relationship is demonstrated in figure 6.2(b). It is noted that there is a somewhat restricted amount of data due to limits in dye availability only allowing 3 varying concentration mixtures to be generated, and the error associated with the spectrum measurement is low and does not truly represent the error in this measurement. The error in establishing the Beer-Lambert relationship can be truly represented via multiple experimental runs and chapter 7.3.3 demonstrates an approximate scatter of 5% around an average absorption value. The phase separation in the over-solubility limit system prevents accurate optical measurements due to the scattering generated when the dye dissolves out of the system.

The Beer-Lambert relationship, equation 6.1, can be fit to the experimental data to find the absorption coefficient α , parallel and perpendicular to the director for this dye system. The fitting gave coefficients $\alpha_{\parallel} = (0.012 \pm 0.001) OD \mu m^{-1} \%(\frac{w}{w})^{-1}$ and $\alpha_{\perp} = (0.0027 \pm 0.0001) OD \mu m^{-1} \%(\frac{w}{w})^{-1}$ which can be used in predictions for the optical characteristics for this system.

6. DICHOIC DYE DOPED SYSTEMS

$$A = \alpha dc \tag{6.1}$$

These coefficients will allow for the calculation of expected absorption depending on the device cell gap and concentration of dye in 5CB. This is crucial when considering the capabilities of a guest-host device.

6.1.4 Elastic and dielectric properties

The elastic and dielectric properties of the dye doped system were investigated by measuring the voltage dependence of capacitance, methodology described in chapter 4.4, and fitting the theoretical model discussed in chapter 2.6. The splay and bend elastic constants (k_{11} and k_{33}) were determined along with the parallel and perpendicular permittivity (ϵ_{\parallel} and ϵ_{\perp}), to a 5% accuracy as discussed in chapter 4.4, and each of these physical parameter's dependence on dye concentration will be discussed. These results will be plotted as a function of reduced temperature, with the nematic to isotropic transition temperature determined from the DSC experimental data (table 6.1) to remove any order parameter dependencies.

Figure 6.3(a) demonstrates how the splay elastic constant varies with reduced temperature for the different concentrations of RM1790 in 5CB. It can be seen that there is a general reduction in k_{11} with increasing dye concentration, though the change is relatively small.

Figure 6.3(b) demonstrates how the bend elastic constant varies with temperature for different dye concentrations in 5CB. It is noted that k_{33} shows a reduction with increasing dye concentration. The change here is slightly larger than the change in k_{11} , but is only an approximate 10% relative reduction.

Finally, figure 6.3(c) demonstrates how the dielectric permittivity parallel and perpendicular to the director changes with reduced temperature for various dye concentrations. Little to no change is observed in the perpendicular permittivity with increasing dye concentration. However, a systematic reduction in the

6.1 High-solubility anthraquinone dye

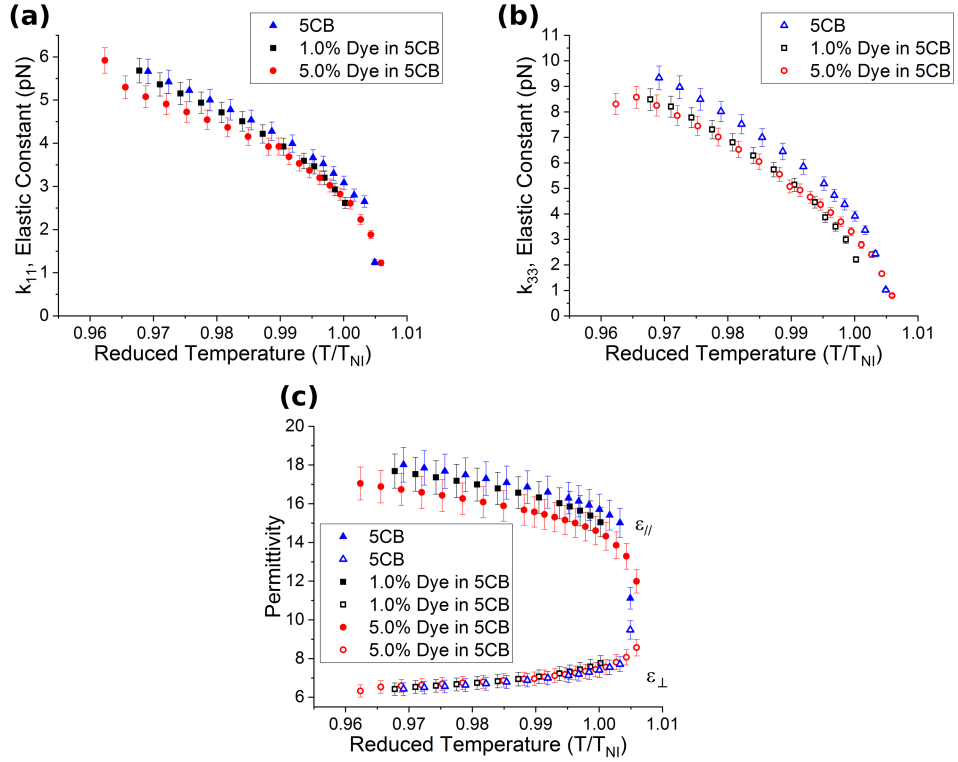


Figure 6.3: The dependence of (a) splay elastic constant, (b) bend elastic constant, and (c) dielectric permittivities on reduced temperature for varying concentration of RM1790 in 5CB.

parallel permittivity is noted with increasing dye concentration in 5CB, with the relative reduction in parallel permittivity being -1.8% for 1.00% and -7.1% for 5.00% dye concentration. The reduction in $\epsilon_{||}$ is very notable and shows a clear reduction with increasing concentration.

The impact of the high concentrations of dyes on the nematic system is important in device considerations. In terms of the elastic properties there is a small reduction in both the splay and bend elastic constants, whilst in terms of dielectric properties there is no change in the perpendicular permittivity, but a systematic reduction in the parallel permittivity with increasing dye concentration. This reduction in the parallel permittivity, and subsequently the reduction

6. DICHOIC DYE DOPED SYSTEMS

to dielectric anisotropy ($\Delta\epsilon = \epsilon_{\parallel} - \epsilon_{\perp}$), will impact the response to the system to an electric field and therefore impact the overall capabilities of an electrically addressed guest-host device. The same can be said for the change in elastic constants which will result in a change to the systems response to external stimuli.

6.1.5 High-solubility summary

The effect of a high-solubility anthraquinone dye on the nematic LC system was investigated in terms of the phase, optical, elastic, and dielectric properties. A solubility limit of approximately $7\%(\frac{w}{w})$ was projected via phase transition measurements of an over-saturated mixture. An increased nematic temperature range was observed with increasing dye concentrations in 5CB. Excellent absorptive properties were observed via single polarised microscopy coupled with a visible light spectrometer. Absorption coefficients for the parallel and perpendicular polarised light with respect to the direct were calculated as $\alpha_{\parallel} = (0.012 \pm 0.001)OD\mu m^{-1}\%(\frac{w}{w})^{-1}$ and $\alpha_{\perp} = (0.0027 \pm 0.0001)OD\mu m^{-1}\%(\frac{w}{w})^{-1}$, an important characteristic when discussing guest-host device capabilities.

The elastic splay and bend constants were found to decrease with increasing dye concentration in 5CB. The electrical permittivity perpendicular to the director remained unchanged with dye concentration, whilst the parallel permittivity decreased systematically with increasing concentration of dye in 5CB. The impact of dye concentration on these physical parameters is an important consideration in the development of electrically switchable guest-host devices containing high concentrations of this highly-soluble anthraquinone dichroic dye.

6.2 Guest-host LC elastomer

Here an investigation into a nematic acrylate liquid crystal elastomer (LCE) was conducted and the coupling of an anthraquinone dichroic dye orientation to the nematic ordering of the LCE system was investigated. This work was conducted in collaboration with D. Mistry, M. Nikkhou, T. Raistrick, D. Baker, and H. F. Gleeson [2]. The main focus of E. I. L. Jull's experimental work in this collaboration was surrounding the dichroic dye guest-host interaction with the system and therefore that will be the main focus of this section.

A nematic acrylate LCE was investigated, described in detail by Mistry [11], with isotropic templating generating a LCE which has no LC behaviour as a function of temperature. However, when under strain nematic-like ordering is observed in the system. Anthraquinone dye 15NB3 synthesised by Ellis [12] was doped into the LCE system to investigate the coupling of the guest to the strain-induced nematic ordering of the LCE host. This dye was utilised due to its mid-visible absorption and high dye order parameter, $S_\beta = 0.914$ [3].

6.2.1 Materials and methods

The LCE sample was prepared from acrylate monomers [11] with the addition of 0.1% ($\frac{w}{w}$) of 15NB3 anthraquinone dye. This material was fabricated in collaboration between E. I. L. Jull, D. Mistry, and M. Nikkhou [2]. The mixture was filled into a thin-film template with glass bottom and Melinex top, with a thickness of approximately $100\mu m$. The top and bottom substrates were untreated to generate an isotropic LCE. The samples were then UV cured for 120 minutes before removal from the mould.

The isotropic state was confirmed from the dark state observed at all angles in POM. 2.5cm wide stripes were cut from the bulk sample for testing on the strain rig. The sample was loaded into a manual strain rig and mounted on a POM setup. The strain induced in the LCE was monitored via particle separation tracking from images taken and the transmission spectrum for polarised light was monitored at 0° and 90° between the polarisation and the strain axis. The

6. DICHOIC DYE DOPED SYSTEMS

spectrum measurements were conducted using a 20x objective and normalising to a non-dye doped LCE sample of similar strain to account for variation in thickness.

6.2.2 Results and discussion

The absorption spectrum of the 15NB3 doped LCE was monitored (peak absorption at 550nm), using a visible spectrometer, as a function of strain to allow calculations of the order parameter dependence on strain. The order was calculated through the guest-host theory discussed previously in chapter 3.1.2, with the β angle found via theoretical modelling to be 13.8° [10]. Figure 6.4(a) gives an example of the low and high strain absorption spectrum for the dye-doped LCE normalised to a non-dye doped LCE.

It can be seen that at low strain there is no variation in absorption with changing polarisation angle, a direct result of the lack of order in the isotropic system. However, at increased strain the system becomes nematic-like, generating a polarisation angle dependence in the absorption. By measuring the peak absorption values parallel and perpendicular to the strain axis the order parameter of the system can be calculated.

The strain was monitored via particle tracking of macroscopic images shown in figure 6.4(b, c). The particles were tracked with the strain given as the ratio of the distance between particles to the original distance between particles, $(\frac{\Delta x}{\Delta x_0})$.

Figure 6.5(a) demonstrates the direct relationship between order parameter ($\langle P_2 \rangle$) of the system and strain at room temperature. It is directly compared with Raman spectroscopy [13, 14] data collected by M. Nikkhou showing strong agreement between experimental procedures. A temperature independent linear increase in the order parameter of the system is observed with increasing strain in figure 6.5(b), demonstrating a strain-induced nematic-like system. A maximum order parameter of $S = (0.28 \pm 0.01)$ is achieved before the fracture point of the sample was reached ($T=9.5^\circ C$). In comparing this with other LCE systems [15]

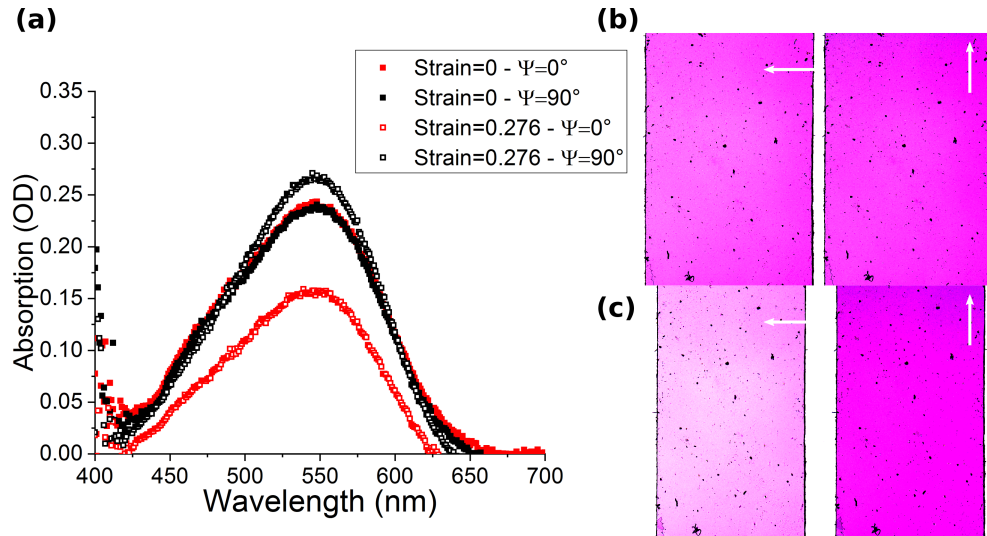


Figure 6.4: (a) The absorption spectrum for the 15NB3 doped LCE at zero strain and high strain is demonstrated for polarisation angles (ϕ) of 0 and 90° to the strain axis. (b) The low strain macroscopic image of the sample with polarisation at 0 and 90° shown. (c) The high strain macroscopic image of the sample with polarisation at 0 and 90° shown. (b, c) Images have increased contrast and lightness to help demonstrate the variation in transmission between polarisation angle.

it is noted that for other such systems the strain dependency of the order parameter has significant temperature dependence, must be close to the nematic to isotropic transition temperature, and demonstrates a non-linear response in order under strain. However, as demonstrated here the LCE material utilised in these experiments generates a linear response in the order parameter under strain, with no difference between temperatures. There is also no nematic to isotropic phase transition in this material due to its isotropic templating.

The result shown in figure 6.5 demonstrates coupling between the 15NB3 dichroic dye and the LCE host director. The guest-host effect has proven a simple yet effective method for measuring the order parameter of this LCE system.

Here it is suggested that the coupling of the anthraquinone dye with the LCE order and the strain induced order could be utilised in an optical strain sensor.

6. DICHOIC DYE DOPED SYSTEMS

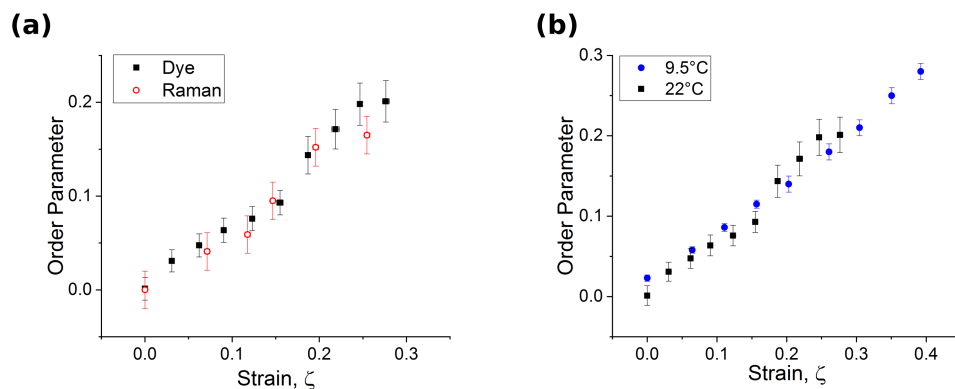


Figure 6.5: The order parameter dependence on strain for the 15NB3 doped LCE as measured via the polarisation angle dependent absorption properties. (a) Room temperature data is directly compared with Raman spectroscopy order parameter data collected by M. Nikkhou. (b) A comparison of 9.5 and 22°C order parameter dependence of strain measured via the 15NB3 absorption properties.

The transmission of light can be directly related to the strain induced on the system, with the contrast between parallel and perpendicular polarisation transmission increasing with increasing strain, figure 6.6. This could be utilised as an optical strain sensor, exhibiting a clear continuous change in transmission when a strain is applied.

6.2.3 Dye-doped LCE summary

In this section the coupling between an anthraquinone-based dichroic dye (guest) and a LCE (host) was investigated. The LCE demonstrates nematic-like ordering under strain and the dichroic dye was utilised as a simple mechanism for measuring the order parameter of the system, demonstrating excellent agreement with independent Raman experimental measurements. This has shown a good coupling between the dichroic dye and the LCE host order. It is suggested that the dye-doped LCE could be utilised as a simple optical strain sensor which would demonstrate a change in transmission when under strain.

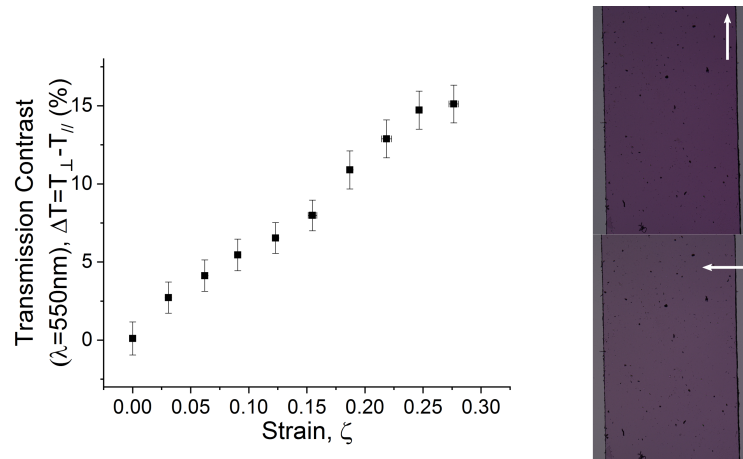


Figure 6.6: The contrast in transmission at 550nm is demonstrated as a function of strain for 15NB3 doped LCE. Image inserts demonstrate macroscopic view of the material at a strain of (0.276 ± 0.004) demonstrating the colour difference between the two polarisation angles with respect to the strain direction.

6.3 Summary

In this chapter two investigations were undertaken into dichroic dye doped guest-host systems. Characterisation of the impact of a high-solubility anthraquinone dye on the optical, elastic, and dielectric properties of the nematic host 5CB was conducted. The solubility limit was projected to be approximately $7\%(\frac{w}{w})$ and a reduction in the splay and bend elastic constant, as well as the parallel dielectric permittivity, were found with increasing dye concentration. The impact of high concentrations of dichroic dyes on the nematic system is important in considerations of guest-host device capabilities.

A LCE doped with anthraquinone dye 15NB3 was investigated for the ability of the dichroic dye to couple to the LCE order. The order parameter was found to vary linearly as a function of strain via the dichroic dye absorption properties. A maximum order parameter of $S = (0.28 \pm 0.02)$ was observed and a transmission contrast, for the dye doped LCE, of 15% was achieved. The system was proposed as a simple optical strain sensor with the ability to change absorption properties

6. DICHOIC DYE DOPED SYSTEMS

continually under strain.

In the next few chapter the primary investigation conducted during this PhD will be demonstrated. The investigation into the physical impact of the photoisomerisation process on a nematic LC will be conducted and the physical mechanisms involved will be identified.

References

- [1] M. Gurulk, H. A. Abdulkadir, M. S. Akkus, F. Akkurt, and A. Alicilar. Comparison of guest-host liquid crystal systems doped with azo or anthraquinone dyes. *Iranian Journal of Science and Technology Transactions A: Science*, 41:1–5, 2017. [71](#), [73](#)
- [2] D. Mistry, M. Nikkhou, T. Raistrick, E. I. L. Jull, D. Baker, and H. F. Gleeson. Isotropic liquid crystal elastomers as exceptional photoelastic materials and stress sensors. *under submission*, 2019. [71](#), [81](#)
- [3] M. T. Sims, L. C. Abbott, S. J. Cowling, J. W. Goodby, and J. N. Moore. Experimental and molecular dynamics studies of anthraquinone dyes in a nematic liquid-crystal host: a rationale for observed alignment trends. *Physical Chemistry Chemical Physics*, 18:20651–20663, 2016. [71](#), [81](#)
- [4] H. Iwanaga and F. Aiga. Correlations among molecular structures, solubilities in fluorinated media, thermal properties and absorption spectra of anthraquinone dichroic dyes with phenylthio and/or anilino groups. *Liquid Crystals*, 38(2):135–148, 2011. [72](#)
- [5] H. Iwanaga, K. Naito, and F. Aiga. Properties of novel yellow anthraquinone dichroic dyes with naphthylthio groups for guest-host liquid crystal displays. *Journal of Molecular Structure*, 975:110–114, 2010.
- [6] H. Iwanaga, K. Naito, and Y. Nakai. The molecular structures and properties of anthraquinone-type dichroic dyes. *Molecular Crystals and Liquid Crystals*, 364:211–218, 2001.
- [7] H. Iwanaga and K. Naito. Highly soluble anthraquinone dyes with CF₃-groups for guest-host liquid crystal displays. *Japanese Journal of Applied Physics*, 37:356–358, 1998. [71](#), [72](#)
- [8] W. Zhang, C. Zhang, K. Chen, Z. Wang, M. Wang, H. Ding, J. Ziao, D. Yang, H. Yu, L. Zhang, and H. Yang. Synthesis and characterisation of liquid crystalline anthraquinone dyes with excellent dichroism and solubility. *Liquid Crystals*, 43(10):1307–1314, 2016. [72](#)

REFERENCES

- [9] H. Iwanaga. Development of highly soluble anthraquinone dichroic dyes and their application to three-layer guest-host liquid crystal displays. *Materials*, 2:1636–1661, 2009. [72](#)
- [10] M. T. Sime, L. C. Abbott, S. J. Cowling, J. W. Goodby, and J. N. Moore. Molecular design parameters of anthraquinone dyes for guest-host liquid-crystal applications: Experimental and computational studies of spectroscopy, structure, and stability. *The Journal of Physical Chemistry C*, 120:11151–11162, 2016. [72](#), [82](#)
- [11] D. Mistry, P. B. Morgan, J. H. Clamp, and H. F. Gleeson. New insights into the nature of semi-soft elasticity and “mechanical-Fréedericksz transitions” in liquid crystal elastomers. *Soft Matter*, 14:1301–1310, 2018. [81](#)
- [12] S. J. Cowling, C. Ellis, and J. W. Goodby. Anthraquinone liquid crystal dichroic dyes - a new form of chromonic dye? *Liquid Crystals*, 38(11-12):1683–1698, 2011. [81](#)
- [13] H. F. Gleeson, C. D. Southern, P. D. Brimicombe, J. W. Goodby, and V. Gortz. Optical measurements of orientational order in uniaxial and biaxial nematic liquid crystals. *Liquid Crystals*, 37(6-7):949–959, 2010. [82](#)
- [14] J. P. F. Lagerwall and G. Scalia. *Liquid crystals with nano and microparticles volume 1*. World Scientific, 2016. [82](#)
- [15] W. Kaufhold and H. Finkelmann. Effect of the spacer length on the mechanical coupling between network anisotropy and nematic order. *Die Makromolekulare Chemie*, 192:2555–2579, 1991. [82](#)

Chapter 7

Photoisomerisation of BAAB2

In the next three chapters the effects of the photoisomerisation process of BAAB2 azobenzene-LC dopant on the nematic LC host 5CB will be investigated and the underlying physical mechanisms involved will be established.

This chapter will begin with the phase and optical characterisation of the pure BAAB2 azobenzene-LC material. The effect of doping nematic LC 5CB with BAAB2 at various concentrations will then be presented. The impact of BAAB2 concentration on the phase sequence, in un-irradiated and low-power continuous wave laser irradiation conditions will be investigated. Analysis of the impact of the photo-induced change on the nematic to isotropic phase transition temperatures (T_{NI}) will be shown.

The temperature dependence of the nematic order parameter in the BAAB2 doped 5CB system, measured directly via guest-host anthraquinone dye interactions, will then be presented for yellow-filtered and UV-irradiated conditions. This will give direct insight into the effect the azobenzene material itself has on the order parameter of the nematic system, as well as the direct effect of the *trans* to *cis* photoisomerisation process. The nematic to isotropic phase transition temperatures will be accurately evaluated and direct comparison with theoretical predictions will be undertaken.

7. PHOTOISOMERISATION OF BAAB2

In these investigations of this light-sensitive material the experimental light conditions are incredibly important in understanding and discussing the observed results. Therefore, the different light exposure conditions are defined below to aid in clarity during discussions in these chapters:

- Un-irradiated defines experiments in which no light impacts the system and it is assumed that no photoisomerisation has occurred. This occurs in DSC experimentation and the results will include the subscript *UnIrr* (e.g. $T_{NI-UnIrr}$).
- Red-filter defines experiments in which the light impacting the system is restricted to wavelengths greater than $\lambda = 580nm$ and it is again assumed that no photoisomerisation has occurred. This is utilised in some POM experiments and results will include the subscript *red* (e.g. T_{NI-red}).
- Yellow-filter defines experiments in which the light impacting the system has wavelengths between 405 and 430nm removed. This is utilised in some POM experiments and will include the subscript *yellow* (e.g. $T_{NI-yellow}$). In these experiments it is demonstrated that the low-intensity light at approximately 400nm results in low levels of photoisomerisation of the BAAB2 dopant.
- Laser irradiation in experiments is achieved via coupling of a low-power (0.5mW) $\lambda = 405nm$ continuous wave laser, resulting in high amounts of photoisomerisation. This will be defined in experimental results with the subscript *laser* (e.g. $T_{NI-laser}$).
- UV irradiation in experiments is achieved via illumination from an **unpolarised** high-intensity broadband UV source, resulting in full photoisomerisation of the sample. This will be defined in experimental results with the subscript *UV* (e.g. T_{NI-UV}).

7.1 BAAB2

4-2-butyl-4'-2-alkoxyazobenzene (BAAB2) is part of a LC azobenzene series synthesised by V. A. Grozhik [1]. The BAAB- series has previously been studied in terms of their optical switching properties [2, 3], potential use as a drug delivery system [4], and their effect on cholesteric LCs [5].

BAAB2 (figure 7.1) is an azobenzene-based material with its own LC phase. Due to its azobenzene linkage group the material demonstrates a light-dependent phase diagram. Throughout this chapter the un-irradiated (non-photoisomerised) state of the material or mixture will first be defined to give a baseline measurement for comparison. Once the baseline measurement is obtained the effect of irradiation on the sample (photoisomerisation) can be fully understood. Here, the investigation into the phase diagram of BAAB2 through DSC, red-filtered POM, and monochromatic POM laser transmission will be presented.

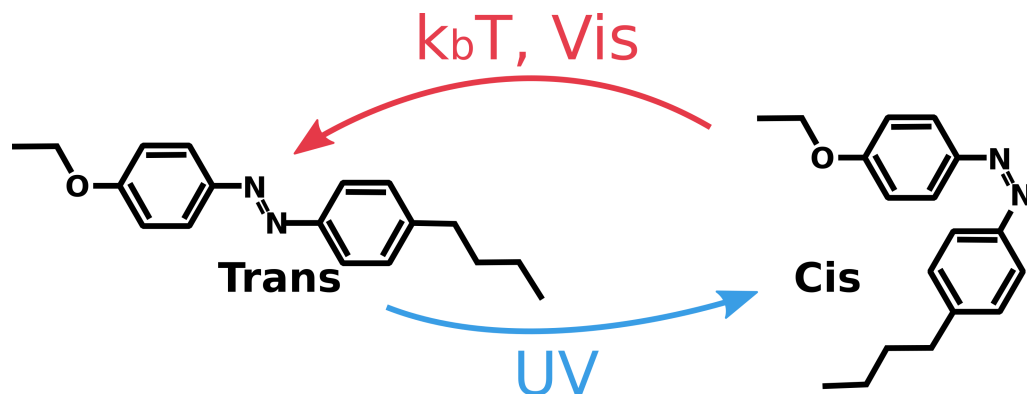


Figure 7.1: The chemical structure of BAAB2 is shown. The *trans* and *cis* conformers are demonstrated.

7.1.1 BAAB2 phases

BAAB2 is shown to only exhibit a nematic LC phase [4] when in the relaxed unexcited state. BAAB2 does not exhibit smectic phases like some of the longer chain length BAAB- series molecules (e.g. BAAB6 [4]). To establish the phase

7. PHOTOISOMERISATION OF BAAB2

diagram of BAAB2 in the un-irradiated state the first investigation conducted was DSC (described in chapter 4.3). This is an excellent method for these photosensitive materials as the sample is encapsulated in a light-tight pan which ensures no ambient light can trigger photoisomerisation.

The DSC heat flow versus temperature is shown for BAAB2 in figure 7.2(a) with the temperature scan rate set to $10^{\circ}Cmin^{-1}$. The top line represents the cooling scan from the isotropic (I) state. An enthalpy change is observed at $(82.4 \pm 0.1)^{\circ}C$ and is associated with the transition into the nematic (N) phase. An enthalpy change corresponding to the nematic to crystal (K) phase transition is not observed on cooling until a much lower temperature due to super-cooling. Due to super cooling any phase transition temperatures will be quoted from the heating cycle of the sample. The heating cycle is the bottom line on the DSC scan, figure 7.2(a). An enthalpy change is observed at $(48.5 \pm 0.1)^{\circ}C$ which is attributed to the crystal to nematic phase transition. A second enthalpy change is observed on heating at $(83.5 \pm 0.1)^{\circ}C$ which is assumed to correspond to the nematic to isotropic phase transition temperature. The transition temperatures are found to be in agreement with previous literature [4].

To confirm the phases of BAAB2 in the temperature regimes given by the DSC scan the BAAB2 material was filled into a random planar alignment LC cell. POM (described in chapter 4.2), with a red filter blocking wavelengths $\lambda < 580nm$ to prevent photoisomerisation, was then used to observe the optical textures which can be directly related to a phase. POM images shown in figure 7.2(c) demonstrate the crystal phase at temperatures below $48^{\circ}C$. Upon heating, the BAAB2 sample transitions into the schlieren texture, confirming it is in the nematic phase in the indicated temperature range. Finally, at $83^{\circ}C$ the phase transition to the isotropic state is observed, with the isotropic state being dark between crossed polarisers due to the lack of birefringence. Whilst the identification of phases was clear from the POM images, the actual onset of the crystal to nematic phase transition temperature was somewhat difficult to measure.

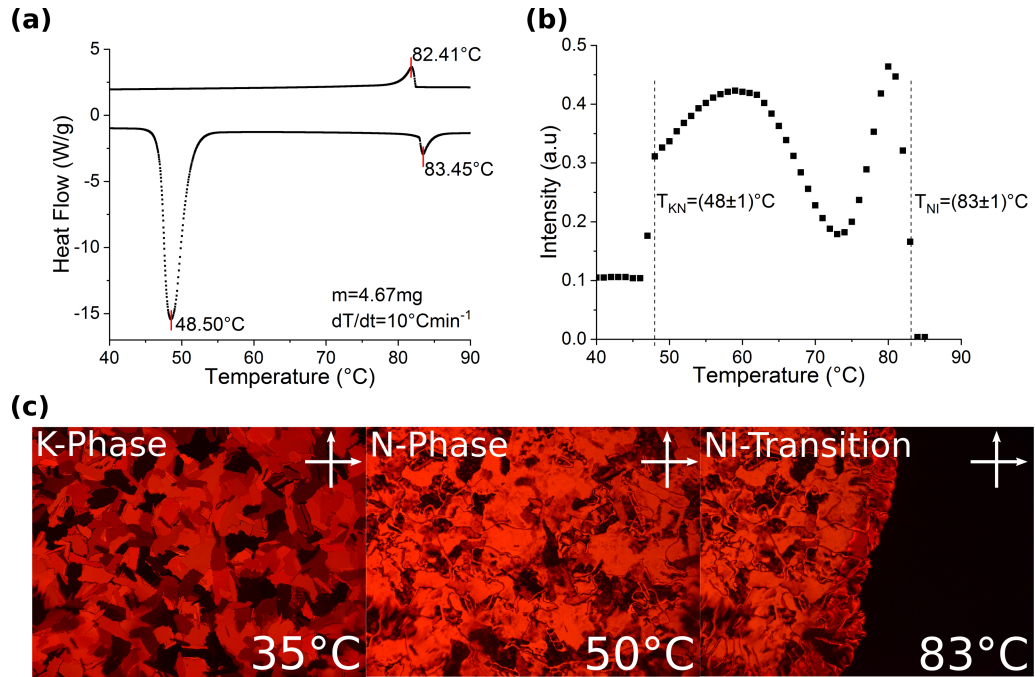


Figure 7.2: (a) The DSC data showing heat flow with respect to temperature for BAAB2 at a heat rate of 10°Cmin^{-1} . (b) The transmission of a red laser coupled to a POM setup through a randomly aligned planar BAAB2 sample. (c) POM images of a randomly aligned planar BAAB2 sample using a red filter to prevent photo-switching of the material.

To further corroborate the DSC transition temperatures the transmission of a red laser ($\lambda = 650\text{nm}$) through the POM setup was measured, shown in figure 7.2(b). The transmission of the laser through the randomly aligned planar BAAB2 sample was measured using a photodiode. This was conducted as a function of temperature using a Linkam hotstage (accuracy of $\pm 0.1^\circ\text{C}$), with the absolute accuracy of the transition temperature given as $\pm 1^\circ\text{C}$ due to the temperature gradient (clear in figure 7.2(c)) across the hot stage, as well as any calibration error. The phase transitions are clear by the sudden changes in transmission intensity. As the BAAB2 sample transitions from the crystalline to the nematic phase, $T = (48 \pm 1)^\circ\text{C}$, a sudden increase in intensity is observed, due to the reduction in scattering. The nematic to isotropic phase transition temperature is noted by the rapid drop in transmission at $T = (83 \pm 1)^\circ\text{C}$. In the

7. PHOTOISOMERISATION OF BAAB2

Experimental Technique	T_{KN} [$^{\circ}C$]	T_{NI} [$^{\circ}C$]	T_{IN} (cooling) [$^{\circ}C$]
DSC (<i>UnIrr</i>)	(48.5 ± 0.1)	(83.5 ± 0.1)	(82.4 ± 0.1)
POM (<i>red</i>)	<i>N/A</i>	(83.8 ± 0.1)	(83.4 ± 0.1)
POM (<i>red-laser</i>)	(48 ± 1)	(83 ± 1)	<i>N/A</i>
S. Watson [4]	48	83	<i>N/A</i>

Table 7.1: Table summarising the phase transition temperatures of pure un-irradiated BAAB2 measured via DSC, red-filtered POM, and red-laser POM transmission measured via photodiode.

isotropic state the birefringence is zero and therefore the transmission between crossed polarisers is zero. The transition temperatures measured here agree well with DSC phase transition temperatures measured.

With the phase diagram of pure un-irradiated BAAB2 confirmed through multiple experimental techniques, phase transition temperatures summarised in table 7.1, it is now crucial to characterise BAAB2’s absorptive properties in relation to its $\pi - \pi^*$ and $n - \pi^*$ transitions (excitation of *trans* and *cis* conformers).

7.1.2 BAAB2 absorption

The absorption properties of BAAB2 were established by measuring the absorption spectrum of BAAB2 in acetone (normalised to pure acetone) in a quartz cuvette using an Agilent UV/Vis 6000 spectrometer. The absorption spectrum ($\lambda = 200 - 800nm$) of BAAB2 is shown in figure 7.3 and demonstrates two distinct absorption peaks corresponding to the excitation of the *trans* and *cis* conformers.

In the *trans* state the BAAB2 molecule absorbs light at a peak wavelength of $\lambda = (350 \pm 1)nm$, which corresponds to the $\pi - \pi^*$ transition. Irradiation of BAAB2 with light of around 350nm will cause excitation of the *trans* conformers (discussed in chapter 3.2) causing an overall increase in *cis* population. In the *cis* conformal state the BAAB2 molecule absorbs light with a peak wavelength

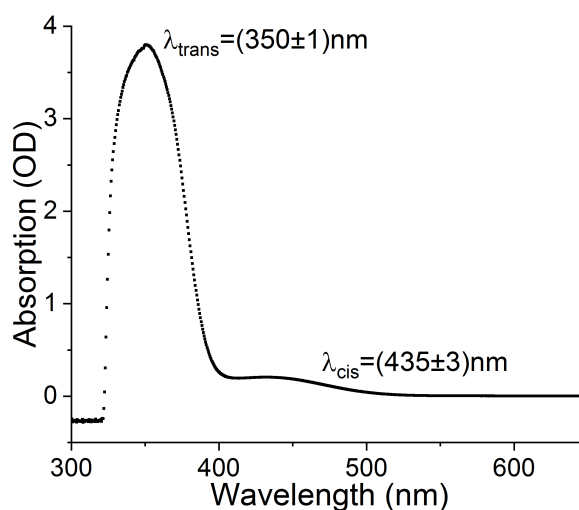


Figure 7.3: The absorption spectrum of BAAB2 dissolved in acetone is shown. There are two distinct peaks in absorption, with $\lambda = (350 \pm 1) \text{ nm}$ corresponding to the $\pi - \pi^*$ transition for the *trans* excitation and $\lambda = (435 \pm 3) \text{ nm}$ corresponds to the $n - \pi^*$ transition for *cis* excitation.

at $\lambda = (435 \pm 3) \text{ nm}$ which corresponds to the $n - \pi^*$ excitation of the molecule. Irradiation of BAAB2 with light of around 435nm will cause excitation of the *cis* conformers causing an overall increase in *trans* population.

It is important to emphasise that the absorption of light at these specified wavelengths ($A(\lambda)$) can be directly related to the concentration of the molecules in either the *trans* ($A(350\text{nm})$) or *cis* ($A(435\text{nm})$) conformational state simply through the Beer-Lambert law. The Beer-Lambert law directly relates the absorption at a specific wavelength to the wavelength-dependent absorption coefficient of a material ($\alpha(\lambda)$), material concentration (c), and cell gap (light path, d) (equation 7.1). BAAB2's physical properties are dependent on the relative concentrations of the conformers and therefore the ability to measure the concentration through the absorption at specified wavelengths will be utilised in later studies.

7. PHOTOISOMERISATION OF BAAB2

$$A(\lambda) = \alpha(\lambda)cd \quad (7.1)$$

7.1.3 Summary of BAAB2

In this section the baseline properties of BAAB2 azobenzene-based LC material have been established. The phase sequence in the un-irradiated state was measured directly via DSC and red-filtered POM, with a nematic phase present from $48 \rightarrow 83^\circ C$. The absorption properties were measured and each excitation mechanism was related directly to a peak absorption wavelength ($\lambda_{trans} = 350nm$ and $\lambda_{cis} = 435nm$).

Pure BAAB2 is incredibly photosensitive, with large changes in physical properties under low light intensities. Therefore, to allow for a more controllable photo-switch (to generate a switchable optical device discussed in chapter 10) a guest-host system was created and investigated. 5CB was doped with BAAB2 at varying concentrations to allow investigation into the effects of photoisomerisation on the phase and optical properties. Investigations into the underlying physics allows for insight into the photoisomerisation mechanism and comparison with theoretical predications allows for interesting conclusions on the theoretical assumptions and their validity.

The following investigation will be roughly split into two experimental stages. The first stage begins with 5CB doped with BAAB2 at varying concentrations. The irradiation of the material is conducted using a $\lambda = 405nm$ continuous wave laser and the effect of irradiation on the nematic to isotropic phase transition temperature is investigated as a function of BAAB2 concentration.

The second stage utilises a double-guest-host system with 5CB doped with BAAB2 at varying concentrations together with $0.5\%(\frac{w}{w})$ 15NB3OH (anthraquinone dye). The dopant 15NB3OH allows for a direct measurement of the order parameter of the system. The second technique also utilises optical spectrometer measurements which allows a direct measurement of the BAAB2 relative conformer population via absorption measurements. Irradiation of the system in

this experiment is achieved via a broadband UV light source and the impact of photoisomerisation on the nematic to isotropic phase transition temperature is investigated, however this time as a function of *cis* concentration. These experimental techniques are described in detail in chapter 4.2.

7.2 BAAB2 doped 5CB

The concentration of BAAB2 in 5CB was varied from 5 \rightarrow 10% ($\frac{w}{w}$) to investigate the effect of photoisomerisation on the nematic LC phase sequence.

7.2.1 Un-irradiated phase sequence

The baseline un-irradiated phase diagram must first be established and therefore DSC is conducted on the various BAAB2 doped samples. The transition temperatures ($UnIrr$) are summarised in table 7.2 and demonstrate an approximately linear increase in the nematic to isotropic phase transition temperature with increasing BAAB2 concentration in 5CB as seen in figure 7.4.

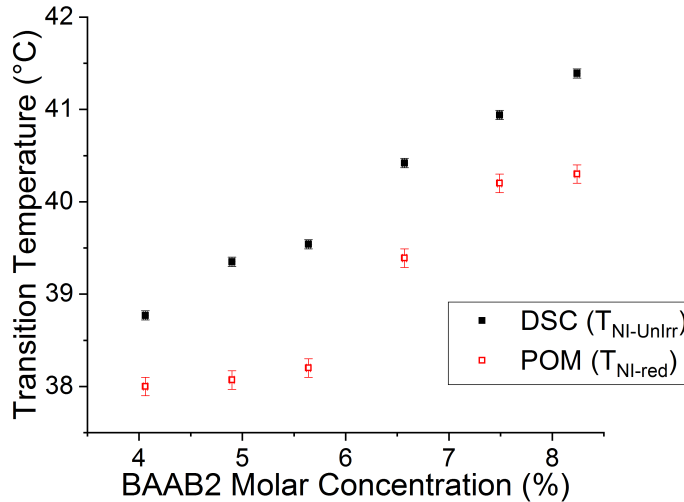


Figure 7.4: Un-irradiated nematic to isotropic phase transition temperatures for varying concentration of BAAB2 in 5CB. A comparison of two techniques DSC and red-filtered POM are shown. An increase in nematic to isotropic transition temperature is observed for increasing BAAB2 concentration in 5CB.

The increase in $T_{NI-UnIrr}$ is a result of the pure BAAB2 higher temperature nematic phase (48.5 \rightarrow 83.5°C) compared to 5CB (25.0 \rightarrow 36.3°C). This has

7.2 BAAB2 doped 5CB

Molar Concentration [%] (± 0.02)	T_{KN} [$^{\circ}C$]	T_{NI} [$^{\circ}C$]	T_{IN} [$^{\circ}C$]
0 [5CB]	(25.0 ± 0.1)	(36.3 ± 0.1)	(34.43 ± 0.05)
4.06	(17.7 ± 0.1)	(38.8 ± 0.1)	(36.8 ± 0.1)
4.90	(16.9 ± 0.5)	(39.4 ± 0.1)	(37.6 ± 0.1)
5.64	(16.8 ± 0.5)	(39.5 ± 0.1)	(37.8 ± 0.1)
6.57	(16.2 ± 0.1)	(40.4 ± 0.1)	(38.5 ± 0.1)
7.49	(15.1 ± 0.5)	(40.9 ± 0.1)	(39.4 ± 0.1)
8.24	(15.7 ± 0.1)	(41.4 ± 0.1)	(39.7 ± 0.1)
[BAAB2]	(48.5 ± 0.1)	(83.5 ± 0.1)	(82.4 ± 0.1)

Table 7.2: Table summarising the different BAAB2 concentrations in 5CB transition temperatures measured via DSC with a temperature scan rate of $10^{\circ}Cmin^{-1}$.

shown that doping of BAAB2 into 5CB simply results in a general increase to the nematic temperature range. In these measurements it is assumed that the BAAB2 *trans* concentration is equal to the total BAAB2 concentration due to the lack of light impacting the system. The lack of light means no photoisomerisation has occurred and the *cis* concentration is assumed to be zero ($c_{cis} = 0\%$), this is unlikely to be the case due to the energy landscape of the molecule leading to a probability of existing in either state, regardless of light-induced transformations or lack of. However, the observed approximately linear increase in $T_{NI-U_{nIrr}}$ with increasing total BAAB2 concentration indicates that it is a fair assumption that the *cis* concentration is close to zero. If photoisomerisation had occurred in the system the resultant *cis* concentration would have decreased the transition temperature with increasing concentration which is not observed.

The various concentrations of BAAB2 in 5CB were then filled into twisted nematic devices (SE3510 rubbed polyimide) with approximately $3\mu m$ cell gaps, described in chapter 4.5. The nematic to isotropic transition temperature was measured using POM with a red-filter to prevent photoisomerisation of the BAAB2 dopant (T_{NI-red}). The red-filter removes light of wavelengths less than $\lambda =$

7. PHOTOISOMERISATION OF BAAB2

580nm and therefore prevents photoisomerisation. The mixtures were heated on a hotstage at a rate of $2^{\circ}Cmin^{-1}$ and the phase transition temperatures were taken as the temperature at which transmission between crossed polarisers (measured via photodiode) reached zero. This method of transition temperature measurement was chosen due to the inability to monitor the sample by eye during laser irradiation.

Good agreement between the red-filtered POM and DSC measurements of the nematic to isotropic transition temperature (T_{NI-red} and $T_{NI-UnIrr}$) is observed in figure 7.4, although a systematic reduction in the transition temperature is observed for the POM measurement. This is likely a result of a high absolute error in the transition temperature measurement when comparing experimental techniques. The absolute error will result from the difference in calibration between techniques, the temperature gradient in the POM hotstage (typically around $0.2^{\circ}C$ across the stage), and also the POM phase transition temperature being chosen as the fully isotropic point. Overall, this will likely result in an absolute error of approximately $\pm 1^{\circ}C$. However by ensuring consistent experimental procedure is conducted using the POM hotstage method, with varying irradiation conditions, a direct comparison can be made between irradiation conditions with high levels of confidence.

7.2.2 Laser-irradiated phase sequence

With the un-irradiated phase sequence firmly established for all mixtures the effect of the photoisomerisation process on the nematic to isotropic transition temperature will now be investigated. The photoisomerisation of the BAAB2 dopant was triggered via exposure to a $0.5mW$ continuous wave laser ($\lambda = 405nm$). The laser was coupled into the POM setup via the reflection arm and the input laser polarisation was aligned with the upper substrate director to ensure maximum absorption. The laser wavelength of 405nm is on the edge of the BAAB2 *trans* excitation band (see figure 7.3). This means that the excitation of the *trans* conformer will be achieved, although it will be at a lower efficiency compared to

7.2 BAAB2 doped 5CB

Molar Concentration [%] (± 0.02)	DSC $T_{NI-UnIrr}$ [$^{\circ}C$] (± 0.1)	POM T_{NI-red} [$^{\circ}C$] (± 0.1)
4.06	38.8	38.0
4.90	39.4	38.1
5.64	39.5	38.2
6.57	40.4	39.4
7.49	40.9	40.2
8.24	41.4	40.3

Table 7.3: Table summarising the different BAAB2 in 5CB concentrations nematic to isotropic phase transition temperatures measured via DSC and red-filtered POM.

wavelengths much closer to the peak excitation wavelength of $\lambda_{trans} = 350nm$.

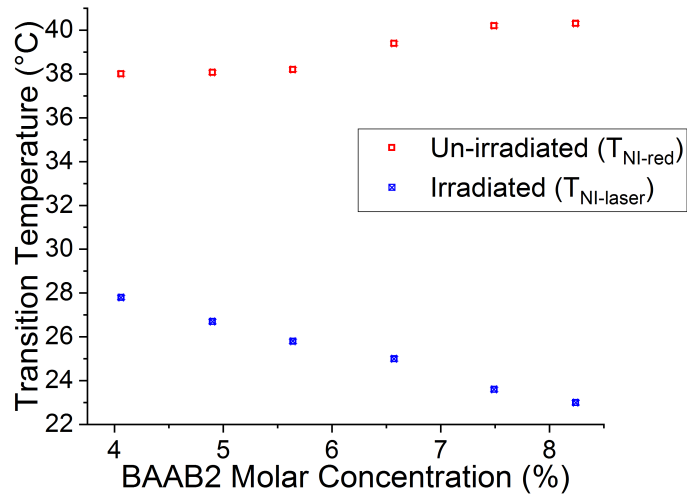


Figure 7.5: Comparison of un-irradiated and laser-irradiated nematic to isotropic transition temperature for varying BAAB2 dopant concentration in 5CB.

The change in the nematic to isotropic phase transition temperature due to

7. PHOTOISOMERISATION OF BAAB2

the laser-induced photoisomerisation ($T_{NI-laser}$) is shown in figure 7.5. A clear reduction in the phase transition temperature is observed for all BAAB2 concentrations. This is predicted by the light-induced order modification (LIOM) model (discussed in chapter 3.2.3) which states that the photoisomerisation of *trans* conformers into *cis* conformers will cause a LIOM due to the *cis* conformer being considered a light-induced impurity (LIM). The model also predicts that the order modification (transition temperature reduction) that occurs due to the photoisomerisation process will increase linearly with increasing *cis* concentration. While there is a clear increase in order reduction with increasing concentration ($T_{NI-laser}$ decreasing from 27.8 to 23.0°C between 5 and 10% ($\frac{w}{w}$)), fitting of equation 7.2 (discussed in chapter 3.2.3) is required to fully evaluate the dependency of transition temperature on *cis* concentration.

$$\frac{\Delta T_{NI}}{T_{NI}^0} = 2c' \frac{\sum_j \Delta v_{ij}}{\sum_j v_{ij}^0}. \quad (7.2)$$

If it is assumed that the laser irradiation causes photoisomerisation of all BAAB2 molecules in the mixture from *trans* to *cis* conformer the relative change in transition temperature (relative change between irradiated and un-irradiated measurement) can be plotted as a function of *cis* concentration. This assumption is chosen as no direct measurement of the *cis* concentration was conducted in this experimentation. This relationship can then be fit with equation 7.2 to find the relative change in intermolecular interaction energy (figure 7.6). In fitting the intercept is fixed at (0, 0) as a 0% concentration of *cis* isomers will result in no change in the phase transition temperature.

Figure 7.6 demonstrates variation of experimental data away from the fit of equation 7.2. The non-ideal fit is likely a result of the incorrect assumption that the entire mixture concentration of BAAB2 is photoisomerised into the *cis* conformer state by the $\lambda = 405nm$ laser. The low power of the laser and poor matching of laser wavelength to *trans* excitation peak is likely the reason not all of the BAAB2 is photoisomerised into the *cis* state and therefore the relative change in transition temperature measured does not correspond to the assumed

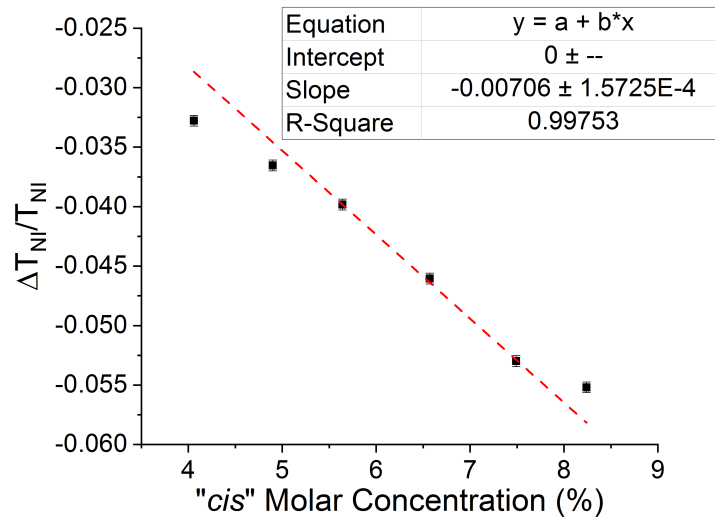


Figure 7.6: The relative change (in Kelvin) in the nematic to isotropic phase transition temperature plotted as a function of BAAB2 *cis* concentration. Fitted with equation 7.2 with intercept fixed at (0, 0).

cis concentration. This will be compared in later sections with UV-irradiation transition temperatures which demonstrate a larger relative reduction in transition temperature for the same total BAAB2 concentrations in 5CB indicating that not all the BAAB2 has been photoisomerised in the experiment here.

7.2.3 Summary of BAAB2 doped 5CB

In this section the un-irradiated phase transition temperatures of various concentrations of BAAB2 doped 5CB have been established via DSC and red-filtered POM showing a linear increase in the nematic to isotropic phase transition temperature with increasing BAAB2 concentration, going from $38.0 \rightarrow 40.3^\circ\text{C}$ between $5 \rightarrow 10\%(\frac{w}{w})$ BAAB2 concentration. This is a direct result of the higher temperature nematic phase of BAAB2 compared with 5CB.

Under continuous irradiation of a 405nm low-powered laser the photoisomerisation of the BAAB2 molecules into the *cis* state resulted in the expected re-

7. PHOTOISOMERISATION OF BAAB2

duction in nematic to isotropic phase transition temperature. However, fitting of equation 7.2 to experimental data revealed that the assumption that all BAAB2 dopant was photoisomerised via the laser irradiation was incorrect.

These results clearly demonstrate the impact of photoisomerisation on a nematic sample and the basic BAAB2 doped 5CB system will be utilised as a photo-switchable device described later in chapter 10. The conformational shape change from *trans* to *cis* causes an overall reduction in order lowering the transition temperature. These results provide good preliminary measurements, however there are experimental unknowns that require de-convolution if further insight into the fundamental physical mechanisms involved in the photoisomerisation process is to be achieved. These unknowns include:

- Population of *trans* and *cis* isomers in:
 - Steady-state
 - Irradiated state (is full switching from *trans* to *cis* achieved?)
- Phase transition temperature in terms of order (better phase transition identification)

To gain more insight into the photoisomerisation process new mixtures containing an additional anthraquinone dye guest were developed and the experimental technique was further expanded to allow direct measurement of the order parameter and *cis* concentration with varying temperature and irradiation conditions.

7.3 Photoisomerisation and order

In this section the new mixture and experimental procedure will first be introduced. The ability for the anthraquinone dye to directly measure the order parameter will then be demonstrated with a direct comparison to accepted literature values for the nematic 5CB. The absorption coefficient for the *cis* conformer will then be measured via optical spectroscopy of irradiated mixtures. The phase sequence dependence on total BAAB2 concentration will be established in the un-irradiated state via DSC. The phase sequence in the yellow-filtered state will then be investigated and the relationship between transition temperature and *cis* concentration will be established, followed by the dependence on the irradiated *cis* concentration achieved via **unpolarised** UV irradiation.

7.3.1 Method and materials

Mixtures between 0→10%($\frac{w}{w}$) of BAAB2 together with 0.5%($\frac{w}{w}$) 15NB3OH anthraquinone dye in 5CB were created and filled into homogeneous planar aligned (SE130 polyimide) LC cells with approximately 10 μ m cell gaps. The absorption spectrum for 15NB3OH is shown in figure 7.7 and demonstrates a clear peak in absorption at $\lambda = 694nm$. This anthraquinone dichroic dye was chosen as it is not azobenzene-based and has an absorption peak far away from BAAB2's absorption peaks (figure 7.3). Time-dependent density functional theory found the β angle between the TDM and the molecular long axis for 15NB3OH to be $\beta = 15.9^\circ$ [6].

Inclusion of the 15NB3OH anthraquinone dye into the BAAB2 doped 5CB mixture allows a direct measurement of the system order parameter from a simple optical measurement. By measuring the absorption at $\lambda = 694nm$ with the polarisation of light parallel and perpendicular to the bulk director the dichroic ratio can be calculated, $D = \frac{A_{\parallel}}{A_{\perp}}$. The dichroic ratio can then be used to calculate the order parameter (discussed previously in chapter 3.1.2) of the system via:

$$S_{LC} = \frac{D - 1}{D + 2} \frac{2}{3 \cos^2(\beta) - 1}. \quad (7.3)$$

7. PHOTOISOMERISATION OF BAAB2

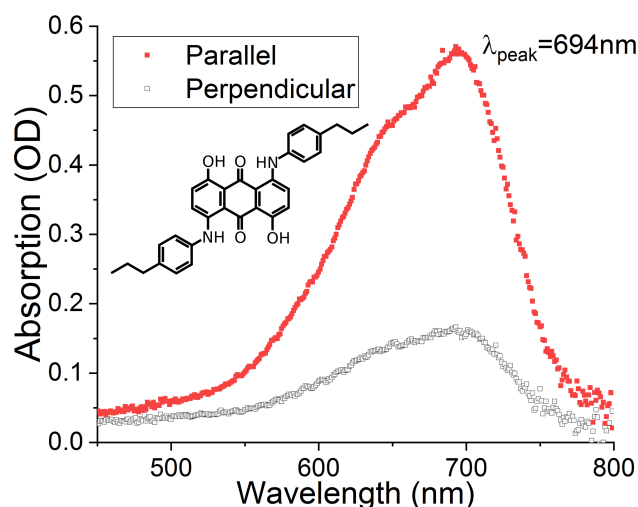


Figure 7.7: 15NB3OH absorption spectrum is shown with the input light polarisation parallel and perpendicular to the nematic host director. Peak absorption wavelength found at $\lambda = 694\text{nm}$.

Each sample was mounted in a single polariser optical microscopy setup with a yellow-filter to cut off light between 405 and 430nm, depicted in figure 7.8. The yellow-filter was implemented to attempt to reduce the amount of photoisomerisation triggered by the broadband visible light source whilst still allowing direct measurement of the *cis* population via the absorption at 450nm.

The transmission intensity was measured with the polarisation of light parallel and perpendicular to the director (normalised to a non-dye doped 5CB sample). The absorption at $\lambda = 694\text{nm}$ was measured to obtain the system order parameter via equation 7.3. Absorption at $\lambda = 450\text{nm}$ was measured to give a direct relation to the *cis* population, via the Beer-Lambert law (equation 7.1). These properties were all measured as a function of temperature, both with and without irradiation, to allow for a direct comparison of the nematic to isotropic phase transition temperatures. Photoisomerisation was triggered via irradiation of the sample with a broadband **unpolarised** UV light source from above. The UV

7.3 Photoisomerisation and order

light was reflected from a dichroic mirror, which reflects $\lambda < 400\text{nm}$ onto the sample and transmits $\lambda > 400\text{nm}$ through to the spectrometer. The use of the UV source coupled with a dichroic mirror resulted in higher intensity irradiation of the sample with intensities from $\lambda = 360 - 400\text{nm}$, much closer to the peak excitation of the *trans* BAAB2 molecule when compared to the continuous wave laser previously used.

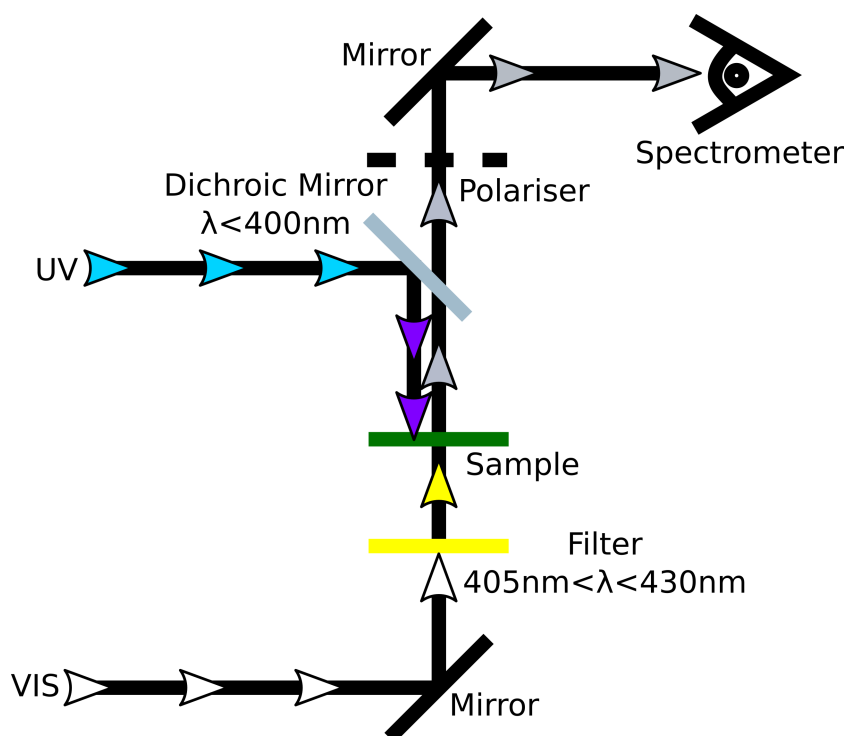


Figure 7.8: The experimental setup used to measure the optical properties of the samples whilst under UV irradiation is depicted.

The ability to directly measure the order parameter of the system, as well as the *cis* population, will allow for a much more rigorous investigation into the photoisomerisation process. Illumination using a high intensity **unpolarised** broadband UV source will also ensure that full photoisomerisation of the BAAB2 *trans* molecules is achieved.

7. PHOTOISOMERISATION OF BAAB2

7.3.2 Order parameter of 5CB

Firstly, to demonstrate the capability of the 15NB3OH dichroic dye absorption characteristics to be related to the order parameter of the system a measurement was conducted on 0.5% ($\frac{w}{w}$) 15NB3OH in 5CB and compared to the Haller method for order parameter calculation of 5CB [7], figure 7.9.

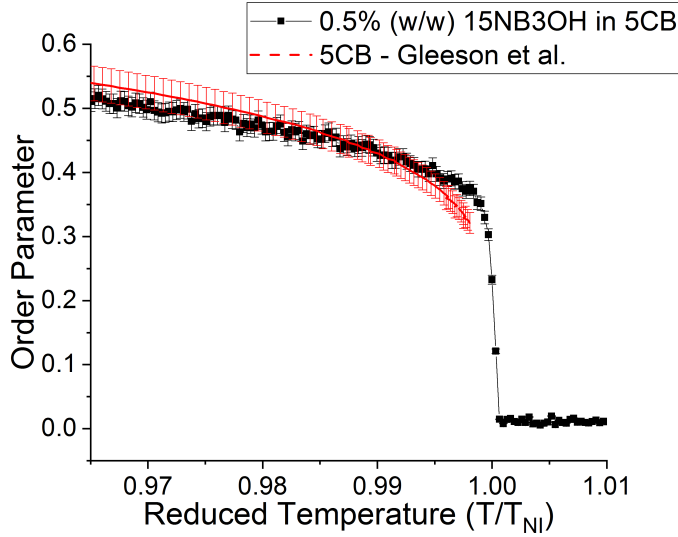


Figure 7.9: A comparison of the measured nematic order parameter for 0.5% 15NB3OH in 5CB (attained via the dichroic ratio) with published literature [7].

Agreement between the order parameter measured via the absorption characteristics of a dichroic dye doped into the nematic 5CB host and literature values for the order parameter of 5CB measured using the Haller method is shown. There is a variation between datasets close to the transition likely due to the absolute error in temperature when comparing different experimental techniques and difference in the definition of the nematic to isotropic phase transition temperature. Here, the phase transition temperature is taken as the point at which $S < 0.3$ which is chosen to ensure consistency between measurements and account for the unavoidable temperature gradient in the sample. The nematic to isotropic phase transition is a first-order transition, however, as seen in figure 7.9, a *continuous*

reduction in order parameter is observed in this experimental procedure due to the temperature gradient in the sample. Therefore the choice of $S < 0.3$ as the transition temperature point ensures consistency between experiments.

In comparing the temperature dependence of order parameter measured using the absorption method with literature Haller method shows good overlap between datasets when the error is included. The error in the order parameter measurement via the anthraquinone absorption is approximately 3%, estimated via the scatter of multiple experimental runs. This was chosen as the error propagation via the experimental accuracy will underestimate the error generated by difference in thermal contact and director alignment between experiments. There will also be changes to the sample characteristics generated by the addition of the 15NB3OH dye dopant to the 5CB host resulting in further discrepancies from literature values. This comparison has clearly shown that utilisation of the anthraquinone dichroic dye for measurement of the order parameter is a fair method, especially if consistency is maintained between all measurements, allowing for high levels of confidence when comparing samples.

7.3.3 Absorption coefficient of *cis* BAAB2

In order to fully understand the underlying physics occurring in the photochromic guest-host system it is crucial that any measurements can be directly related to the *cis* concentration in the sample (rather than just the total BAAB2 concentration as used in the previous section). As will be demonstrated, even in the non-UV irradiated state the *cis* population is not necessarily at 0% which subsequently impacts the physical properties observed.

The absorption of polarised light parallel and perpendicular to the director was measured at $\lambda = 450nm$ for varying concentrations of BAAB2 together with 0.5% ($\frac{w}{w}$) 15NB3OH in 5CB. The absorption values were measured whilst under continuous irradiation of **unpolarised** UV light. Here it is assumed that irradiation with the UV light source results in full photoisomerisation of the

7. PHOTOISOMERISATION OF BAAB2

BAAB2 into the *cis* conformal state, a more reasonable assumption now that a high-intensity broadband UV light source is employed. With this assumption the average absorption (equation 7.4) normalised with respect to the cell gap, $\frac{A_{avg}}{d}$, can be directly related to the *cis* concentration. The Beer-Lambert law, equation 7.1 can be fit to the data to calculate the absorption coefficient ($\alpha(450nm)$) for the *cis* conformer, as seen in figure 7.10.

$$A_{avg} = \frac{A_{\parallel} + 2A_{\perp}}{3}. \quad (7.4)$$

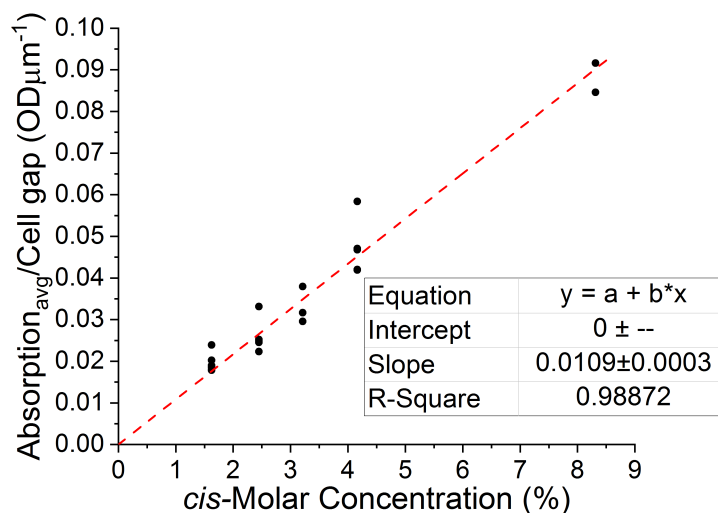


Figure 7.10: The average absorption at $\lambda = 450nm$ (normalised with respect to cell gap) is plotted as a function of BAAB2 *cis* molar concentration. These absorption measurements are taken during continuous UV irradiation of the BAAB2 doped samples and multiple repeats of the same concentrations are conducted. Fitting of the Beer-Lambert law is employed with the intercept fixed at (0, 0).

In fitting the Beer-Lambert law the intercept is fixed at (0, 0) as at 0% molar concentration the absorption will be 0OD. As can be seen from figure 7.10 the Beer-Lambert law gives a good fit indicating the assumption that all of the BAAB2 molecules are photoisomerised by the UV irradiation is correct. The fit gives an absorption coefficient of $\alpha(450nm) = (0.0109 \pm 0.0003)OD\mu m^{-1}\%^{-1}$.

This absorption coefficient can now be used to calculate the *cis* conformer population in any system given the average absorption measurement at 450nm and the device cell gap,

$$c = \frac{A(450nm)_{avg}}{d} \frac{1}{\alpha(450nm)}. \quad (7.5)$$

It is important to note that in the yellow-filtered state of the guest-host system the BAAB2 *cis* isomer has a polarisation angle dependant absorption at 450nm, shown in figure 7.11. This indicates that in the low-intensity yellow-filtered state the *cis* conformers that are present align in some manner with respect to the nematic director. The polarisation angle dependence decreases in the irradiated state (almost independent). This leads to some interesting conclusions surrounding the packing of these *cis* conformers and suggests that when non-UV irradiated they pack well with the nematic host and subsequently would not generate very much disruption to the nematic order. This will be revisited in the next section investigating the yellow-filtered order parameter. However, when irradiated they are more randomly aligned (polarisation angle independent absorption) potentially suggesting an increase to the *cis* conformer's disruption to the nematic order.

This polarisation angle dependency in absorption does however mean that in order to monitor the population of *cis* conformers between irradiation states it is necessary to calculate the average absorption as previously demonstrated.

7. PHOTOISOMERISATION OF BAAB2

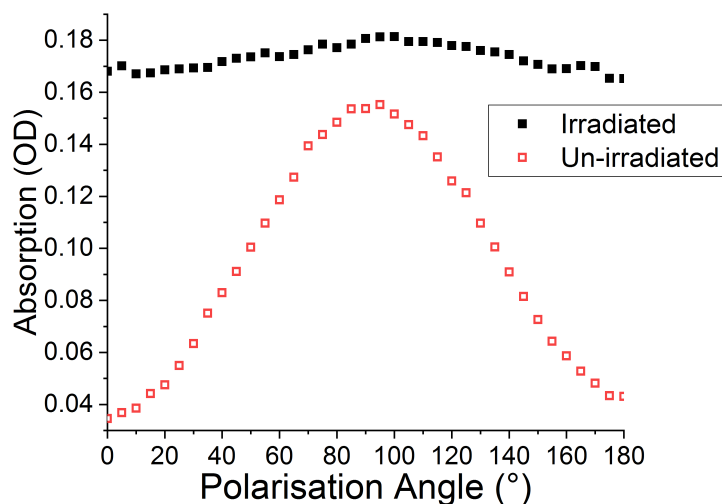


Figure 7.11: The polarisation angle dependence at $\lambda = 450\text{nm}$ of the guest-host 0.5% 15NB3OH + 2% ($\frac{w}{w}$) BAAB2 in 5CB system in the yellow-filtered and irradiated states. The molar concentration of *cis* conformers in the un-irradiated and irradiated states are measured to be 0.65% and 1.62%. The 450nm absorption corresponds to the BAAB2 *cis* conformer absorption.

7.3.4 Yellow-filtered order modification

The baseline measurement in the un-irradiated state must first be established for direct comparison with irradiated conditions to establish the impact of photoisomerisation. The first test is to again conduct a combination of DSC and POM to measure the un-irradiated transition temperature. In the POM a yellow-filter is utilised instead of a red-filter to allow direct measurement of the *cis* concentration. The red-filter removed all wavelengths below 580nm, whilst the yellow filter removes wavelengths between 405 and 430nm.

The DSC transition temperatures ($T_{NI-UnIrr}$) for varying BAAB2 concentration together with 0.5% ($\frac{w}{w}$) 15NB3OH in 5CB, compared directly to the non-15NB3OH doped samples from previous section 7.2.1, are shown in figure 7.12.

Excellent agreement between the 15NB3OH doped samples and the non-doped

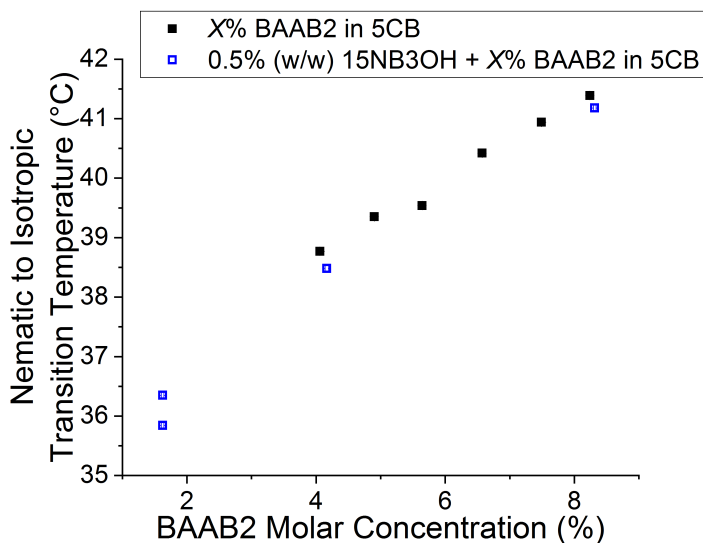


Figure 7.12: DSC transition temperatures are shown for varying BAAB2 concentration in 15NB3OH doped 5CB and non-15NB3OH doped 5CB. A general increase in transition temperature with increasing BAAB2 concentration is observed.

samples is seen, with a small variation of $\pm 0.5^\circ\text{C}$ between comparable concentrations. A linear increase in the transition temperature is again observed with increasing the total BAAB2 concentration and the small variation between samples is likely a result of the $0.5\%(\frac{w}{w})$ 15NB3OH dopant. It is important to note that here it is again assumed that the *cis* concentration is close to zero due to the light-tight pans employed in DSC. This assumption appears reasonable again due to the results demonstrating a linear increase in nematic to isotropic transition temperature with increasing concentration of BAAB2 in 5CB.

Now the order parameter will be measured as a function of temperature using POM, with a yellow-filter, to give insight into how the transition temperature ($T_{NI-yellow}$, taken as the point at which $S < 0.3$) varies as a direct function of *cis* concentration. The point at which $S < 0.3$ is chosen as the transition temperature to ensure consistency between measurements and account for the

7. PHOTOISOMERISATION OF BAAB2

unavoidable temperature gradient in the sample.

As previously noted in measurements of the polarisation angle dependence of the *cis* absorption (figure 7.11), when the system is in the yellow-filtered POM setup (no UV irradiation) the concentration of the BAAB2 molecules in the unrelaxed *cis* conformal state is not zero. According to the LIOM model any *cis* molecules can be simply considered as LIMs and will generate a change (reduction) in the intermolecular interaction energy. To investigate the effect of the yellow-filtered *cis* population on the system the order parameter is evaluated whilst simultaneously measuring the *cis* concentration via the 450nm absorption values.

The order parameter of the system is measured via absorption measurements at $\lambda = 694nm$ corresponding to the 15NB3OH anthraquinone dye. This allows a clear evaluation of the order of the system and also allows a quantitative measurement of the nematic to isotropic transition temperature. A comparison of the order parameter measured as a function of temperature for yellow-filtered 2%($\frac{w}{w}$) and 10%($\frac{w}{w}$) BAAB2 together with 0.5%($\frac{w}{w}$) 15NB3OH in 5CB is shown in figure 7.13. The absorption was measured at $\lambda = 450nm$ for the 2%($\frac{w}{w}$) and 10%($\frac{w}{w}$) BAAB2 doped samples and equation 7.5 gave the *cis* concentrations as $(0.91 \pm 0.03)\%$ and $(4.0 \pm 0.1)\%$ respectively.

Figure 7.13(a) demonstrates how an order reduction is induced with increasing concentration of *cis* conformers even without active UV irradiation of the system. An increase in *cis* concentration causes a shift in the order parameter curve to the left (lower temperatures), a direct result of the order parameter modification due to the reduction in the intermolecular interaction energy caused by the *cis* LIMs. By plotting the order parameter as a function of reduced temperature, figure 7.13(b), the two samples follow the same trend. This is expected as the order modification simply lowers the phase transition temperature and by normalising to this reduction the system will still follow the expected nematic behaviour.

7.3 Photoisomerisation and order

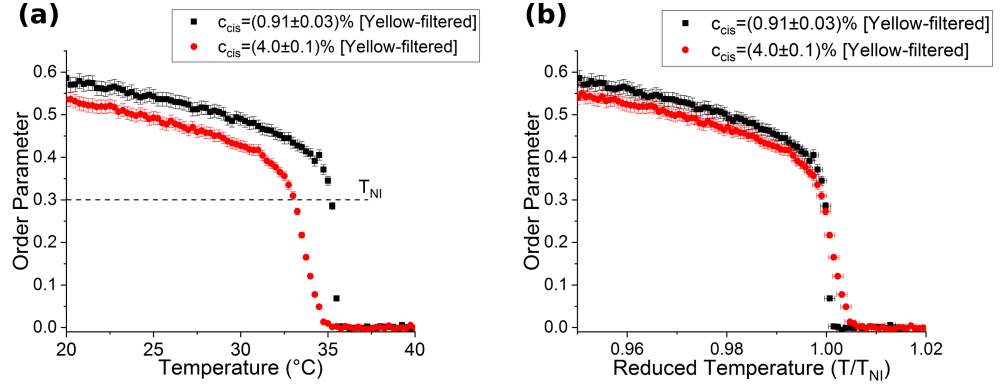


Figure 7.13: An example of the difference in the order parameter dependence on (a) temperature and (b) reduced temperature for two yellow-filtered mixtures of BAAB2 in 15NB3OH doped 5CB. The lower concentration mixture (2% ($\frac{w}{w}$) BAAB2) has a lower molar concentration of *cis* conformers (0.91%) whilst the higher concentration mixture (10% ($\frac{w}{w}$) BAAB2) has a higher steady state molar concentration of *cis* molecules (4.0%). This higher concentration of *cis* conformers results in a larger reduction in the order parameter curve. Plotting as a function of reduced temperature shows that the two systems follow similar nematic behaviour as expected.

To fully evaluate the impact of the *cis* concentration in the yellow-filter state the order parameter was measured as a function of temperature for a variety of *cis* concentrations. The yellow-filtered (no UV irradiation) state relationship between the nematic to isotropic phase transition temperature ($T_{NI-yellow}$) and *cis* concentration is demonstrated in figure 7.14(a).

The nematic to isotropic phase transition temperature ($T_{NI-yellow}$) is observed to decrease with increasing molar *cis* concentration in the yellow-filtered state. The reduction is small and there is a relatively large absolute error in the measurement using a hotstage due to difference in thermal contact and device alignment, estimated to be $\pm 1^\circ C$ from the scatter in the dataset. However, even with the associated error it can clearly be seen that the increasing *cis* population causes the expected reduction in the nematic to isotropic transition temperature due to

7. PHOTOISOMERISATION OF BAAB2

the order modification from the *cis* impurities.

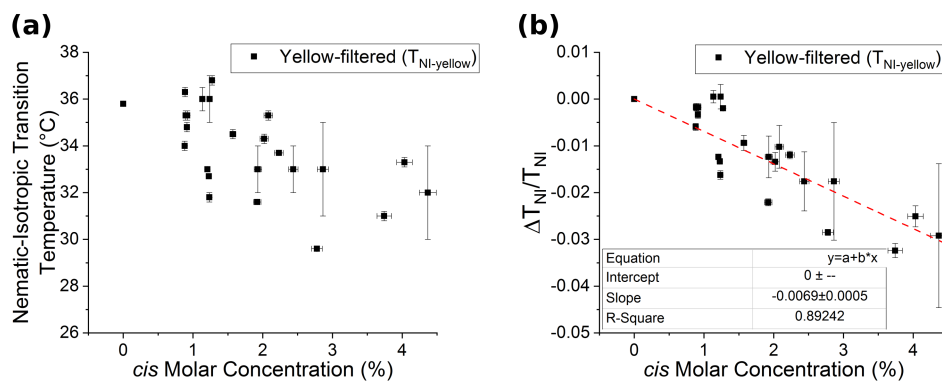


Figure 7.14: (a) Nematic to isotropic phase transition temperature as a function of *cis* concentration in the yellow-filtered state. (b) The relative change in the nematic to isotropic phase transition temperature as a function of *cis* concentration in the yellow-filtered state. Fitting of the LIOM model (equation 7.2) gives the relative change in interaction energy, intercept fixed at (0, 0).

These results seem somewhat counter to the previous DSC and red-filtered (un-irradiated) non-15NB3OH doped POM results, which demonstrate an overall increase in phase transition temperature with increasing total BAAB2 concentration. In these yellow-filtered measurement, utilising the order parameter, the samples with higher total BAAB2 concentration generally had a higher total measured *cis* concentration, meaning if compared with the previous DSC results of the same total BAAB2 concentration an opposite trend is observed. However, the reason for this discrepancy is in the experimental conditions themselves, rather than the experimental procedure. In DSC the samples are contained in a light-tight sample pan which prevents any ambient light from photoisomerising the BAAB2 dopant and therefore the assumption that the *cis* concentration is close to 0% is valid. Now the discrepancy between yellow-filtered and red-filtered POM (and DSC) results is easily explained when the transmission spectra of each filter employed is considered.

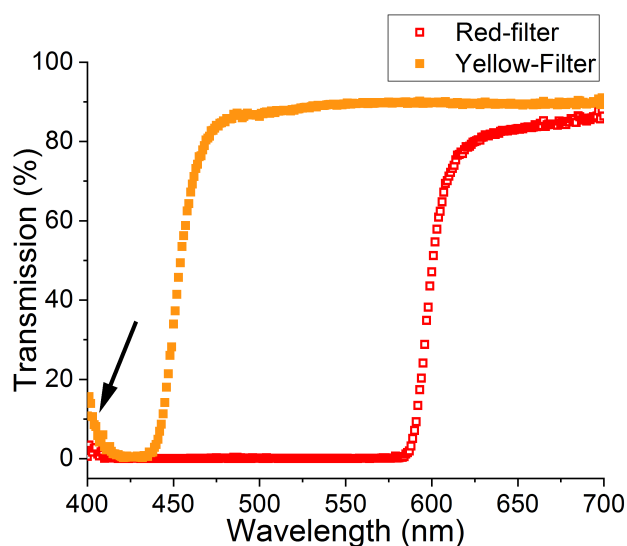


Figure 7.15: The transmission spectrum of the red-filter utilised in previous experimental results and the yellow-filter currently employed in experimental procedure is demonstrated. The small increase in transmission at low wavelengths for the yellow-filter is highlighted.

As can be seen from figure 7.15 the yellow-filter allows approximately 15% transmission at close to $\lambda = 400\text{nm}$. This small amount of light leakage will cause some photoisomerisation of the BAAB2 molecules and generate an increase in the *cis* concentration when compared with DSC and red-filtered experiments, although the levels will be low as the broadband visible bulb has low intensities in this wavelength regime. This is the reason behind the discrepancy between these yellow-filtered POM results and DSC/red-filtered POM even though there is no direct UV or laser irradiation of the sample. The use of the yellow-filter does however allow the advantage of direct measurement of the *cis* population via the 450nm absorption and therefore is the best possible experimental setup for deconvolution of the photoisomerisation process. The small amount of BAAB2 photoisomerisation into the *cis* state is directly monitored and allows for interesting conclusions to be drawn surrounding the physical packing of the *cis* conformer in this low-intensity photoisomerising condition. This comparison of DSC, red-

7. PHOTOISOMERISATION OF BAAB2

filtered POM, and yellow-filtered POM transition temperatures has demonstrated that the previous assumption that the red-filtered and DSC measurements prevented photoisomerisation is correct as a reduction in transition temperature with increasing BAAB2 concentration would have been observed if it were not the case.

Utilising the LIOM model the transition temperature dependence on *cis* concentration measured from the yellow-filtered POM can be replotted as the relative change in nematic to isotropic transition temperature $\frac{\Delta T_{NI}}{T_{NI}}$ (in Kelvin) versus *cis* concentration. The relative change in nematic to isotropic transition temperature is taken relative to the DSC measured phase transition temperature for each of the mixture as this is the closest to 0% *cis* conformer concentration. This will then allow fitting of equation 7.2 to establish the relative change in intermolecular interaction energy, figure 7.14(b).

The fitting of the LIOM equation indicates that in the yellow-filtered state the relative change in intermolecular interaction energy generated by the presence of *cis* conformers is $(-3.5 \pm 0.3) \cdot 10^{-3}$, which will be compared with later UV-irradiation results.

7.3.5 BAAB2 *cis* orientation

As previously demonstrated in figure 7.11 the *cis* conformer has a polarisation angle dependent absorption in the yellow-filtered (no UV irradiation) state. This polarisation angle dependence in absorption indicates an ordering of the *cis* molecule with respect to the nematic director, unexpected as *cis* molecules are typically assumed to be non-rod-like isotropic impurities in the system. Here the theory relating the nematic order parameter, dye order parameter, and transitional dipole moment (TDM) angle (discussed in chapter 3.1.2) will be utilised to establish the possible packing of the *cis* conformer in the yellow-filtered un-irradiated state.

The order parameter has been measured in the yellow-filtered state as a function of temperature via the absorption of the anthraquinone dye 15NB3OH via

equation 7.3. The angle the TDM makes with the 15NB3OH molecular long axis, β , is known from theoretical modelling. By measuring the dichroic ratio for the *cis* conformer (D_{cis}) at $\lambda = 450nm$ equation 7.3 can be rearranged to give the TDM angle for the *cis* molecule (β_{cis}). The *cis* conformer is clearly not a rod-like molecule so the TDM angle generated from this can be assumed to be the angle between the director and the TDM.

$$\beta_{cis} = \cos^{-1} \sqrt{\frac{1}{3} \left(\left[\left(\frac{D_{cis} - 1}{D_{cis} + 2} \right) \frac{2}{S_{LC}} \right] + 1 \right)} \quad (7.6)$$

By averaging across all yellow-filtered temperature dependant scans of various concentrations of BAAB2 together with 0.5%($\frac{w}{w}$) 15NB3OH in 5CB the average angle is found to be $\beta_{cis} = (26.6 \pm 0.5)^\circ$.

Previous literature exploring the angular dependence of azo-based material TDMs find that the fluctuation between possible *cis* conformers in the xy-plane results in an average TDM that is approximately along the N=N bond direction in the molecule [8]. If the calculated β value is used as the angle between the director and the N=N bond (TDM) it gives the possible packing demonstrated in figure 7.16. The 5CB dimerisation is shown and the possible packing of the *cis* molecules around the nematic host is demonstrated. The packing of the *cis* molecules at the suggested angle would agree with the current measurements which show a low amount of disruption to the order generated with increasing *cis* concentration in the yellow-filtered state.

Summary of order in low- or un-irradiated states

In this section new mixtures of BAAB2 containing 0.5%($\frac{w}{w}$) 15NB3OH in 5CB were introduced, along with the new method of measuring the temperature dependence of order parameter, whilst simultaneously monitoring the *cis* population. The absorption coefficient for the *cis* conformer was directly measured to be $\alpha(450nm) = (0.0109 \pm 0.0003)OD\mu m^{-1}\%^{-1}$, allowing real-time monitoring of

7. PHOTOISOMERISATION OF BAAB2

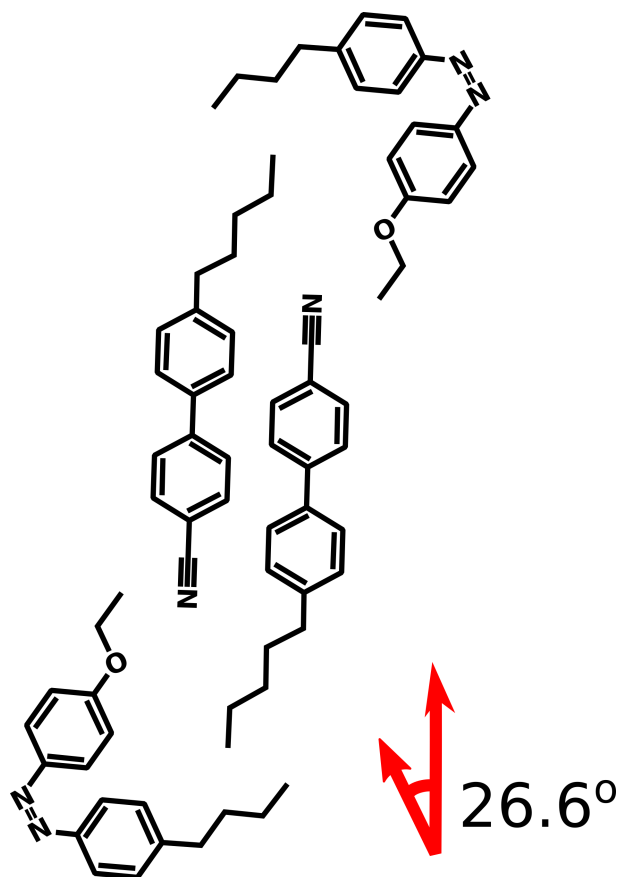


Figure 7.16: The possible packing of the *cis* molecule with nematic 5CB. The angle of the N=N bond is based on the calculated β value from the order parameter conversion.

the *cis* concentration via simple absorption measurements.

DSC was conducted on varying concentrations of BAAB2 together with 0.5% ($\frac{w}{w}$) 15NB3OH in 5CB and demonstrated a linear increase in the un-irradiated nematic to isotropic phase transition temperature ($T_{NI-UnIrr}$). This is in agreement with previous DSC measurements on the non-15NB3OH doped samples discussed in section 7.2.1.

The order parameter was then measured as a function of temperature using

7.3 Photoisomerisation and order

yellow-filtered POM, whilst also directly measuring the *cis* concentration via the absorption at 450nm. A decrease in the nematic to isotropic phase transition temperature ($T_{NI-yellow}$) was observed with increasing *cis* concentration, contrary to previous results. It was demonstrated that the yellow-filter resulted in low levels of photoisomerisation in the samples due to the transmission of light between 400 and 405nm. This resulted in a LIOM generating the observed lowering of the phase transition temperatures. This further corroborated the previous assumption that the DSC and red-filtered POM methods prevented photoisomerisation in the samples and has a resultant *cis* concentration close to 0%. Fitting of the LIOM model gave the relative change in intermolecular energy generated by the appearance of the *cis* molecules in the yellow-filtered state to be $(-3.5 \pm 0.3) \cdot 10^{-3}$.

The polarisation angle dependence of the *cis* absorption was related to the angle of the *cis* TDM ($\beta = (26.6 \pm 0.5)^\circ$). This allowed insight into the potential packing of the *cis* conformer when not under high-intensity irradiation and helps explain the low-levels of order modification generated.

To further investigate the physical effect of *cis* conformers and the photoisomerisation process irradiation of samples with an **unpolarised** broadband UV source will be conducted and the affect on order (transition temperature, T_{NI-UV}) will be established.

7. PHOTOISOMERISATION OF BAAB2

7.3.6 UV-irradiated order modification

Now that the physical impact of *cis* molecules in the yellow-filtered state has been established, the direct effect of UV photoisomerisation of the azobenzene-based BAAB2 on the 15NB3OH-doped 5CB host can be determined. The order parameter was again measured as a function of temperature to establish the nematic to isotropic phase transition temperature (T_{NI-UV}) as a function of *cis* concentration whilst under direct UV irradiation. An example of the order parameter versus temperature for yellow-filtered and irradiated 2%($\frac{w}{w}$) BAAB2 + 0.5%($\frac{w}{w}$)15NB3OH in 5CB (molar *cis* concentration of 0.91% and 1.62% respectively), and yellow-filtered 10%($\frac{w}{w}$) BAAB2 + 0.5%($\frac{w}{w}$) 15NB3OH in 5CB (measured molar *cis* concentration of 4.0%) is shown in figure 7.17.

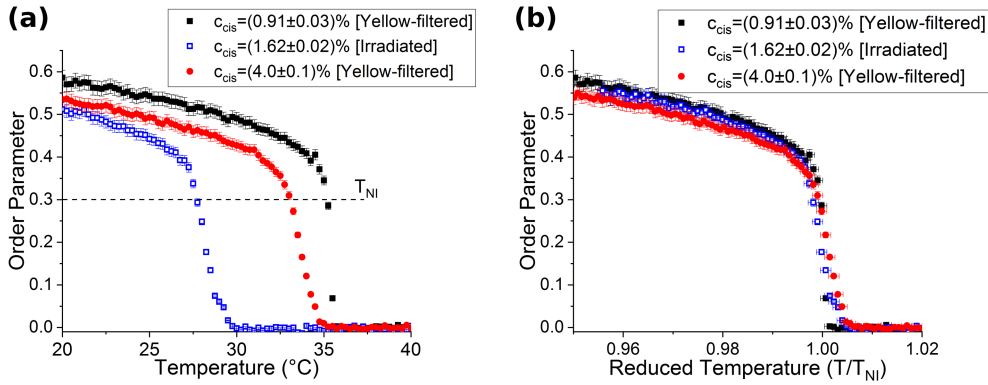


Figure 7.17: The order parameter versus (a) temperature and (b) reduced temperature for different *cis* concentrations in both yellow-filtered and irradiated states. The irradiated state increase in *cis* conformer shows a much larger change in order parameter compared to the increase in yellow-filtered increase in *cis* conformer concentration. It is shown that plotting as a function of reduced temperature results in each sample following the same trend as expected.

It can immediately be seen that the UV-induced photoisomerisation process causes a large decrease in the order parameter of the system, which appears dramatic when compared to the order reduction generated by the increased concentration in the yellow-filtered states. If the reduction in the nematic to isotropic

7.3 Photoisomerisation and order

Molar Concentration [%]	Irradiation state	ΔT_{NI} ($^{\circ}C$) [± 0.1]
(0.91 ± 0.03)	Yellow-filtered	-0.5
(4.0 ± 0.1)	Yellow-filtered	-7.9
(1.62 ± 0.02)	UV Irradiated	-7.5

Table 7.4: Table showing an example of the reduction in nematic to isotropic phase transition temperature when compared with un-irradiated DSC measurements for various concentrations of *cis* conformer and varying illumination states.

phase transition temperature is simply considered for each case, compared to the samples DSC un-irradiated phase transition temperature (table 7.4), it can be seen that when UV irradiated the sample produces a similar reduction in nematic to isotropic phase transition temperature as a yellow-filtered sample with nearly 2.5 times the *cis* concentration. This discrepancy is counter to the LIOM model which simply predicts a linear relationship between order modification and *cis* concentration. The fact that these two drastically different concentrations have similar reductions in phase transition temperatures suggests that there is an additional physical mechanism generated by the high-intensity UV irradiation causing an additional increase in order modification.

To fully investigate the UV irradiated photoisomerisation process the nematic to isotropic transition temperature (T_{NI-UV} , $S < 0.3$) was investigated for varying *cis* concentration and is shown in figure 7.18(a).

As expected under irradiation the photoisomerisation process increases the *cis* concentration in the sample, disrupting the order, and reducing the nematic to isotropic transition temperature. The transition temperature decreases linearly with increasing *cis* concentration as predicted by the LIOM model. In comparing with the previous laser irradiated transition temperature ($T_{NI-laser}$) it is clear that full photoisomerisation was not achieved as noted by the much higher transition temperatures measured compared to the UV-irradiated transition tem-

7. PHOTOISOMERISATION OF BAAB2

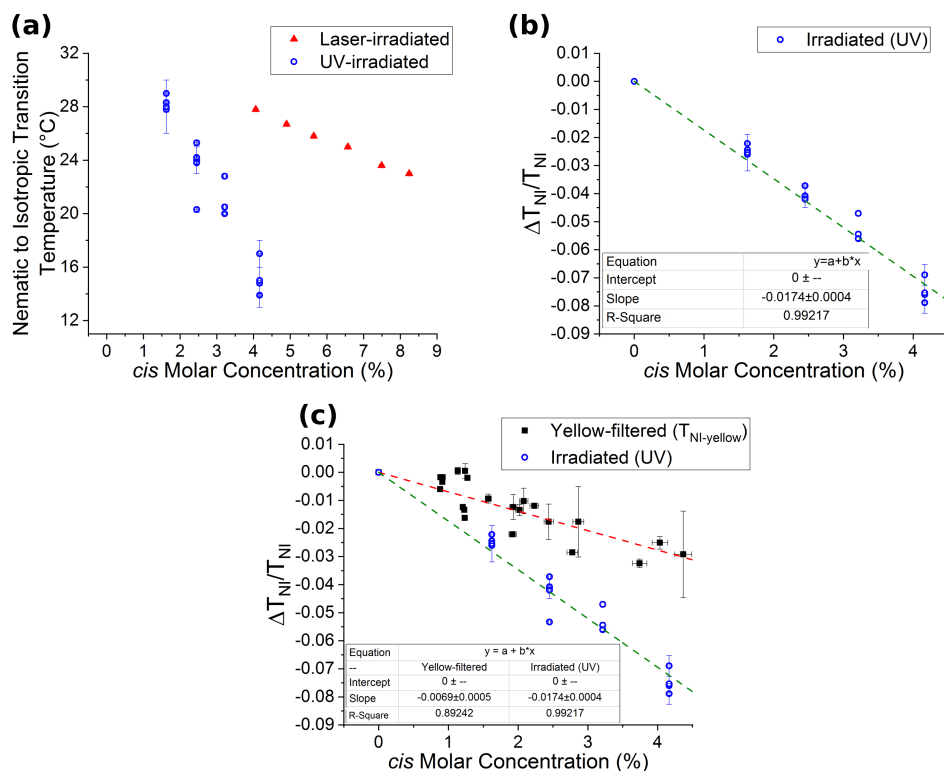


Figure 7.18: (a) The nematic to isotropic phase transition temperature (T_{NI-UV}) as a function of *cis* concentration for UV irradiated samples compared with previous laser irradiated phase transition temperature ($T_{NI-laser}$). The phase transition temperature decreases with increases *cis* concentration. (b) The relative change in phase transition temperature as a function of *cis* concentration. LIOM model is fit to establish the change in intermolecular interaction energy. (c) Comparison of irradiated and yellow-filtered relative change in phase transition temperature as a function of *cis* concentration, clearly highlighting the different dependencies.

peratures for comparable *cis* concentrations.

To calculate the change in intermolecular interaction energy, the relative change in phase transition temperature was plotted as a function of *cis* molecule concentration and fit with a linear equation, figure 7.18(b). The fitting of the

LIOM model with the intercept at $(0, 0)$ generates a much better fit than previous laser irradiation testing. The fitting results in a relative change in intermolecular interaction energy of $(-8.7 \pm 0.2) \cdot 10^{-3}$, a factor of more than 2 larger than the yellow-filter relative change in intermolecular energy of $(-3.5 \pm 0.3) \cdot 10^{-3}$.

Figure 7.5(c) clearly shows the difference between the yellow-filtered and UV irradiated effect of *cis* concentration on the nematic to isotropic phase transition temperature. The active photoisomerisation process generates a much larger modification of the system order parameter, generating a 2.5 times larger relative reduction in intermolecular interaction energy. The LIOM model, discussed in chapter 3.2.3, assumes that the order modification in an azobenzene-based nematic system is simply proportional to the LIM (*cis*) concentration. Here it has clearly been demonstrated that the order reduction (transition temperature modification) is dependant on more than just the *cis* concentration with an increased order modification generated by a secondary mechanism during **unpolarised** UV irradiation of the sample.

Summary of UV-irradiation

In this section the order parameter dependence on irradiated *cis* concentration was experimentally determined. The relationship between the nematic to isotropic phase transition temperature (T_{NI-UV}) and irradiated *cis* concentration was shown. The relative change in intermolecular interaction energy generated by the *cis* conformer was measured to be $(-8.7 \pm 0.2) \cdot 10^{-3}$, 2.5 times larger when compared with the yellow-filtered change in intermolecular interaction energy. This is indicative of a secondary physical mechanism generating a higher modification of the packing in the nematic system when **unpolarised** UV irradiation is employed.

7.4 Summary

The effect of doping calamitic LC 5CB with azobenzene-LC BAAB2 was investigated, with the impact on the phase sequence characterised in terms of *cis* conformer concentration and illumination conditions.

DSC found that the inclusion of BAAB2 into 5CB at concentrations of 5 \rightarrow 10% ($\frac{w}{w}$) caused an increase in the nematic to isotropic phase transition temperature from 36.5 \rightarrow 41.1°C. With no photoisomerisation occurring in the sample, due to the light-tight pans implemented in DSC, the BAAB2 *cis* concentration is close to 0% and therefore a linear increase in phase transition is observed due to the BAAB2 un-irradiated higher temperature range nematic phase when compared with 5CB.

The order parameter was measured as a function of temperature using yellow-filtered POM for various concentrations of BAAB2 together with 0.5% ($\frac{w}{w}$) 15NB3OH in 5CB. The *cis* concentration was monitored directly during experiments and the nematic to isotropic transition temperature was measured as a function of *cis* concentration.

In the yellow-filtered measurement the nematic to isotropic transition temperature was found to linearly decrease with increasing *cis* concentration, with a relative change in intermolecular interaction energy of $(-3.5 \pm 0.3) \cdot 10^{-3}$. The *cis* concentration was no longer 0% in the yellow-filtered condition due to the small amount of photoisomerisation caused by the 400-405nm low-intensity light leaking through the yellow-filter. The packing of the *cis* conformer into the system was also predicted utilising the combination of the absorption TDM with order parameter data.

Irradiation with **unpolarised** broadband UV light was utilised to trigger the photoisomerisation of BAAB2 and the order parameter was again measured as a function of temperature. The nematic to isotropic phase transition temperature was measured as a function of *cis* concentration in the irradiated state and again demonstrated a linear decrease with increasing concentration. The relative

change in intermolecular interaction energy was measured to be $(-8.7 \pm 0.2) \cdot 10^{-3}$, more than two times larger than in the yellow-filtered state.

At this point it is hypothesised that the order parameter modification in the UV irradiated, active photoisomerisation, state is a combination of the *cis* concentration causing a disruption to the packing (similar to the yellow-filtered state) plus a light induced torque exerted out of the plane on the system.

The experimental technique utilises **unpolarised** UV light irradiating the sample from above. As discussed in chapter 3.2.2 irradiation of an azobenzene-based material with polarised light causes a global reorientation of the molecule to be perpendicular to the irradiation polarisation. In this case **unpolarised** light is irradiating the system from above, resulting in an affinity for the molecules to orient out of the plane. Reorientation does not occur in these samples due to the strong anchoring conditions, however this affinity to reorient out of the plane will generate a light-induced torque on the nematic system. It is hypothesised that the light-induced torque is the cause of the increased order reduction when compared to the non-UV irradiated samples. To test this hypothesis, dielectric spectroscopy will be utilised in the next chapter as a probe to give insight into the physical properties and mechanisms occurring in this light-sensitive system.

References

- [1] P. V. Adomenas and V. A. Grozhik. . *Izv. AN BSSR, Ser. Chem.*, 36:N2, 1977. [91](#)
- [2] V. Grozhik, H. F. Gleeson, S. Serak, S. Watson, and A. Agashkov. Study of optical switching and reorientation in liquid crystals of homologous series of 4-n-butyl-4'-n-alkoxybenzenes. *Molecular Crystals and Liquid Crystals*, 320:433–444, 1998. [91](#)
- [3] U. Hrozhyk, S. Serak, N. Tabiryan, and T. J. Bunning. Wide temperature range azobenzene nematic and smectic LC materials. *Molecular Crystals and Liquid Crystals*, 454:235–245, 2006. [91](#)
- [4] S. J. Watson, H. F. Gleeson, A. D'emanuele, S. Serak, and V. Grozhik. A Study of Photochromic Azobenzene Liquid Crystals as Controlled Release Drug Delivery Systems. *Molecular Crystals and Liquid Crystals*, 331:375–382, 1999. [91](#), [92](#), [94](#)
- [5] S. V. Serak, E. O. Arikainen, H. F. Gleeson, V. A. Grozhik, J. P. Guillou, and N. A. Usova. Laser-induced concentric colour domains in a cholesteric liquid crystal mixture containing a nematic azobenzene dopant. *Liquid Crystals*, 29(1):19–26, 2002. [91](#)
- [6] M. T. Sims, L. C. Abbott, S. J. Cowling, J. W. Goodby, and J. N. Moore. Principal molecular axis and transition dipole moment orientations in liquid crystal systems: an assessment based on studies of guest anthraquinone dyes in a nematic host. *Physical Chemistry Chemical Physics*, 19:813–827, 2017. [105](#)
- [7] H. F. Gleeson, C. D. Southern, P. D. Brimicombe, J. W. Goodby, and V. Gortz. Optical measurements of orientational order in uniaxial and biaxial nematic liquid crystals. *Liquid Crystals*, 37:949–959, 2010. [xxii](#), [108](#)
- [8] T. S. Yankova, N. A. Chumakova, D. A. Pomogailo, and A. Kh. Vorobiev. Orientational order of guest molecules in aligned liquid crystal as measured by EPR and UV-vis techniques. *Liquid Crystals*, 40(8):1135–1145, 2013. [119](#)

Chapter 8

Photoisomerisation and physical properties

In the previous chapter BAAB2 doped 5CB was utilised in investigating the impact of the photoisomerisation process on the phase sequence of the nematic LC system. It was found that the presence of *cis* conformers generated a light-induced order modification (LIOM), reducing the nematic to isotropic phase transition temperature. It was found that UV irradiation generated a much larger relative change in the intermolecular interaction energy compared to similar *cis* concentrations generated by low-intensity yellow-filtered visible light. It was therefore hypothesised that the **unpolarised** UV light generates a light-induced torque on the nematic director generating an increased order modification in the system. This hypothesis will be tested in this chapter by utilising dielectrics as a probe into the light-sensitive system.

8.1 Dielectrics

Measurement of the deformation of the nematic director under an applied electric field (discussed in chapter 2.6) is an good method of establishing elastic and dielectric properties of a LC sample, as well as the pre-tilt of the alignment layer. In this section the measurement of the voltage dependence of capacitance, and subsequent fitting, will be utilised as a probe to establish whether a light-induced

8. PHOTOISOMERISATION AND PHYSICAL PROPERTIES

torque (external force) is exerted on the BAAB2 doped samples during irradiation with **unpolarised** UV. Measurement of the splay (k_{11}) and bend (k_{33}) elastic constants, the electrical permittivity parallel and perpendicular (ϵ_{\parallel} and ϵ_{\perp}), and the surface pre-tilt (θ_{tilt}) will be undertaken.

It is important to emphasise that any differences between irradiated and yellow-filtered samples of identical *cis* concentrations are not suggestions that they have fundamentally different physical properties, *cis* molecules in both states will have the same physical properties, but rather that any difference is indicative of an external force acting on the system which is unaccounted for in the fitting and subsequently manifests itself as a change in the physical parameters.

In this section the baseline physical properties will first be established for the non-BAAB2 doped sample. This will then be followed by measurements of the physical parameters of varying concentrations of BAAB2 together with 0.5% ($\frac{w}{w}$) 15NB3OH in 5CB for the yellow-filtered state and then the UV-irradiated state, giving insight into possible external forces acting on the material. The order parameter with respect to temperature is again measured via the 15NB3OH absorption and is established in all testing to give an accurate value for the nematic to isotropic phase transition temperature. The *cis* concentration is again measured via absorption values at 450nm, established in the previous chapter. All comparison of elastic/electric/pre-tilt parameters must be conducted as a function of reduced temperature ($\frac{T}{T_{NI}}$) to remove the impact of order modification. The LC mixtures are filled into low pre-tilt (1-2°, SE130 polyimide) uniform planar aligned ITO LC cells with 10 μ m cell gap. The capacitance was measured as a function of voltage from 0 \rightarrow 20 V_{rms} at a frequency of f=10kHz.

Later in this section the comparison of physical properties is represented by the relative change (e.g. $\frac{\Delta k_{ii}}{k_{ii}^0}$), which assuming an approximately 5% error in each value, as discussed in chapter 4.4, would result in a 7% error in the relative change. This however does not take into account error in the fitting of the temperature dependent empirical formulas. With this in mind all errors in the relative change in physical properties will be quoted with a 10% error to attempt

to give an accurate representation of the error in these results. Multiple runs were conducted across concentrations and irradiation conditions to give an accurate representation of the physical parameter dependencies measured in this light-sensitive system.

8.1.1 15NB3OH doped 5CB

Firstly, a baseline measurement must be established for direct comparison. This is achieved through dielectric measurements on 0.5% ($\frac{w}{w}$) 15NB3OH in 5CB (no BAAB2 dopant). Dielectric measurements were conducted on the sample, as well as pure 5CB, at a range of temperatures in the nematic region of the samples. An example graph of permittivity versus voltage is shown in figure 8.1 (a). Below the threshold voltage there is no change in permittivity, but once above the threshold voltage (approximately $0.7V_{rms}$) the director reorientation begins and a change in permittivity is measured. Fitting of equations (discussed in chapter 2.6) to the permittivity versus voltage curves, demonstrated in figure 8.1(a), gives splay and bend elastic constants, dielectric properties, and surface pre-tilt as a function of temperature for the material.

The temperature dependence of the elastic and dielectric properties were fit with empirical formulae (equation 8.1 and 8.2) to allow for a direct comparison between data sets, fitting procedure described in detail in [1]. It can be seen from the above results that there is very little change when introducing the anthraquinone dye 15NB3OH into 5CB nematic LC. There is a small reduction in the k_{33} elastic constant observed, but otherwise the material properties remain largely unchanged as expected from such a small concentration of dopant. The 0.5% 15NB3OH in 5CB results will be used as the baseline for comparison with BAAB2 doped samples to directly observe the impact of the BAAB2 material.

8. PHOTOISOMERISATION AND PHYSICAL PROPERTIES

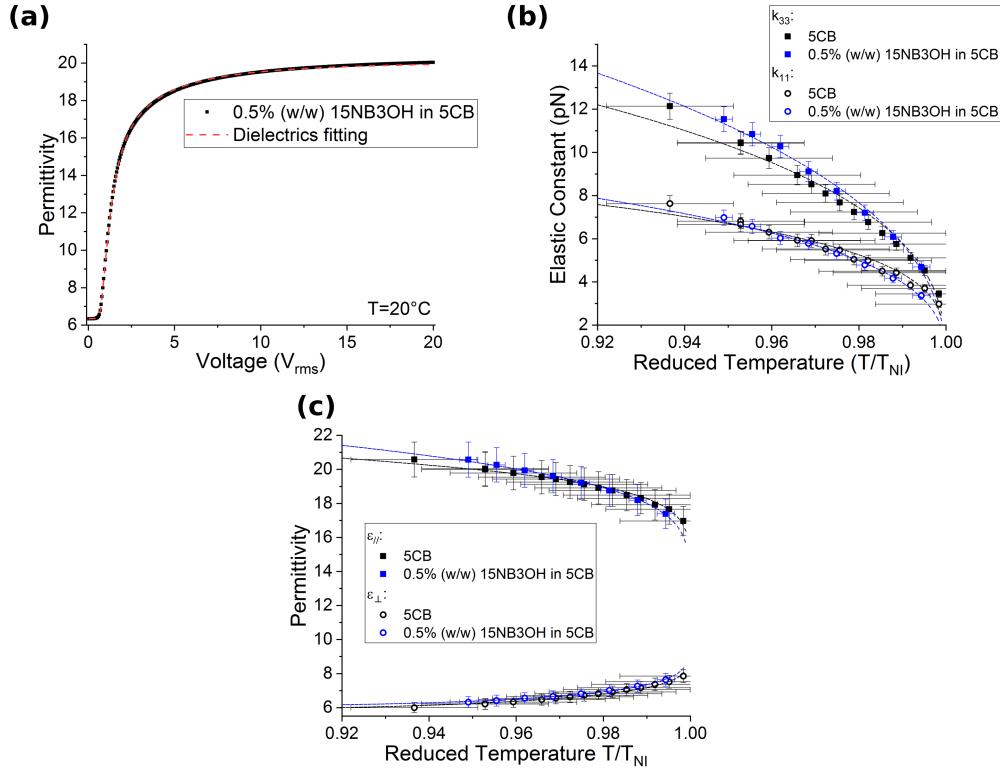


Figure 8.1: (a) The dependence of permittivity on voltage for 0.5% (w/w) 15NB3OH in 5CB, at a temperature of 20°C . The dielectrics fitting gave parameters of: $k_{11} = 6.98pN$, $k_{33} = 11.54pN$, $\epsilon_{\parallel} = 20.58$, $\epsilon_{\perp} = 6.32$, and $\theta_{tilt} = 2.15^\circ$. (b) A comparison of 5CB and 0.5% 15NB3OH in 5CB elastic constants temperature dependence. A slight reduction in k_{33} is observed. (c) A comparison of 5CB and 0.5% 15NB3OH in 5CB parallel and perpendicular electrical permittivity. Very little change is observed from such a small dopant concentration. (b, c) Empirical fitting of equations from [1]. Results are plotted as a function of reduced temperature to remove order parameter discrepancies.

$$\begin{aligned}\epsilon_e(T) &= \epsilon^* + A_\epsilon(T^* - T) + B_\epsilon(T^* - T)^{0.5} + \frac{2}{3}(\Delta\epsilon)_o\left(1 - \frac{T}{T_{NI}}\right)^{\lambda_\epsilon}, \\ \epsilon_o(T) &= \epsilon^* + A_\epsilon(T^* - T) + B_\epsilon(T^* - T)^{0.5} - \frac{1}{3}(\Delta\epsilon)_o\left(1 - \frac{T}{T_{NI}}\right)^{\lambda_\epsilon},\end{aligned}$$

$$\langle \epsilon(T) \rangle = \epsilon^* + A_\epsilon(T^* - T) + B_\epsilon(T^* - T)^{0.5}, \quad (8.1)$$

$$132 \quad \langle \epsilon \rangle = \frac{\epsilon_e + 2\epsilon_o}{3},$$

$$\Delta\epsilon = (\Delta\epsilon)_o\left(1 - \frac{T}{T_{NI}}\right)^{\lambda_\epsilon},$$

where T is temperature, ϵ_e is the extraordinary dielectric permittivity, ϵ_o is the ordinary dielectric permittivity, ϵ^* is the extrapolated dielectric permittivity at T^* which is the extrapolated temperature of the hypothetical continuous phase transition, A_ϵ is the static dielectric permittivity background term, B_ϵ is the dielectric amplitude, $(\Delta\epsilon)_o$ is the dielectric anisotropy in the crystalline state (obtained via extrapolation to $T = 0K$), T_{NI} is the nematic to isotropic phase transition temperature, λ_ϵ is a characteristic constant of the material which reflects the materials temperature dependence, and $\langle \epsilon \rangle$ is the average dielectric constant.

$$k_{ii}(T) = (k_{ii})_o \left(1 - \frac{T}{T_{NI}}\right)^{-\lambda_\epsilon}, \quad (8.2)$$

where k_{ii} is the elastic constant under consideration ($i=1$ or 3 in this investigation) and $(k_{ii})_o$ is the extrapolated elastic constant at $T = 0K$.

8.1.2 Yellow-filtered physical properties

Firstly, measurements for the yellow-filtered samples with varying BAAB2 concentration, again from $0 \rightarrow 10\%(\frac{w}{w})$, are conducted. Optical spectroscopy was used in tandem with the dielectric measurements to give accurate values of the nematic to isotropic transition temperature, as well as direct measurements of the *cis* population through absorption values at $\lambda = 450nm$.

The temperature dependence of each of the physical parameters was fit with the empirical formula described in [1] and the relative difference between the BAAB2 doped sample in question and the 0.5% 15NB3OH in 5CB sample (no BAAB2) was averaged between $\frac{T}{T_{NI}} = 0.95 \rightarrow 0.99$ to give an indication of the impact of the BAAB2. The relative change of each physical parameters dependence on *cis* concentration for the yellow-filtered samples will now be discussed in turn.

Elastic constants

The relative change in the splay and bend elastic constants, averaged over a temperature range of $\frac{T}{T_{NI}} = 0.95 \rightarrow 0.99$, dependence on the yellow-filtered BAAB2

8. PHOTOISOMERISATION AND PHYSICAL PROPERTIES

cis concentration is shown in figure 8.2. Figure 8.2(a) shows that for the majority of *cis* concentrations in the yellow-filtered state there is a slight increase in splay elastic constant. There doesn't appear to be any clear concentration dependence in the relative increase in k_{11} , with an average found to be $(4 \pm 2)\%$.

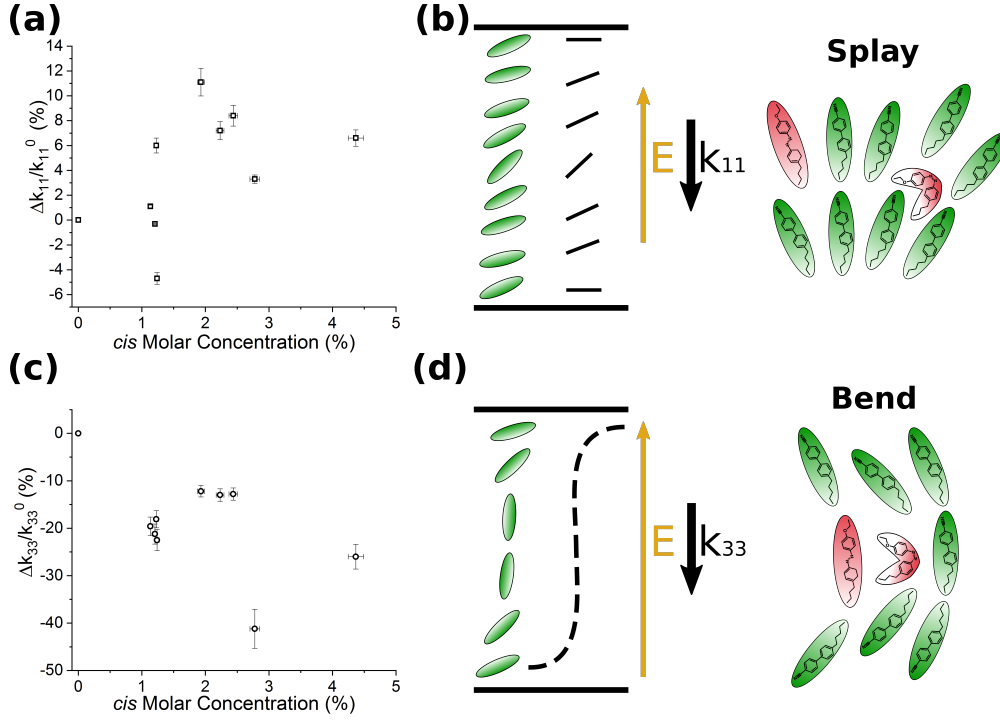


Figure 8.2: (a) The average relative change in splay elastic constant as a function of yellow-filtered *cis* concentration, averaged over $\frac{T}{T_{NI}} = 0.95 \rightarrow 0.99$. An average increase of $(4 \pm 2)\%$ is observed. (b) Depiction of the nematic director deformation occurring in the measurement of the splay elastic constant. The splay restoring force is demonstrated. Possible packing of the *cis* molecules into the splay packing is also shown. (c) The average relative change in the bend elastic constant is shown as a function of yellow-filtered *cis* concentration, averaged over $\frac{T}{T_{NI}} = 0.95 \rightarrow 0.99$. An overall decrease with increasing *cis* concentration is observed. (d) Depiction of the nematic director deformation occurring in the measurement of the bend elastic constant. The bend restoring force is demonstrated. Possible packing of the *cis* molecule into the bend packing is shown.

The splay elastic constant is calculated via the threshold voltage which occurs

in the low voltage regime. The director deformation occurring at this low voltage regime is demonstrated in figure 8.2(b). The possible impact of the BAAB2 dopant on the material can be inferred if the geometry of the molecules is simply considered.

In terms of the splay deformation it is sensible to assume the *trans* molecules will have little impact on the elastic constant (restoring forces generated), with the *trans* conformer shape being similar to the 5CB nematic host. The *cis* conformer however appear to potentially cause an increase in the elastic restoring force, although this is a very small effect with a large associated error. The packing of the V-shaped mesogen appears impractical in the splay director deformation, with the *cis* molecules bend angle being quite large, and means that it may potentially result in the observed increase in splay restoring force. However, previous literature has noted very little difference in splay elastic constant upon inclusion of a bent mesogen [2] into a nematic calamitic material.

The relative change in the bend elastic constant is shown in figure 8.2(c), showing an overall decrease in k_{33} with increasing *cis* conformer concentration. The BAAB2 dopant causes a relative decrease between 12 and 41% in the bend elastic constant. This is easily explained when the molecular geometry of the *cis* conformer is considered. The V-shaped molecule will clearly assist in the bend deformation, depicted in figure 8.2(d), reducing the restoring forces generated and therefore lowering the bend elastic constant measured. The reduction in bend elastic constant has been clearly observed upon including bent-core molecules in a calamitic nematic LC [2, 3].

Dielectric permittivity

The relative change in the parallel and perpendicular dielectric permittivity with relation to yellow-filtered BAAB2 *cis* concentration is shown in figure 8.3. Figure 8.3(a) shows that there is a small decrease in ϵ_{\parallel} with increasing *cis* concentration. Considering the molecular anisotropy of the *cis* isomer, figure 8.3(b), it becomes apparent that the *cis* isomer is likely to have a reduced dielectric anisotropy due

8. PHOTOISOMERISATION AND PHYSICAL PROPERTIES

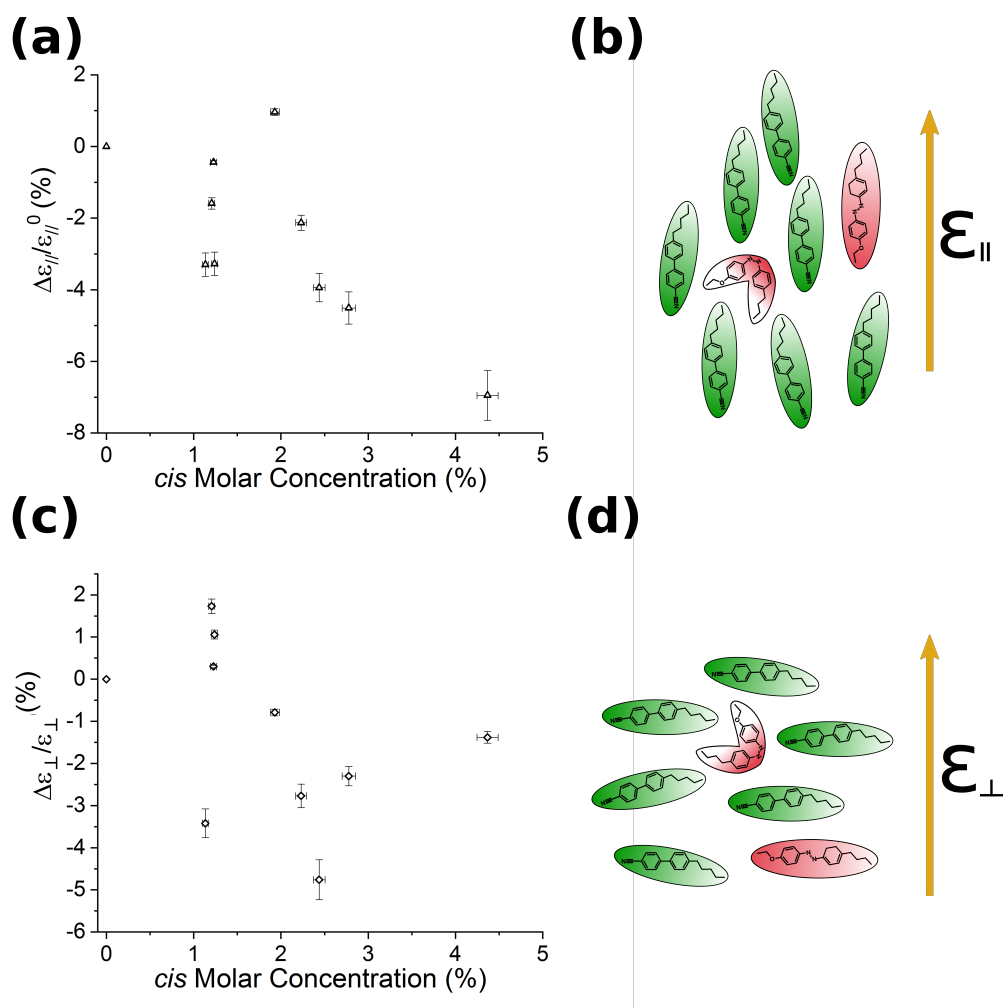


Figure 8.3: (a) The average relative change in parallel permittivity as a function of yellow-filtered *cis* concentration is shown, averaged over $\frac{T}{T_{NI}} = 0.95 \rightarrow 0.99$. A general decrease with increasing *cis* concentration is observed. (b) The relationship between the director and the measured parallel permittivity is depicted. The packing of the *cis* isomer into this configuration is shown to help draw conclusions on the observed trends. (c) The average relative change in perpendicular permittivity as a function of yellow-filtered *cis* concentration, averaged over $\frac{T}{T_{NI}} = 0.95 \rightarrow 0.99$. (d) The relationship between the director and the measured perpendicular permittivity is depicted. The packing of the *cis* molecule into this configuration is shown to help draw conclusions on the observed results.

to its less rod-like shape, therefore resulting in a reduced ϵ_{\parallel} as observed in the experimental data.

Figure 8.3(c) shows how ϵ_{\perp} changes with increasing *cis* population in the yellow-filtered state. There appears to be a slight decrease with increasing concentration, although the data is somewhat inconclusive. This indicates that there is potentially a reduction in the perpendicular electrical permittivity in the *cis* state conformer.

Overall there is very little change in the dielectric properties although a general decrease in dielectric anisotropy is observed for increasing *cis* concentration, figure 8.4, which is in agreement with observed dielectric anisotropy trends with during the inclusion of bent-core molecules in calamitic nematic materials [3]. These results will be compared with irradiated samples to give further insight into the photoisomerisation process.

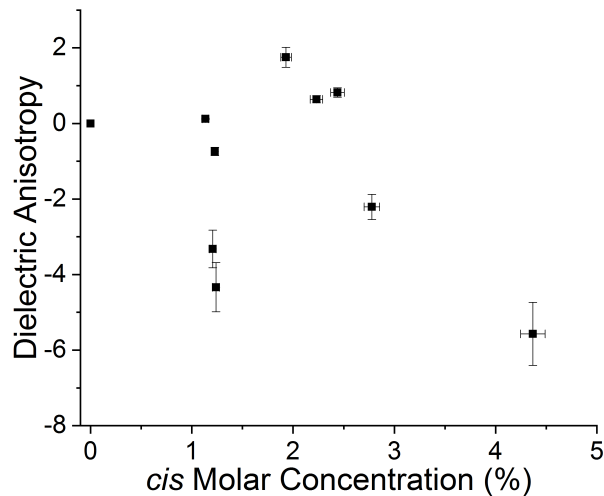


Figure 8.4: The average relative change in dielectric anisotropy as a function of yellow-filtered *cis* concentration is shown, averaged over $\frac{T}{T_{NI}} = 0.95 \rightarrow 0.99$. A general decrease with increasing *cis* concentration is observed.

8. PHOTOISOMERISATION AND PHYSICAL PROPERTIES

Pre-tilt

The fitting of the dielectrics data outputs the pre-tilt of the device substrates. The pre-tilt gives a measurement of the angle the director makes out of the plane at each surface, determined by the alignment substrate used. In the current testing polyimide surface alignment SE130 is used, with a quoted pre-tilt of 1-2°. Figure 8.5(a) shows how the pre-tilt varies with increasing *cis* concentration in the yellow-filtered state. Interestingly, the initial inclusion of BAAB2 into the system causes a decrease in pre-tilt angle from an average of 2° to approximately 0.5° for less than 1.5% *cis* concentration.

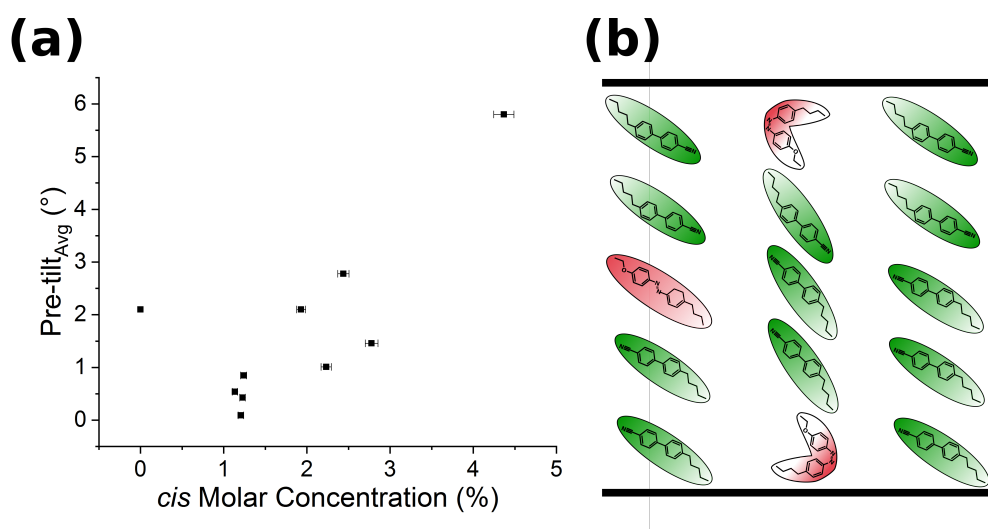


Figure 8.5: (a) The average pre-tilt dependence on the yellow-filtered *cis* concentration is shown, averaged over each samples full temperature dataset. After an initial decrease in pre-tilt with the addition of BAAB2 an increase in pre-tilt is observed with increasing *cis* concentration is observed. (b) A depiction of the pre-tilt in the devices measured. The impact of the V-shaped molecule on the director is shown to demonstrate how it could cause an increase in the pre-tilt measured in the device.

There is however a clear increase in average pre-tilt angle with increasing *cis* concentration from approximately 0.5 → 5.5°. This large increase in pre-tilt is

not a change in alignment layer, but rather a change of the molecular packing. Figure 8.5(b) depicts how the *cis* isomer could potentially change the measured pre-tilt of the system via its bend angle. The V-shaped molecule could cause an apparent increase in the pre-tilt due to the packing of the nematic around its bend angle.

The effect of the BAAB2 dopant on the physical parameters of the nematic LC system has been clearly established in the yellow-filtered state as a baseline. Now measurement under continuous UV irradiation can be conducted. Direct comparison with the yellow-filtered physical parameters will give a direct indication of the physical processes occurring in the system and the possibility of an external force acting on the system.

8. PHOTOISOMERISATION AND PHYSICAL PROPERTIES

8.1.3 UV-Irradiated physical properties

The voltage dependant capacitance was measured whilst simultaneously irradiating the sample with **unpolarised** UV light to investigate the impact of irradiation/photoisomerisation on the samples. It is important to again emphasise that any discrepancy between the yellow-filtered and irradiated samples at comparable concentrations of *cis* conformers does not indicate a change in molecular physical properties, but rather indicates the action of an additional external force on the system that is not accounted for in the fitting of experimental data. In this respect the dielectrics fitting is utilised as a probe into the underlying physical mechanisms occurring in the sample during irradiation. The relative change of each of the physical parameters will now be discussed in turn and compared with the previous yellow-filtered results.

Elastic constants

The relative change in the splay elastic constant with respect to *cis* concentration for irradiated BAAB2 samples is shown in figure 8.6(a). It can be seen that the splay elastic constant decreases with increasing *cis* concentration for the irradiated samples. This decrease is in direct contrast to the yellow-filtered sample which demonstrated a roughly concentration independent increase in k_{11} . Whilst there has been no change in the material this relative decrease in k_{11} can be explained if the possibility of an external optical torque (Υ_{opt}) acting on the system is considered, figure 8.6(b). The optical torque that could be generated due to the irradiation of **unpolarised** UV would act out of the plane. This force would act in the opposite direction to the splay restoring force thus resulting in a lower measurement of the splay elastic constant.

Similar results are observed in the measurements of the bend elastic constant, figure 8.6(c). A decrease in bend elastic constant is again observed with increasing *cis* concentration. The relative decrease is larger for the irradiated state when compared with similar concentrations of *cis* isomer in the yellow-filtered state. This again indicates an external force (optical torque) acting on the system when under continuous irradiation causing an *apparent* reduction in the bend elastic

constant.

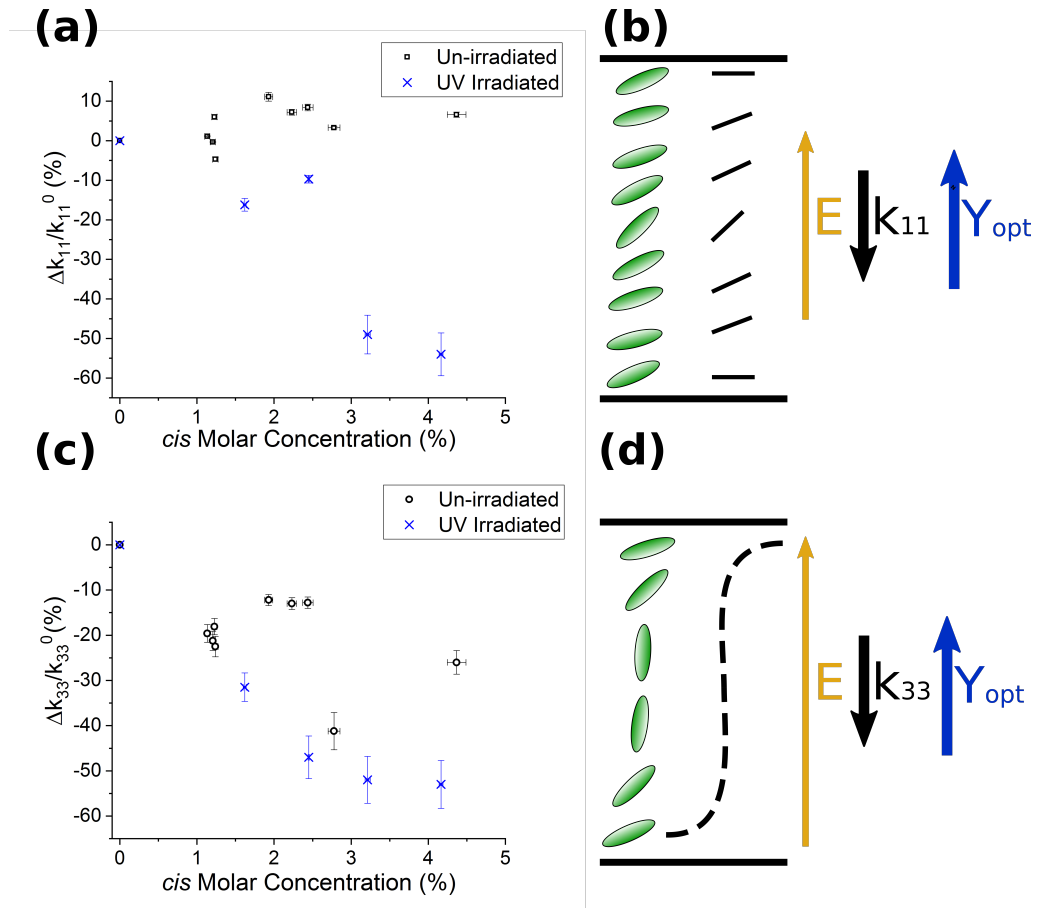


Figure 8.6: (a) The average relative change in splay elastic constant dependence on irradiated and yellow-filtered *cis* concentration is shown, averaged over $\frac{T}{T_{NI}} = 0.95 \rightarrow 0.99$. In the irradiated state an overall decrease with increasing *cis* concentration is observed. (b) The splay director deformation is shown with the possible forces acting on the system depicted. (c) The average relative change in bend elastic constant dependence on irradiated and yellow-filtered *cis* concentration is shown, averaged over $\frac{T}{T_{NI}} = 0.95 \rightarrow 0.99$. The irradiated state demonstrates a large decrease with increasing *cis* concentration. (d) The bend director deformation is shown with possible forces acting on the system depicted.

The reduction in both elastic constants when under continuous irradiation is

8. PHOTOISOMERISATION AND PHYSICAL PROPERTIES

indicative of an external force acting on the system. It is not a result of a change in material parameters as the material is directly compared to the yellow-filtered samples with similar *cis* concentrations. Therefore, the increased relative reduction in elastic constants indicates that there is an additional optical torque acting on the system out of the plane causing the *apparent* reduction in elastic physical parameters.

Dielectric permittivity

Measurement of the dielectric permittivity parallel and perpendicular whilst under continuous UV irradiation is shown in figure 8.7. It can be seen that ϵ_{\parallel} shows very little difference between the yellow-filtered and irradiated states of similar *cis* concentrations. This is in agreement with the hypothesis of an optical torque acting on the system. If the measurement of ϵ_{\parallel} is considered, figure 8.7(b), it is simply a measurement of the dielectric permittivity when the director is oriented out of the plane. An optical torque acting on the system would have little to no impact on the final out-of-plane state as the applied electric field and optical torque are acting in the same direction. For the highest irradiated *cis* concentration there is perhaps an increased reduction compared to yellow-filtered, however in general there appears to be little difference.

The measurement of perpendicular dielectric permittivity under irradiation shows an increase in ϵ_{\perp} with increasing *cis* concentration. This is opposite to the yellow-filtered state which demonstrated a small decrease with increasing concentration. This is again in agreement with the hypothesis of an optical torque acting on the system when the potential forces acting on the system are considered.

If an optical torque is acting on the system in the low voltage planar regime it will potentially generate a slight reorientation out of the plane. This would manifest itself as an increase in the measured perpendicular permittivity, demonstrated in figure 8.6(d), as the director is rotated towards the out of plane state (ϵ_{\parallel}) which has a higher permittivity, and therefore this observed increase in ϵ_{\perp} is indicative of an optical torque acting on the system.

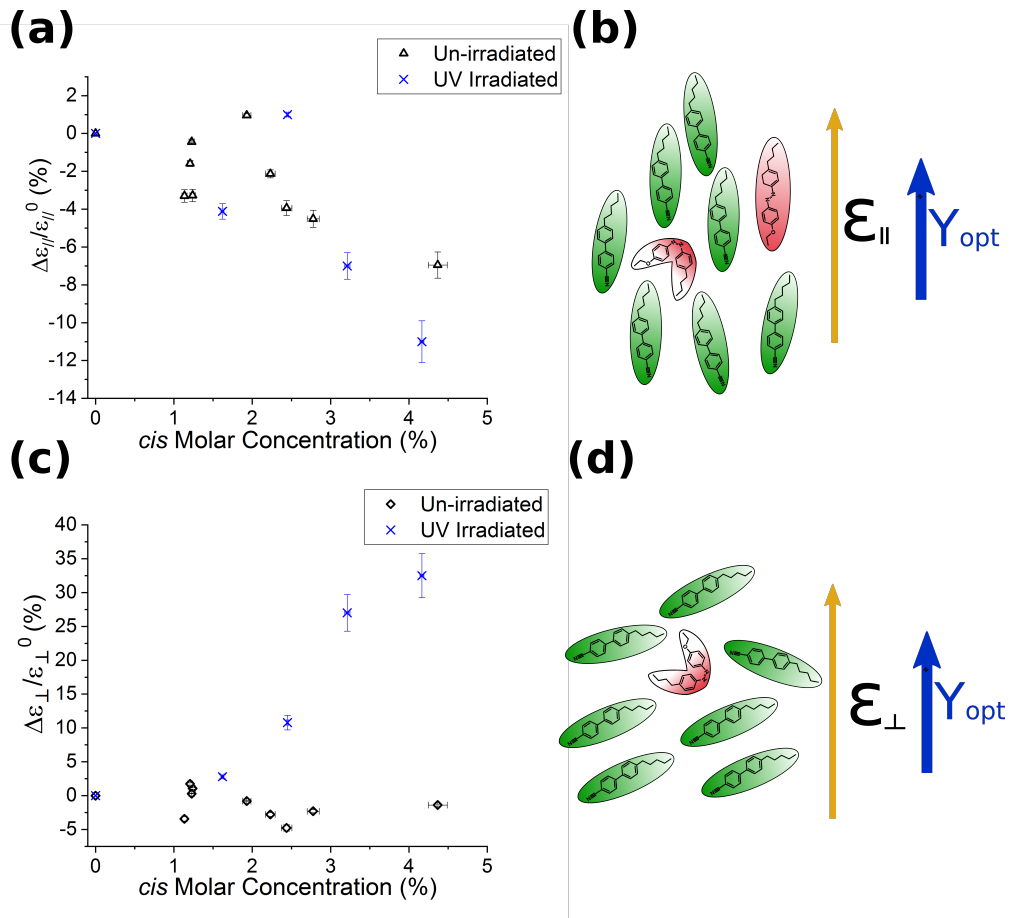


Figure 8.7: (a) The average relative change in parallel permittivity as a function of irradiated and yellow-filtered *cis* concentration, averaged over $\frac{T}{T_{NI}} = 0.95 \rightarrow 0.99$. (b) Depiction of the parallel permittivity measurement with the hypothesised optical torque force direction shown. (c) The average relative change in perpendicular permittivity as a function of irradiated and yellow-filtered *cis* concentration, averaged over $\frac{T}{T_{NI}} = 0.95 \rightarrow 0.99$. An increase is observed with increasing irradiated *cis* concentration. (d) Depiction of the perpendicular permittivity measurement is shown. The impact of an optical torque force acting on the system is shown in the slight reorientation of the director.

Pre-tilt

Finally, the average pre-tilt is observed to increase with increasing concentration of *cis* molecules whilst under continuous irradiation, figure 8.8(a), when compared

8. PHOTOISOMERISATION AND PHYSICAL PROPERTIES

with the yellow-filtered similar *cis* concentrations. This is similar to the measurement of the perpendicular dielectric permittivity in that the optical torque acting on the system will cause a slight re-orientation out of the plane. Figure 8.8(b) depicts how this effect could manifest itself in a higher measured pre-tilt angle in the dielectrics fitting.

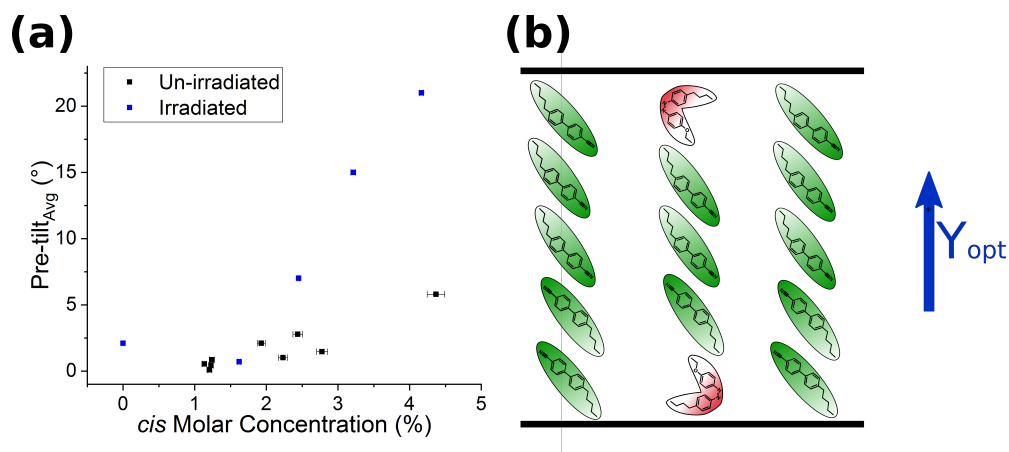


Figure 8.8: (a) The average pre-tilt as a function of irradiated and yellow-filtered *cis* concentration, measured over the full temperature range of each dataset. The irradiated state shows an increase in pre-tilt with increasing *cis* concentration. (b) Depiction of the pre-tilt measurement is shown with the effect of an optical torque acting on the system demonstrated by an increase in the director reorientation.

In previous literature the absorption of methyl-red azobenzene material onto the alignment layer has been suggested in a LC guest-host system when under UV irradiation [4], causing a change to the alignment conditions utilised as a form of photo-patterning. Here it is acknowledged that such a mechanism may be occurring in the BAAB2 doped 5CB system, causing the observed change in pre-tilt, although this is hard to conclude on and further experimentation is required to test if this is occurring.

8.2 Summary

In this chapter the fitting of the voltage dependence of capacitance has been utilised as an investigative tool into the physical mechanisms occurring during the photoisomerisation process. A direct comparison of the relative change in physical parameters measured (elastic constants, dielectric properties, and device pre-tilt) between continuously UV irradiated and yellow-filtered samples was undertaken. The difference between yellow-filtered and irradiated physical parameters agreed well with the hypothesis of an external force acting on the system during irradiation. This light-induced torque generated measurements of lower elastic constants due to the optical torque opposing the elastic restoring force. An increased perpendicular permittivity and pre-tilt for comparable *cis* concentrations was observed in comparing irradiated and yellow-filtered samples, again indicative of an optical torque acting out of the plane.

These results imply that there is an external force acting out of the plane of the system accounted for here if an optical torque, due to the selective excitation of the photoisomerisation process, is considered. These results have demonstrated that in considering the LIOM generated by the photoisomerisation of azo-based compounds more than the *cis* concentration must be considered for accurate predictions of the order modification.

In the next chapter the time-dependence of the photoisomerisation process will be investigated to give insight into photoisomerisation and relaxation rates, as well as the impact of the yellow-filtered visible light on the system itself.

References

- [1] A. Ranjkesh, M. Moghadam, J-C. Choi, B. Kim, JH. Ko, M. S. Zakerhamidi, and H-R. Kim. Physical model for temperature-dependent dielectric properties of anisotropic nematic liquid crystals. *Physical Chemistry Chemical Physics*, 20:19294–19306, 2018. [xxiv](#), [131](#), [132](#), [133](#)
- [2] P. Sathyanarayana, B. K. Sadashiva, and S. Dhara. Splay-bend elasticity and rotational viscosity of liquid crystal mixtures of rod-like and bent-core molecules. *Soft Matter*, 7:8556–8560, 2011. [135](#)
- [3] M. R. Dodge, C. Rosenblatt, and R. G. Petschek. Bend elasticity of mixtures of V-shaped molecules in ordinary nematogens. *Physical Review E*, 62(4):5056–5063, 2000. [135](#), [137](#)
- [4] T-H. Lin, Y. Huang, A. Y. G. Fuh, and S-T. Wu. Polarization controllable Fresnel lens using dye-doped liquid crystals. *Optics Express*, 14(6):2359–2364, 2006. [144](#)

Chapter 9

Time-dependence of photoisomerisation

The time dependence of the photoisomerisation process is important to quantify as it will impact the operation of the system in applications and also monitoring the system during the photoisomerisation process will give further insight into the process, as well as information about the impact of lighting conditions.

9.1 Time-dependent optical properties

In this section the optical properties of 2%($\frac{w}{w}$) BAAB2 together with 0.5%($\frac{w}{w}$) 15NB3OH in 5CB are monitored as a function of time to measure the *cis* population via the absorption at $\lambda = 450nm$, as well as the order parameter as a function of time via the 15NB3OH polarisation dependent absorption at $\lambda = 694nm$. Photoisomerisation is triggered via UV irradiation at time $t=5s$ and the relaxation process is also monitored upon removal of UV irradiation at time $t=60s$. These time-dependant parameters are measured at a variety of temperatures ($22 \rightarrow 30^{\circ}C$) to observed any temperature dependencies in the physical processes.

Figure 9.1(a) shows how the *cis* concentration varies as a function of time for varying temperature in the 2%($\frac{w}{w}$) BAAB2 together with 0.5%($\frac{w}{w}$) 15NB3OH in 5CB mixture. The error in the absolute values for *cis* concentration are high in these measurements due to error in cell gap measurements, with each experiment

9. TIME-DEPENDENCE OF PHOTOISOMERISATION

conducted in a different region of the cell to prevent photo-degradation of the sample regions.

It can be seen that the irradiation of the sample with UV at $t=5s$, first dashed line, causes a rapid increase in the *cis* concentration due to the active photoisomerisation of the BAAB2 molecules from the *trans* to the *cis* conformal state. The concentration reaches a maximum point and then remains constant under continuous UV-irradiation. This result indicates that all previous measurements under constant UV irradiation had a stable *cis* population. Upon removal of the UV-irradiation, $t=60s$, the BAAB2 dopant immediately begins to decay back from the *cis* conformer to the *trans* conformer. This decay is a combination of the thermal decay, with the *trans* state being energetically favourable, but also the driven reverse photoisomerisation process from the visible light exciting the *cis* conformers. Now a closer look at each of the processes, photoisomerisation and decay, will be conducted.

Figure 9.1(b) demonstrates how the *cis* concentration increases under UV irradiation. All temperatures demonstrate saturation within a time of 10s. Fitting of a linear relationship to this increase in *cis* concentration (between UV on at $t=5s$ and the first plateau point) the photoisomerisation rate of BAAB2 generated by the UV light source can be measured as a function of temperature. Figure 9.1(c) demonstrates the measured photoisomerisation rate and shows temperature independence, with an average photoisomerisation rate of $(0.12 \pm 0.01)\%s^{-1}$. The temperature independence is expected as the photoisomerisation rate will be dominated by the UV intensity used and the excitation probability of the BAAB2 *trans* molecules.

Once the UV irradiation is switched off at $t=60s$ the *cis* concentration immediately begins to decrease, figure 9.2(a). It can be seen that the *cis* concentration exponentially decays and therefore fitting of an exponential decay equation allows the decay rate to be determined as a function of temperature. Figure 9.2(b) shows that the exponential decay rate increases with increasing temperature from

9.1 Time-dependent optical properties

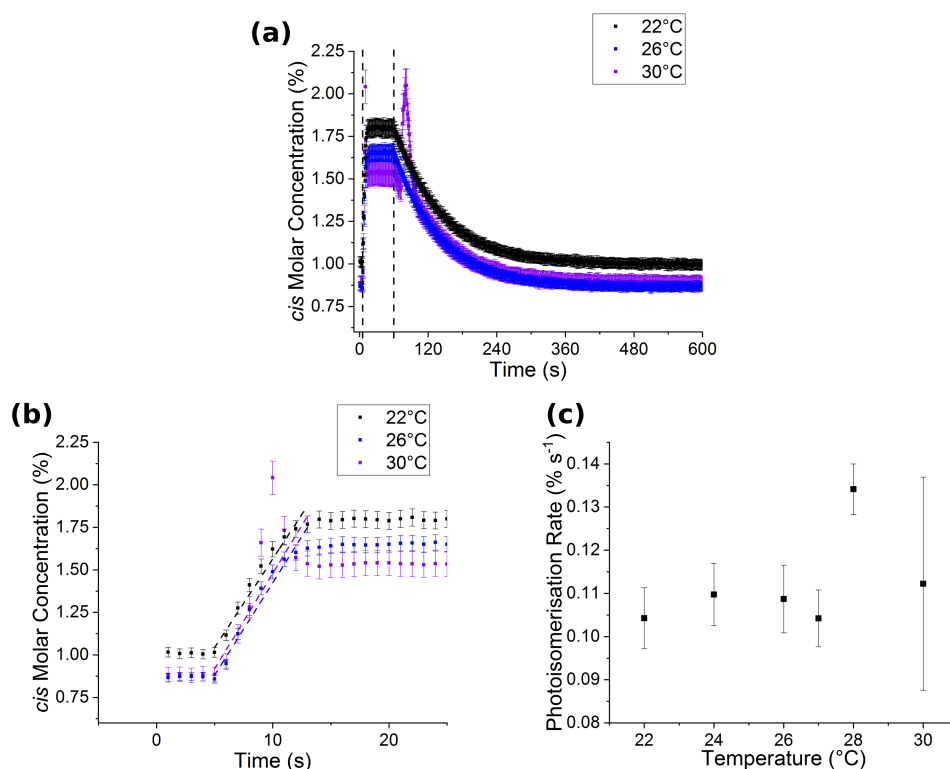


Figure 9.1: (a) *cis* concentration measured with respect to time for 2%($\frac{w}{w}$) BAAB2 together with 15NB3OH in 5CB. The first dashed line at $t=5s$ represents the UV switch on time, whilst the second dashed line at $t=60s$ represents the UV switch off time. (b) A closer look at the active photoisomerisation section with the UV switched on at $t=5s$ and saturation of *cis* molecules achieved within 10s. (c) The photoisomerisation rate as a function of temperature measured via a linear fit of (b).

approximately $0.012 \rightarrow 0.014\%s^{-1}$, an order of magnitude slower than the photoisomerisation rate. The increasing decay rate with increasing temperature is expected due to the transformation from the *cis* to the *trans* being a combination of visible light driven reverse photoisomerisation and thermal decay (with the thermal decay rate increasing with increasing temperature). On average the sample has returned to the original ground state within 6 minutes. It is important to emphasise that this is the decay rate whilst under continuous yellow-filtered

9. TIME-DEPENDENCE OF PHOTOISOMERISATION

visible light illumination which excites the *cis* molecules and drives the reverse photoisomerisation process.

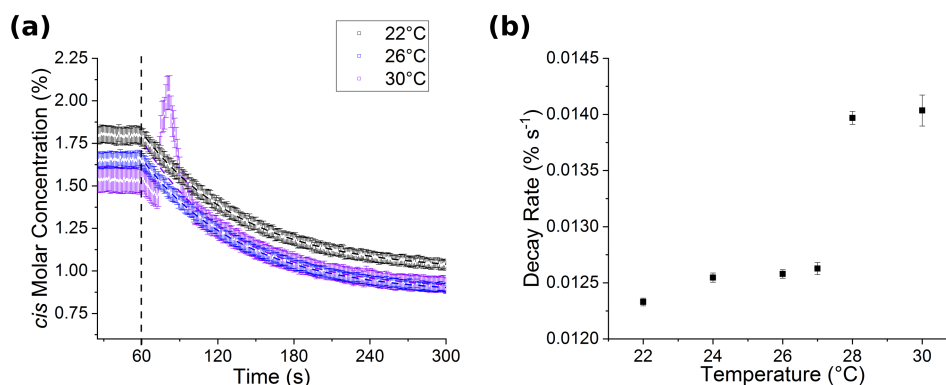


Figure 9.2: (a) The decay of the *cis* molecules after the UV is switched off. (b) The decay rate of the *cis* conformer into the *trans* conformer as a function of temperature measured via an exponential decay fit to (a).

The order parameter was measured via the polarisation angle dependant absorption of the 15NB3OH at 694nm and the variation of order parameter versus time for different temperatures is shown in figure 9.3(a). The experimental data presented demonstrates how the initial order parameter (pre-irradiation) decreases with increasing temperature as expected. The order under continuous irradiation also decreases with increasing temperature, and when above the modified nematic to isotropic transition temperature, measured in chapter 7.3 to be approximately 28°C, the order parameter drops to zero (isotropic). Figure 9.3(b) demonstrates the initial yellow-filtered order parameter and irradiated order parameter measured as a function of temperature in this experiment compared directly with the identical mixtures temperature dependence of order parameter measured in chapter 7.3. Excellent agreement is observed between experimentation. Figure 9.3(c) demonstrates that the order modification generated by the irradiation of the UV light is instantaneous and stabilisation of the order parameter is achieved within 10s, in agreement with the *cis* concentration data (figure

9.1).

Figure 9.3(d) demonstrates how the order parameter recovers when the UV irradiation is switched off. At temperatures where the system remains in the nematic phase under continuous irradiation the order parameter begins to recover instantly as the UV irradiation is removed. However, at temperatures in which the sample undergoes an isothermal phase transition into the isotropic state the recovery of the order parameter is delayed. This is a result of the order modification of the *cis* concentration being much larger than that required to generate an isothermal phase transition and therefore a higher proportion of the *cis* population needs to relax into the *trans* state before the nematic phase is regained and the order can increase.

The time dependence of concentration and order has been established here, however these measurements require constant illumination of the sample with yellow-filtered visible light which has been shown in chapter 7.3 to generate a small amount of photoisomerisation in the samples and will also drive the reverse photoisomerisation process due to the excitation of *cis* conformers with the visible light. To test the impact of the illumination conditions on the samples the capacitance is monitored as a function of time with different illumination conditions triggered at different times.

9.2 Time-dependence of capacitance

In this section the capacitance is monitored as a function of time for 3%($\frac{w}{w}$) BAAB2 together with 0.5%($\frac{w}{w}$) 15NB3OH in 5CB with different illumination conditions to monitor the impact of light on the system. A low voltage of $0.2V_{rms}$ is used in these experiments and therefore the capacitance measured is directly related to the the perpendicular dielectric permittivity.

The capacitance as a function of time is shown in figure 9.4(a). At times less than $t=15s$ there is no light illuminating the system resulting in a constant capacitance. At $t=15s$ the UV irradiation occurs and causes photoisomerisation of the

9. TIME-DEPENDENCE OF PHOTOISOMERISATION

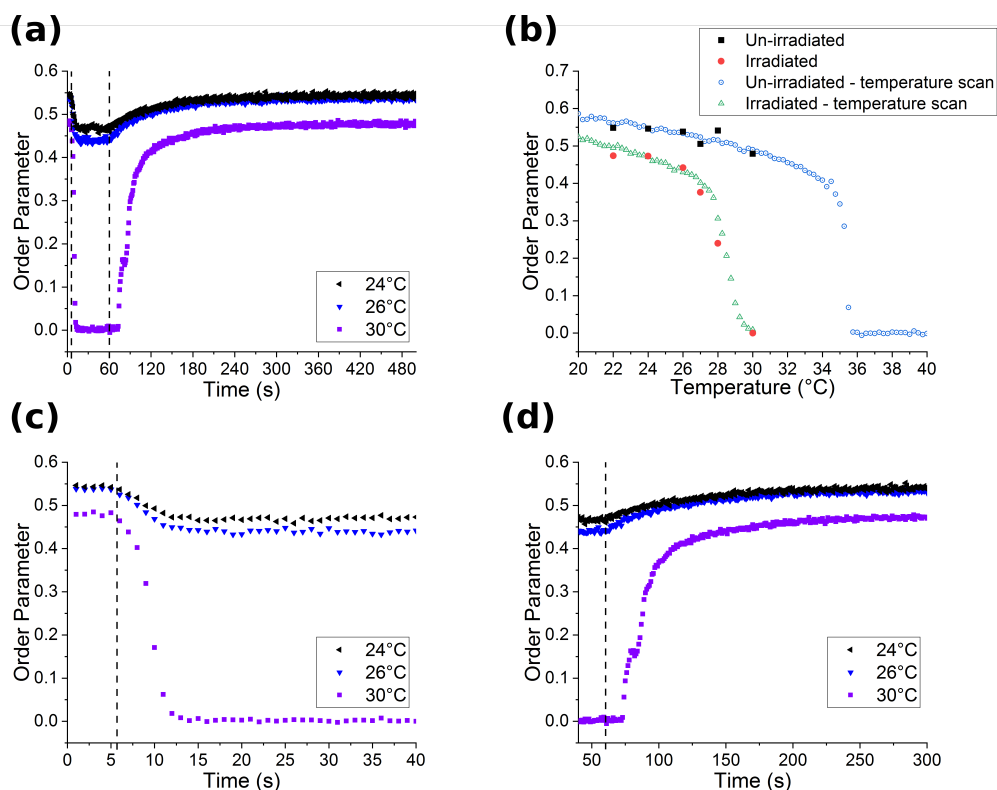


Figure 9.3: (a) The order parameter versus time for 2% ($\frac{w}{w}$) BAAB2 together with 15NB3OH in 5CB. The first dashed line at $t=5$ s represents the UV light being switched on, whilst the dashed line at $t=60$ s represents the UV light being switched off. (b) The maximum and minimum order parameters measured for various temperatures in the time dependent experiment compared with the order parameter versus temperature scan conducted in chapter 7.3. (c) A closer look at the time dependence of the order parameter during the active photoisomerisation process. (d) A closer look at the order parameter recovery during the relaxation of *cis* conformers to the *trans* conformal state.

BAAB2 *trans* conformer into the *cis* conformer before plateauing at a constant capacitance as expected when the *cis* concentration is at its maximum. At time $t=115$ s the yellow-filtered visible light is switched on and results in a decrease in capacitance as the visible light triggers the reverse photoisomerisation process, counter to the UV irradiation. This reaches an equilibrium position where the

9.2 Time-dependence of capacitance

capacitance stabilises. The yellow-filtered visible illumination is removed at time $t=171$ s and the capacitance rapidly returns to its UV saturated value.

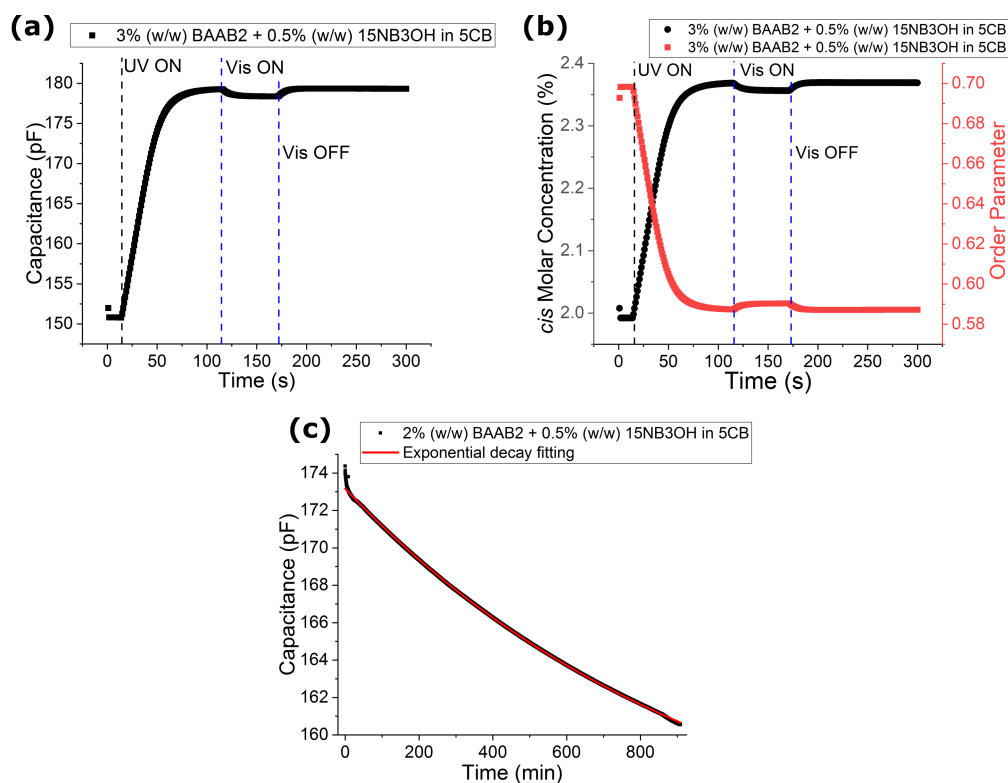


Figure 9.4: Time dependence of (a) Capacitance and (b) *cis* molar concentration for 3% ($\frac{w}{w}$) BAAB2 together with 0.5% ($\frac{w}{w}$), with UV irradiation and yellow-filtered visible irradiation points labelled. (c) The time dependence of capacitance for 2% ($\frac{w}{w}$) BAAB2 together with 0.5% ($\frac{w}{w}$) post UV irradiation with no yellow-filtered visible light illuminating the system.

The molar concentration of *cis* conformers, measured via the optical properties, before UV irradiation and during continuous UV irradiation is found to be 1.9% and 2.5%. Now if it is assumed that the capacitance is directly related to the concentration of *cis* conformers it will enable the impact of the visible light on the *cis* concentration to be estimated. Figure 9.4(b) shows how the approximate *cis* concentration depends on time. The yellow-filtered visible light generates a 0.05%

9. TIME-DEPENDENCE OF PHOTOISOMERISATION

reduction in the *cis* concentration. This a small impact on the *cis* concentration and therefore should not impact previous assumptions. Similar assumptions can be made to attempt to represent the order parameter dependence on time during this experiment. By assuming the order parameter during UV and yellow-filtered light irradiating the system ($S = 0.49$) is directly related to the inverse of capacitance at this point then the data shown for order versus time in figure 9.4(b) can be generated. As expected the order parameter appears to decrease when the UV light is switched on, and then increases again when the yellow-filtered visible light irradiates the system triggering the reverse photoisomerisation process. It is important to note that this result is not a direct measurement, but rather an extrapolation, and therefore is only an aid in attempting to further understand the impact of visible light on the system.

The capacitance was monitored as a function of time for 2%($\frac{w}{w}$) BAAB2 together with 0.5%($\frac{w}{w}$) 15NB3OH in 5CB upon removing the UV irradiation and having no yellow-filtered visible light illumination, figure 9.4(c). Here it is observed that the decay rate is much slower compared to previous results in which the decay was monitored whilst yellow-filtered visible light illuminated the system. The system had not returned to its ground state after 15 hours un-irradiated which demonstrates the impact the visible light has on the relaxation rate of the system.

9.3 Summary

In this chapter the time-dependence of the photoisomerisation process was investigated through a combination of optical and capacitance measurements. The time dependent optical properties determined the photoisomerisation rate was temperature independent with an average photoisomerisation rate of $(0.12 \pm 0.01)\%s^{-1}$. The relaxation rate was found to be temperature dependent, due to the thermal decay of the *cis* to *trans* conformer, varying from $0.012 \rightarrow 0.014\%s^{-1}$ a factor of ten slower than the photoisomerisation rate.

Monitoring of the time-dependence of capacitance revealed the yellow-filtered visible light generates a very small decrease in the *cis* concentration when under continuous UV irradiation (0.05%). The relaxation of the system without the yellow-filtered visible light illuminating the system was shown to be much slower than when illuminated, greater than 15 hours compared to 6 minutes relaxation time when yellow-filter illuminated.

9.4 Summary of photoisomerisation investigation

In the last few chapters the physical impact of azobenzene-based BAAB2 on the nematic LC system was thoroughly investigated. The relative change in intermolecular interaction energy generated from the *cis* molecules in the yellow-filtered state was experimentally measured to be $(-3.5 \pm 0.3) \cdot 10^{-3}$. A 2.5 times larger relative change in intermolecular interaction energy generated from the *cis* molecules was measured in the UV-irradiated state, with a measured value of $(-8.7 \pm 0.2) \cdot 10^{-3}$. This indicated that there is an additional physical mechanism that occurs during UV irradiation that results in an increased order modification. It was hypothesised that a light-induced optical torque is acting on the system out of the plane due to the selective excitation of the BAAB2 molecule from the **unpolarised** UV light. It was suggested that this optical torque could be the cause of the increased order modification under UV irradiation.

Packing of the *cis* molecules in the yellow-filtered state was measured via the polarisation angle dependence of their absorption. The ability for them to pack well with the 5CB host is suggested as the reason for the low levels of order modification in the yellow-filtered state. When in the irradiated state the polarisation angle dependency is lost suggesting the *cis* molecule no longer packs well with the nematic host and is more disordered.

Analysis of the elastic and electrical properties of the system in the yellow-filtered and irradiated state agrees with the hypothesis that an external force is acting out of the plane during the irradiation of the system. Observed changes in physical properties were indicative of an external force acting on the system, rather than actual changes to the physical properties of the system.

The time dependent measurements of the photoisomerisation process demonstrated the importance of the visible light triggering the reverse photoisomerisation process for the rapid relaxation of the system back to the steady state. The photoisomerisation rate caused by the UV light was measured to be $(0.12 \pm$

9.4 Summary of photoisomerisation investigation

0.01) $\%s^{-1}$ and the relaxation rate was found to vary from 0.012 \rightarrow 0.014 $\%s^{-1}$ depending on the device temperature.

These chapters have demonstrated that the light-induced change in physical parameters due to azobenzene-based materials may not simply be a function of *cis* concentration as suggested by LIOM theory. It has been experimentally shown that the light-induced molecular reorientation effect caused by the selective excitation of the BAAB2 molecules generates an optical torque on the strongly anchored system. This optical torque results in a much larger order modification compared to that simply generated by the disruption caused by the *cis* concentration and must therefore be included in considerations surrounding these light-sensitive systems.

9. TIME-DEPENDENCE OF PHOTOISOMERISATION

Chapter 10

All-optical automatic switchable laser protection

Much of the work contained in this chapter was published by Ethan I. L. Jull and Helen F. Gleeson, "All-optical responsive azo-doped liquid crystal laser protection device", *Optics Express*, **26**(26), 2018 [1]. Should any of the work included be specific to an author that is not E. I. L. Jull it will be noted in the text.

10.1 Introduction

Photosensitive LC systems, similar to those discussed in chapter 7 → 9, are incredible materials with a multitude of potential applications. They are typically generated from azobenzene-based materials which exhibit the reversible photoisomerisation process, discussed in chapter 3. There has been considerable research into: the behaviour of chiral nematics doped with azo-based materials [2, 3], azo-based LC materials [4, 5], and also chiral dopant's with an in-built azobenzene group [6–10]. Photosensitive LC systems have been suggested for application in optical data storage devices [8, 11], photo-tuneable diffraction gratings [12, 13], and resonance tuning in plasmonic devices [14, 15].

In this chapter the BAAB2 doped 5CB, discussed in chapter 7, will be presented as a passive switchable laser protection device which automatically switches

10. ALL-OPTICAL AUTOMATIC SWITCHABLE LASER PROTECTION

into a protection/blocking mode under irradiation of the laser wavelength. The use of LCs in laser protection has been previously demonstrated [16, 17], with the electro-optical properties of LCs being an excellent basis for a switchable optical device as shown in chapter 5. However, the need for an external sensor to detect the laser "threat" before switching the LC system into protection mode is somewhat limiting. It seems logical to utilise the light-matter interaction in photosensitive LCs for an all-optical automatically switching protection device.

The reversible *trans-cis* photoisomerisation process will trigger the switch from transmission to blocking in this laser protection device. The photo-induced transformation of the azo-molecule between the *trans* and *cis* conformal states generates an order modification when doped into a LC host (discussed in detail in chapter 3). This order modification will lower the nematic to isotropic phase transition temperature. Therefore, if the device is held in a specified temperature range this photoisomerisation process will induce an isothermal phase transition, the basis for this photo-switchable laser protection device.

10.2 Materials and methods

Mixtures of BAAB2 azo-LC in 5CB were created at varying concentrations from $5 \rightarrow 10\%$ ($\frac{w}{w}$). These mixtures were filled into twisted nematic (TN) planar aligned devices (SE3510 polyimide alignment layer) with approximately $3\mu\text{m}$ cell gaps (fabrication described in chapter 4.5). The absorption spectrum of BAAB2 in acetone measured using an Agilent UV/Vis 6000 spectrometer is shown in figure 10.1. In this application a low-power 405nm laser ($P=0.2\text{-}3.5\text{mW}$, beam diameter= 27mm) will be utilised as the laser "threat" and will trigger the photoisomerisation of the BAAB2 molecules. The overlap of the BAAB2 absorption bands and the 405nm wavelength is shown in figure 10.1 and demonstrates the ability for the laser to trigger the *trans-cis* excitation process.

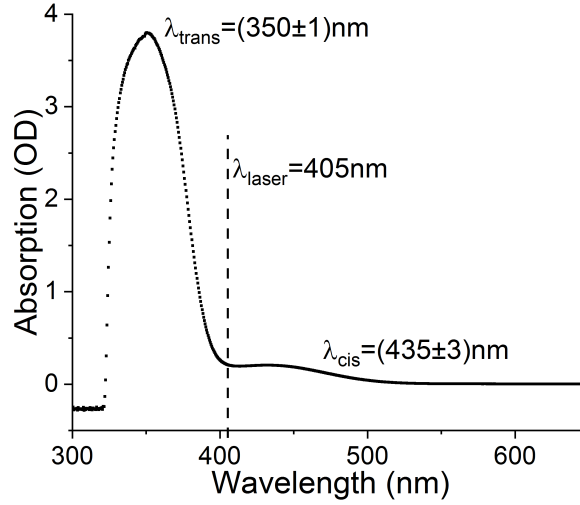


Figure 10.1: The absorption spectrum for BAAB2 dissolved in acetone is shown. The absorption peaks correspond to the *trans* and *cis* conformer excitations. The overlap of the laser wavelength with the *trans* excitation is shown.

10.3 Results and discussion

10.3.1 Phase transition temperature

The fundamental mechanism behind this device is the light-induced isothermal phase transition. Therefore the nematic to isotropic phase transition temperature must be carefully evaluated in the un-irradiated states, under ambient conditions, and under continuous laser irradiation.

DSC (described in chapter 4) and red-filtered POM (to prevent photo-switching from the white light source) was conducted on each of the BAAB2 concentrations in 5CB to evaluate the un-irradiated nematic to isotropic transition temperatures, figure 10.2(a). In the un-irradiated state an increase in the phase transition temperature with increasing BAAB2 concentration is observed. This is a direct result of pure BAAB2 having a higher nematic to isotropic phase transition temperature (83.5°C) compared to pure 5CB (35.8°C). There is a slight discrepancy between the POM and DSC results attributed to the absolute accuracy of each experi-

10. ALL-OPTICAL AUTOMATIC SWITCHABLE LASER PROTECTION

mental method. Subsequent measurements of the nematic to isotropic transition temperature under various irradiation conditions are conducted using POM and therefore will be directly compared to red-filtered POM rather than DSC results.

Illuminating the sample in the POM setup without a red-filter in place will trigger photoisomerisation of the BAAB2 in the sample and this would subsequently reduce the order parameter and therefore the nematic to isotropic phase transition temperature. The broadband light source impact on transition temperature would be less when compared with UV or laser irradiation. It is however an important characteristic to consider if the device is to be implemented in real-world conditions. Therefore, the nematic to isotropic transition temperature was measured whilst under broadband white light in the POM setup for each mixture of BAAB2 in 5CB, figure 10.2(a). An average reduction of approximately 7°C was observed for each concentration, a result of the photoswitching caused by the 50W halogen bulb focussed onto the sample.

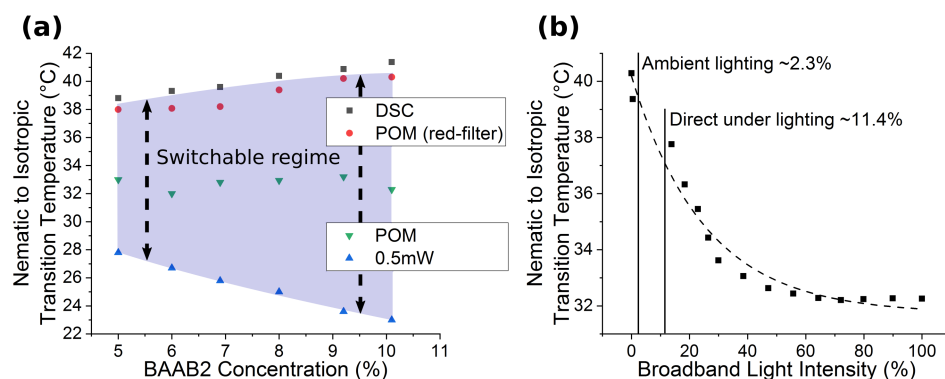


Figure 10.2: (a) The nematic to isotropic transition temperature is evaluated for varying concentration of BAAB2 in 5CB for a variety of irradiation conditions. The blue highlighted zone is the switchable regime in which irradiation with the 405nm laser will result in an isothermal phase transition. (b) The nematic to isotropic transition temperature for 10% $(\frac{w}{w})$ BAAB2 in 5CB as a function of broadband white light intensity is shown. The transition temperature decreases with increasing broadband intensity and an exponential decay is fit to guide the eye.

To further investigate the impact of broadband white light sources the effect of increasing broadband intensity on the nematic to isotropic transition temperature of the 10%($\frac{w}{w}$) BAAB2 in 5CB was evaluated, figure 10.2(b). This demonstrates a reducing transition temperature with increasing broadband intensity. This is expected as the increased intensities will cause an increase in the amount of photoisomerisation that is triggered in the sample. The white light intensity was measured using a photodiode and directly compared to the intensity measured from ambient lighting conditions to give insight into the potential transition temperature modification in standard conditions. The ambient light intensity was found to be approximately 2.3% the maximum microscope intensity which indicates a very small transition temperature modification in implementation of the device in real world conditions.

The impact of continuous wave (CW) laser (0.5mW , 9.0mWcm^{-2}) irradiation on the nematic to isotropic transition temperature of each sample was then investigated. The 405nm laser was coupled into the POM setup via the reflection arm and the transition temperature was measured after 5 minutes of continuous irradiation. The 5 minutes of continuous irradiation was implemented to ensure the sample had fully equilibrated allowing for reproducibility between experimental runs. The results shown in figure 10.2(a) demonstrate the large reduction in transition temperature under CW laser irradiation, approximately 10°C across all concentrations. The overall trend demonstrates a decreasing nematic to isotropic transition temperature with increasing BAAB2 concentration under CW laser irradiation, a direct result of the higher concentration of *cis* conformers.

The temperature range between the un-irradiated transition temperature (POM red-filter) and the CW laser irradiation transition temperature (0.5mW) is denoted the switchable protection regime of the device. If the device is held between these temperatures and exposed to the laser "threat" the system will undergo an isothermal phase transition from nematic to isotropic. In considering our TN device configuration between crossed polarisers this isothermal phase transition will move the device from transmitting between crossed polarisers (nematic) to dark between crossed polarisers (isotropic). The switchable temperature region

10. ALL-OPTICAL AUTOMATIC SWITCHABLE LASER PROTECTION

demonstrated can be readily tuned for any application simply through careful choice of LC host and azo-LC concentration.

10.3.2 Device spectra

Figure 10.3 demonstrates the transmission and blocking spectra of the photo-switchable device. In the transmission, TN, state there is clear transmission observed across the visible spectrum allowing for continual effective observations through the device. There are low levels of absorption noted at lower wavelengths which are a result of the BAAB2. The BAAB2 absorption does not impact implementation of the device as it only slightly impacts the colour of observations made through the device (slightly yellow), as can be seen from the image inserts. Once irradiated with the CW laser the device transitions into the blocking, isotropic, state. The spectrum demonstrates 0% transmission across all wavelengths in the blocking state. It is important to note that the transmission in the blocking state of the device is purely dependent on the polariser extinction ratio of the polarisers utilised. The image inserts in figure 10.3 demonstrates how observations through the device in the transmission and blocking state appear.

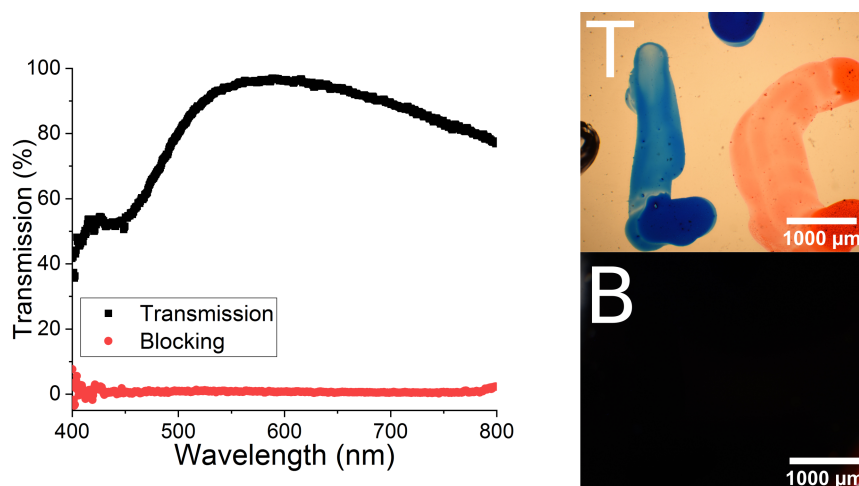


Figure 10.3: The transmission and blocking spectra for the BAAB2 doped 5CB device is demonstrated.

Once the laser irradiation is removed the device will relax back into the TN state as the *trans* conformer is energetically favourable. This will occur typically within an hour, although this is temperature and "light" condition dependent. If the system is exposed to wavelengths of light corresponding to the *cis* excitation the time taken to return back to the nematic state will be greatly reduced, typically within 10 minutes.

10.3.3 Response time

One of the most crucial aspects of switchable laser protection lies in the response time of the device. This was evaluated in these devices by measuring the transmission through the device as a function of time using a photodiode. The response time was measured from the first point of irradiation to 10% transmission, chosen to give a robust comparison between different experimental conditions. The response time of the device was measured as a function of BAAB2 concentration, device temperature, and laser power. Each of these variables will now be evaluated in turn.

The response time was measured as a function of temperature across each BAAB2 in 5CB mixture's switchable protection regime following irradiation with 0.5mW laser power. A comparison of the temperature dependence of response time for 5%($\frac{w}{w}$) and 10%($\frac{w}{w}$) BAAB2 in 5CB is shown in figure 10.4(a). Firstly, the increased operational temperature range of the 10%($\frac{w}{w}$) doped mixture is clear. A decrease in response time with increasing temperature is also observed for both mixtures, ranging from a few hundred milliseconds up to 10s. By plotting these response times as a function of reduced temperature ($\frac{T}{T_{NI}}$) it can be seen that the response time for each mixture simply increases at approximately the same rate as it moves away from the un-irradiated nematic to isotropic transition temperature. This is expected as the further away from the un-irradiated transition temperature the greater the decrease in order required to generate the isothermal phase transition. This therefore requires more BAAB2 to be photoswitched from the *trans* to *cis* state.

10. ALL-OPTICAL AUTOMATIC SWITCHABLE LASER PROTECTION

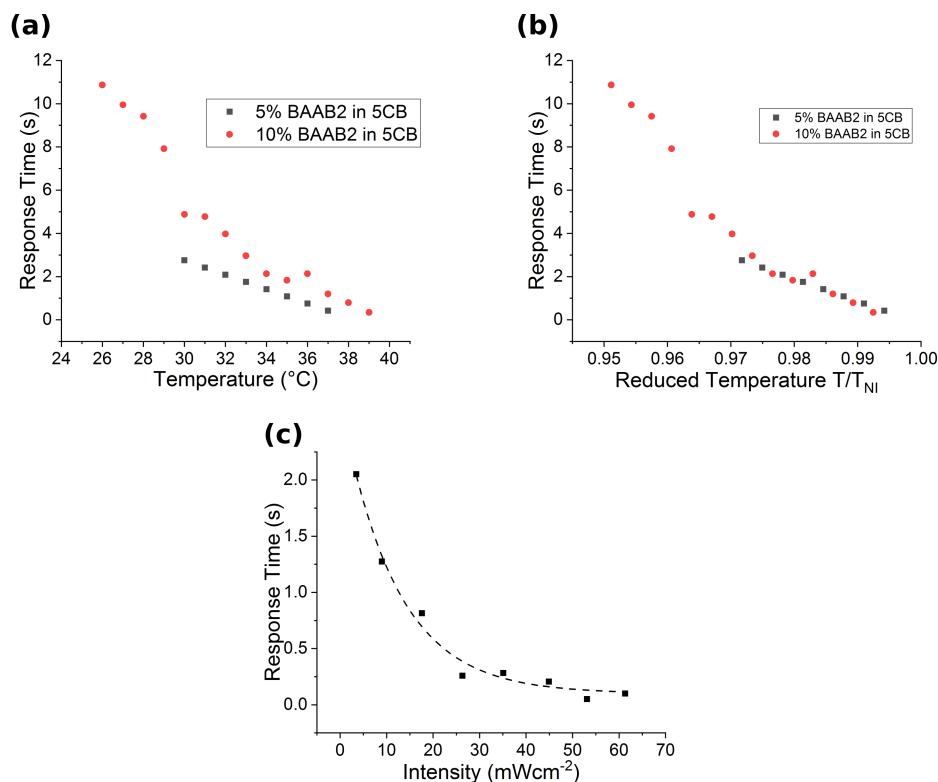


Figure 10.4: (a) The response time for 5% ($\frac{w}{w}$) and 10% ($\frac{w}{w}$) BAAB2 in 5CB as a function of (a) temperature and (b) reduced temperature. (c) The response time dependence of 10% ($\frac{w}{w}$) BAAB2 in 5CB on laser intensity.

The laser intensity irradiating the system will also impact the response time. An increased laser intensity will generate an increased photoisomerisation rate, increasing the order modification rate and therefore the overall system response time. Figure 10.4(c) demonstrates the response time of the 10% ($\frac{w}{w}$) BAAB2 in 5CB mixture, at 2°C below the un-irradiated nematic to isotropic transition temperature. It can be seen that increasing laser intensity generates a much faster response time going from $2 \rightarrow 0.51\text{s}$ over a power range of $0.2 \rightarrow 3.5\text{mW}$ ($3.5 \rightarrow 61.3\text{mWcm}^{-2}$). This means that if the system is under "threat" from a high intensity laser it would result in a reduced exposure time (faster response time) and therefore better protection.

It is noted that the laser wavelength, 405nm, is on the edge of the BAAB2 *trans* excitation waveband and therefore has a relatively low photoisomerisation efficiency. Better matching of the *trans* excitation waveband to the laser wavelength would result in much faster response times.

The response time generated in the photoswitchable device can be compared to literature describing damage to CCD cameras [18]. It was demonstrated by Schwarz that a colour CCD camera experiences damage from $16kWcm^{-2}$ after exposure times of more than 1s. The intensity of the continuous wave laser used in testing this photo-switchable device is much smaller, $61.3mWcm^{-2}$, compared to the threshold damage of a CCD camera demonstrated by Schwarz, $16kWcm^{-2}$.

Response times of less than 1s have been clearly demonstrated, with a much lower laser intensity compared to the threshold damage intensity, in the BAAB2 doped 5CB system investigated in this chapter. This clearly shows how this photo-induced switch will provide protection for colour CCD cameras against large laser intensities, as well as low power intensity dazzling. As demonstrated, the response time decreases rapidly with increasing laser intensity and therefore if a high intensity laser impacted the system it can be expected that the response time would decrease dramatically, providing even greater protection.

10.4 Summary

In this chapter an all-optical passive switchable laser protection device was characterised and tested against a 405nm low powered laser. The optical properties of the device were demonstrated, showing good transmission and blocking states. The response time dependence on BAAB2 concentration, device temperature, and laser intensity were fully explored with a response time of 51ms demonstrated. The ability of the system to provide protection for CCD cameras was evaluated and excellent protection is predicted.

The potential for this device to be applied to real world application is simple and effective. The system can be altered in terms of the azo-dopant and LC

10. ALL-OPTICAL AUTOMATIC SWITCHABLE LASER PROTECTION

host to provide protection in any temperature range from various laser wavelengths. Protection against other laser wavelengths is achieved by shifting the *trans* excitation waveband to the desired region, simply through careful selection of azo-dopant. The passive nature of this device provides a solution which requires no external sensors, and providing good switch speeds into protection mode. Thus, this azo-LC doped device has been demonstrated to be an excellent switchable laser protection device.

References

- [1] E. I. L. Jull and H. F. Gleeson. All-optical responsive azo-doped liquid crystal laser protection filter. *Optics Express*, 26(26):34179–34184, 2018. 159
- [2] H. Lee, K. Doi, H. Harada, O. Tsutsumi, A. Kanazawa, T. Shiono, and T. Ikeda. Photochemical modulation of color and transmittance in chiral nematic liquid crystal containing an azobenzene as a photosensitive chromophore. *Journal of Physical Chemistry B*, 104(30):7023–7028, 2000. 159
- [3] U. A. Hrozhyk, S. V. Serak, N. V. Tabiryanyan, T. J. White, and T. J. Bunning. Optically switchable, rapidly relaxing cholesteric liquid crystal reflectors. *Optics Express*, 18(9):9651–9657, 2010. 159
- [4] U. A. Hrozhyk, S. V. Serak, N. V. Tabiryanyan, and T. J. Bunning. Optical tuning of the reflection of cholesterics doped with azobenzene liquid crystals. *Advanced Functional Materials*, 17(11):1735–1742, 2007. 159
- [5] J. D. Lin, Y. M. Lin, T. S. Mo, and C. R. Lee. Photosensitive and all-optically fast-controllable photonic bandgap device and laser in a dye-doped blue phase with a low-concentration azobenzene liquid crystals. *Optics Express*, 22(8):9171–9181, 2014. 159
- [6] N. Venkataraman, G. Magyar, M. Lightfoot, E. Montbach, A. Khan, T. Schneider, J. W. Doane, L. Green, and Q. Li. Thin flexible photosensitive cholesteric displays. *Journal of the Society for Information Display*, 17(10):869–873, 2009. 159
- [7] T. V. Mykytiuk, I. P. Ilchishin, O. V. Yaroshchuk, R. M. Kravchuk, Y. Li, and Q. Li. Rapid reversible phototuning of laser frequency in dye-doped cholesteric liquid crystal. *Optics Letters*, 39(22):6490–6493, 2014.
- [8] S. Chen, Y. Chen, X. Tong, B. Wu, M. Ma, Y. Shi, and X. Wang. Room temperature optical image storage devices based on novel photo-responsive chiral azobenzene liquid crystal dopants. *Materials Research Express*, 3(11):115701, 2016. 159

REFERENCES

- [9] P. V. Dolganov, S. O. Gordeev, V. K. Dolganov, and A. Yu. Bobrovsky. Photo- and thermo-induced variation of photonic properties of cholesteric liquid crystal containing azobenzene-based chiral dopant. *Molecular Crystals and Liquid Crystals*, 633(1):14–22, 2016.
- [10] Y. C. Hsiao, K. C. Huang, and W. Lee. Photo-switchable chiral liquid crystal with optical tristability enabled by a photoresponsive azo-chiral dopant. *Optics Express*, 25(3):2687–2693, 2017. [159](#)
- [11] T. Ikeda and O. Tsutsumi. Optical switching and image storage by means of azobenzene liquid-crystal films. *Science*, 268(5219):1873–1875, 1995. [159](#)
- [12] L. de Sio, A. Serak, N. Tabiryan, and C. Umeton. Mesogenic versus non-mesogenic azo dye confined in a soft-matter template for realization of optically switchable diffraction gratings. *Journal of Materials Chemistry*, 21(19):6811–6814, 2011. [159](#)
- [13] L. de Sio, L. Ricciardi, S. Serak, M. La Deda, N. Tabiryan, and C. Umeton. Photo-sensitive liquid crystals for optically controlled diffraction gratings. *Journal of Materials Chemistry*, 22(14):6669–6673, 2012. [159](#)
- [14] Z. Chen, K. S. Hsiao, X. Li, Z. Li, J. Yu, and J. Zhang. Optically tunable microfiber-knot resonator. *Optics Express*, 19(15):14217–14222, 2011. [159](#)
- [15] G. Gilardi, S. Xiao, N. Asger, Mortensen, A. d’Alessandro, and R. Beccherelli. Plasmon resonance optical tuning based on photosensitive composite structures. *Journal of the Optical Society of America B*, 31(2):360–365, 2014. [159](#)
- [16] E. I. L. Jull and H. F. Gleeson. Tuneable and switchable liquid crystal laser protection system. *Applied Optics*, 56(29):8061–8066, 2017. [160](#)
- [17] A. Rees and J. Staromlynska. Automatic laser light detection and filtering using a liquid crystal Lyot filter. *Journal of Nonlinear Optical Physics and Materials*, 2(4):661–676, 1993. [160](#)

REFERENCES

- [18] B. Schwarz, G. Ritt, M. Koerber, and B. Eberle. Laser-induced damage threshold of camera sensors and micro-optoelectromechanical systems. *Optical Engineering*, 56(3):034108, 2017. [167](#)

REFERENCES

Chapter 11

Conclusion

At the beginning of this thesis the fundamentals of liquid crystal physics were introduced to give an excellent foundation for the discussions involved in this research. This was followed by a more detailed look at dichroic dyes, the guest-host effect, and the photoisomerisation of azobenzene materials and their effect on liquid crystals.

A rapid, compact, switchable, and tuneable liquid crystal Lyot filter was investigated for its ability to provide optical protection for cameras and eyesight against damaging continuous lasers. Specific wavelength rejection was achieved by utilising the wavelength dependent transmission between aligned polarisers, with a tuneable rejection wavelength across the visible spectrum ($475 - 650nm$) achieved by application of low voltages to the liquid crystal layer ($0.5 - 1.05V_{rms}$). A wavelength independent transmission mode was achieved via high-voltage application ($30V_{rms}$), which reduces the liquid crystal birefringence to approximately 0 resulting in transmission between aligned polarisers. The response time was investigated in switching between the OFF and ON states for protection against three common laser wavelengths (as well as between these different ON states). This demonstrated response times varying between 40 and 110ms, fast enough to provide protection for CCD cameras against up to 18W laser power sources.

The implementation of this liquid crystal Lyot filter as a switchable laser protection device would be simple, with calibration testing required to allow for any

11. CONCLUSION

temperature dependence in the device. Future work on this liquid crystal Lyot filter for laser protection device should involve the investigation into the use of a negative dielectric liquid crystal constrained in a homeotropic orientation device. This would result in an improved ON response time of the device as the switch would be driven by the application of a voltage (from low to high voltage), rather than a relaxation from a high-voltage state as is the case here. The use of a negative dielectric liquid crystal would also result in the OFF state being the $0V_{rms}$ state, reducing the overall power consumption of this device.

The effect of doping a high-solubility anthraquinone-based dichroic dye into the nematic liquid crystal host 5CB was investigated. The maximum solubility limit of this new high-solubility dye was indirectly extrapolated to be approximately $7\%(\frac{w}{w})$ in 5CB, higher than previous reports of anthraquinone solubility in nematic liquid crystals, although a direct measurement is required to confirm this. The impact of these high concentrations of dichroic dye on the host 5CB's phase, optical, elastic, and dielectric properties were then investigated. The nematic temperature range was found to increase with increasing dye concentration, from an $11^\circ C$ range for pure 5CB to a $19.3^\circ C$ for $5.0\%(\frac{w}{w})$ high-solubility dye in 5CB. The absorption peak for the high-solubility dye was found to be $(403.1 \pm 0.4)nm$, with parallel and perpendicular absorption coefficients when in the nematic host 5CB found to be $\alpha_{\parallel} = (0.012 \pm 0.001)OD\mu m^{-1}\%(\frac{w}{w})^{-1}$ and $\alpha_{\perp} = (0.0027 \pm 0.0001)OD\mu m^{-1}\%(\frac{w}{w})^{-1}$. Finally, the elastic splay and bend constants were found to decrease with increasing dye concentration in 5CB. The perpendicular dielectric permittivity remained largely unchanged with increasing concentration, whilst the parallel dielectric permittivity showed a large systematic reduction with increasing dye concentration.

The impact of the high-solubility dye on the nematic host physical parameters are incredibly important in establishing dichroic dye guest-host device capabilities. The impact on the elastic and dielectric properties will alter the systems response to external fields and drastically change device performance. Further investigations are required on this high-solubility anthraquinone dichroic dye to allow for more confidence in the conclusions presented in this thesis. Restrictions

in material availability meant that the solubility limit could not be established through the standard method of over-saturated absorption spectroscopy measurements, required to confirm the solubility limit of $7\%(\frac{w}{w})$ measured here.

An anthraquinone dye doped liquid crystal elastomer was developed and the strain dependence of order parameter was investigated via the polarisation angle dependence of the dichroic dyes absorption. It was demonstrated that the material order parameter had a linear dependence on the strain, showing excellent agreement with separate Raman spectroscopy data. The order parameter dependence on strain was found to be largely temperature independent, with a maximum order parameter measured to be $S = (0.28 \pm 0.01)$ before material breakage. It was suggested that the material could be used as a simple optical strain sensor, with a transmission contrast of 15% measured at a strain of 0.276 .

This dye doped liquid crystal elastomer demonstrated clearly how the absorption properties of a dichroic dye can be utilised as a probe in investigating a systems order parameter. Further work is required on this material to fully investigate the temperature dependence of this material's strain induced order to fully evaluate whether it is truly temperature independent as the result here suggest. Further characterisation of the strain induced change in optical properties should also be conducted, with various dichroic dyes to establish the best possible change in optical properties under strain for simple optical strain sensor application.

The requirement of an external sensor on the switchable liquid crystal Lyot filter device to switch the device into protection mode was deemed restrictive in the device capabilities and therefore light-sensitive liquid crystal systems were investigated to remove this need. Azobenzene BAAB2 was first characterised in terms of its phase and optical characteristics. A nematic phase was demonstrated between $48 \rightarrow 83^{\circ}C$ for the un-irradiated sample and the absorption peaks for the *trans* and *cis* excitations were found to be $\lambda_{trans} = 350nm$ and $\lambda_{cis} = 435nm$.

11. CONCLUSION

Doping of the nematic liquid crystal 5CB with this azobenzene material was then undertaken at varying concentrations up to $10\%(\frac{w}{w})$. In the un-irradiated state the nematic to isotropic phase transition temperature was found to increase approximately linearly from $38.0 \rightarrow 40.3^\circ C$ between 5 and $10\%(\frac{w}{w})$ BAAB2 in 5CB, a direct result of the higher nematic temperature range of BAAB2 compared to 5CB. Under continuous irradiation from a low powered 405nm continuous laser the photoisomerisation of the BAAB2 molecules resulted in a reduction in the nematic to isotropic phase transition temperature (a light-induced order modification). However, fitting of the light-induced order modification model demonstrated that the assumption that full photoisomerisation of the BAAB2 population had occurred via this low powered laser irradiation was wrong.

Therefore, to fully investigate this material an additional anthraquinone dichroic dye dopant 15NB3OH was introduced as a method to directly monitor the order modification generated by the photoisomerisation process. The average absorption coefficient for the BAAB2 *cis* conformer was measured to be $\alpha(450nm) = (0.0109 \pm 0.0003)OD\mu m^{-1}\%^{-1}$ allowing a direct measurement of the *cis* population in any system state. It was found that in the yellow-filtered state a small amount of light leakage generated an increase in the *cis* population and subsequently generated an order modification. The relative change in intermolecular interaction energy generated by the low-intensity yellow-filtered photoisomerisation was found to be $(-3.5 \pm 0.3) \cdot 10^{-3}$. Irradiation of the samples using an **unpolarised** UV light source was then conducted to induce full photoisomerisation of the samples. The relative change in intermolecular interaction energy was found to be 2.5 times larger than the yellow-filtered results, at $(-8.7 \pm 0.2) \cdot 10^{-3}$ indicating that a secondary mechanism was generating a larger order modification in the system.

It was hypothesised that the secondary physical process responsible for the increased order modification was a light-induced torque generated by the selective excitation of the BAAB2 azobenzene material. The irradiation with **unpolarised** UV light from above generates an affinity for the BAAB2 to orient out of the plane, generating an optical torque on the system. This was investigated by

utilising dielectrics as a probe into the material. Under continuous UV irradiation, compared to similar *cis* concentrations under the two irradiation conditions (UV and yellow-filtered), a reduction in the elastic constants, an increase in perpendicular permittivity, and an increase in pre-tilt angle were observed. All of these observations are indicative of an external force acting out of the plane of the system (unaccounted for in fitting resulting in the observed "changes" to physical parameters).

These results demonstrated how the light-induced order modification model assumption that the order reduction is simply a function of *cis* concentration is incorrect. As shown here the irradiation conditions are incredibly important and the possibility of additional order modification being generated by light-induced molecular reorientation (optical torque) in azobenzene based materials must also be considered.

The time dependence of the photoisomerisation process of the BAAB2 doped 5CB system was then investigated, demonstrating a temperature independent photoisomerisation rate of average $(0.12 \pm 0.01)\%s^{-1}$. The decay rate was found to vary with temperature, as expected due to the thermal decay process involved in the *cis* to *trans* relaxation, from $0.012 \rightarrow 0.014\%s^{-1}$. The decay rate was also found to be highly dependent on the illumination conditions due to the reverse photoisomerisation process being triggered by visible wavelengths of light. Illumination with yellow-filtered light resulted in the systems typically relaxing within 6 minutes, whilst no illumination meant that full relaxation took more than 15 hours.

Future work on this incredible light-sensitive material should further investigate the optical properties of the BAAB2 doped 5CB system. The light-induced order modification model also assumes that the change in the materials polarisability during photoisomerisation is negligible when compared with the impact of the order modification. However this may not be a correct assumption for this material and further characterisation of the photoisomerisation process is required should this system be utilised in further applications. Modelling of the

11. CONCLUSION

system for comparison with experimental data would also aid in increasing confidence in the conclusions drawn in this thesis, especially surrounding the packing of the *cis* conformer in the low-intensity states.

The ability for the BAAB2 doped 5CB system to act as an all-optical automatic photo-switchable laser protection device was then demonstrated. The ability for the twisted nematic BAAB2 doped 5CB device to switch between a transmission and blocking mode via irradiation with a low-powered continuous laser of 405nm was demonstrated. The response time dependence on temperature and laser power was carefully characterised and the ability for the device to provide protection for CCD cameras was evaluated with excellent protection predicted.

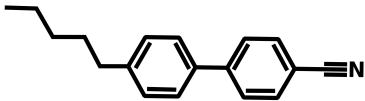
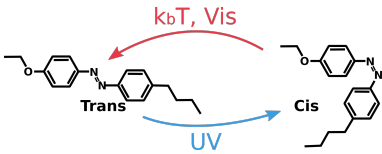
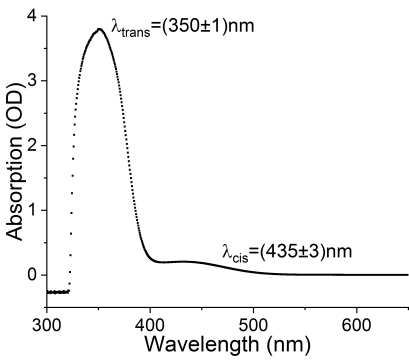
The investigation into light-sensitive liquid crystal materials has developed some interesting systems with some intriguing applications. The ability for devices to switch in response to light means that they have the capability to provide excellent protection against damaging wavelengths. Full investigation into the light-induced order modification generated by azobenzene based materials in nematic liquid crystal unveiled some intriguing physics and demonstrated how predictions of these materials requires careful consideration not only of conformer concentrations, but also the irradiation conditions. The ability to accurately predict how these materials act is crucial not only in application development, but also in photo-alignment investigations in which the photoisomerisation process is utilised heavily.

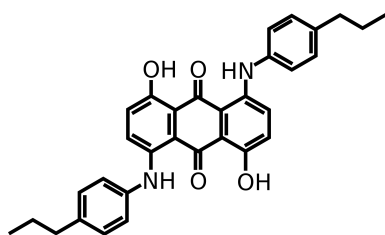
Appendix A

Materials Glossary

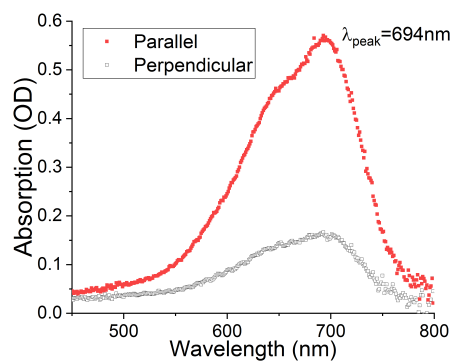
Here a glossary of the most common materials are included for ease of reference.

A. MATERIALS GLOSSARY

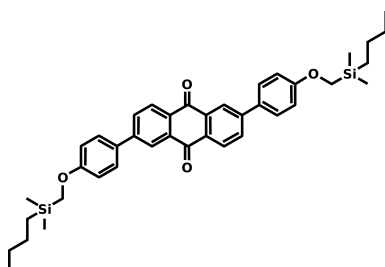
Material	Phase sequence and Absorption spectrum
 <p data-bbox="277 898 643 976"><i>4-Cyano-4'-pentylbiphenyl</i> 5CB</p>	<p data-bbox="884 853 1062 887">K-N=25.0°C</p> <p data-bbox="884 898 1062 931">N-I=36.3°C</p>
 <p data-bbox="240 1417 679 1496"><i>4-2-nutyl-4'-2-alkoxyazobenzene</i> BAAB2</p>	 <p data-bbox="884 1417 1062 1451">K-N=48.5°C</p> <p data-bbox="884 1462 1062 1496">N-I=83.5°C</p>



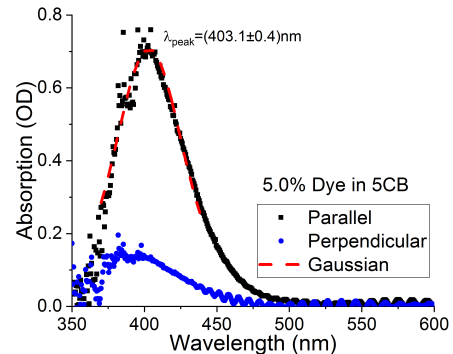
1,5-Dihydroxy-4,8-bis-(4-propylphenylamino) anthraquinone
15NB3OH



N/A



2,6-bis(4-(butyldimethylsilyl)oxy)phenyl) anthracene-9,10-dione
High-solubility Dye



K-I=48.5°C